Title
Photochemical Manipulation of Nanoscale Semiconductor Materials

Author
Jung, Hankyeol

Publication Date
2021

UNIVERSITY OF CALIFORNIA SAN DIEGO

Photochemical Manipulation of Nanoscale Semiconductor Materials

A dissertation submission in partial satisfaction of the requirements for the degree

Doctor of Philosophy

in

Materials Science and Engineering

by

Hankyeol Jung

Committee in charge:

Professor Alina M. Schimpf, Chair
Professor Prabhakar R. Bandaru
Professor Andrew C. Kummel
Professor Ping Liu
Professor Jefferey D. Rinehart

2021

The Dissertation of Hankyeol Jung is approved, and it is acceptable in quality and form for publication on microfilm and electronically.

University of California San Diego

2021

DEDICATION

To my family.

TABLE OF CONTENTS

Chapter 1: Introduction

Chapter 2: Photochemical Reduction of Nanocrystalline Maghemite to Magnetite

Chapter 3: UV irradiation of Colloidal WSe_2 Nanocrystals with Lithium Triethylborohydride

Chapter 4: Air-Stable Reduction of Zn-Bridged Preyssler-Type Polyoxometalate Frameworks

LIST OF FIGURES

LIST OF TABLES

LIST OF ABBREVIATIONS

CAN	Ceric ammonium nitrate
CB	Conduction band
$Cu[OTf]_2$	Coppertriflate
e^-_{CB}	Conduction-band electron
EtOH	Ethanol
FWHM	Full width at half maximum
HOMO	Highest occupied molecular orbital
h^+_{VB}	Valence-band hole
HWHM	Half width at half maximum
ICP-MS	Inductively coupled plasma detected by mass spectroscopy
IR	Infrared
LED	Light emitting diode
$Li[Et_3BH]$	Lithium triethylborohydride
LUMO	Lowest unoccupied molecular orbital
MeOH	Methanol
NIR	Near infrared
OA	Oleic acid
OAm	Oleylamine
PL	Photoluminescence
POM	Polyoxometalate
pXRD	Powder X-ray diffraction
SQUID	Superconducting quantum interference device

TEM	Transition electron microscopy
TGA	Thermogravimetric analysis
THF	Tetrahydrofuran
TM	Transition metal
Tol	Toluene
TOPO	Trioctylphosphine oxide
UV	Ultraviolet
VB	Valence band
vdW	van der Waals
Vis	Visible light
XPS	X-ray photoelectron spectroscopy

ACKNOWLEDGEMENTS

I would like to give special thanks to:

Prof. Alina M. Schimpf for supporting me to grow as an independent scientist and engineer, as well as guiding me to the world of photodoping and materials chemistry. I am grateful for Alina’s enthusiasm and in-depth insight in chemistry, which I admire and want to emulate. I will miss our post-group-meeting Rock Bottom outings and occasional lab parties. Prof. Andrew Kummel, Prof. Prabhakar Bandaru, Prof. Jeffery Rinehart, and Prof. Ping Liu for being my committee members and providing valuable discussions and insightful comments on my research.

The Schimpf lab members, especially Khin San, Jessica Geisenhoff, Linfeng Chen, Alec Rachkov, Carl Lemmon, Liana Alves, Ashley Tamura, Haley Palm, and Haeun Chang for fun conversations about research, as well as non-research topics, and for spending/surviving graduate school period together with me. Former lab members, especially Mike Turo, Billy Pistel, Asel Karunaratne, Richard Tran, Steffen Mevik, Ruth Reinicke, and Bruce Tompson for keeping me a pleasant company. I am grateful that I could have ever had a chance to work with my labmates, who made my lablife more enjoyable than ever.

Friends, particularly BJ and Joanna, who have been my best friends since I came to San Diego, for always supporting me and bringing me to the Convoy. Miran, Hee-dae, and Junghye for presenting me with unforgettable memories during my graduate school period. Yeara, Seungyoon, and Hyeseon for in-depth conversation about Korean TV shows and numerous foodie trips around San Diego. Hyeseung, Dong-yeon, Gina, Jinyoung, Hyewon, and Woojoo, Ling for being my best consultants and supporters. KAIST people and ‘San Diego seven girls’ for having been my local besties for the last two years.

Finally, my family who have supported and believed me to grow up to be who I am today. Especially my mother and father for their dedication and sacrifice for our family, for making me relaxed through what is supposed to be a highly stressful time, and for being my primary mentors and role models in life. My brother for always cheering me and making me laugh. My aunt and uncle, who are my second parents, for having given me affectionate care and support.

Chapter 2, in full, is a reprint of the material as it appears in **Jung, H.**, Schimpf, A. M. Photochemical reduction of nanocrystalline maghemite to magnetite. Submitted and under review. The author of this dissertation was the primary author of the material. I would like to thank Ben and Jeremy for assistance with magnetic measurements and analysis.

Chapter 4, in part, is currently being prepared for submission for publication in Chen, L., **Jung, H.**, Schimpf, A. M.* Air-Stable Reduction of Zn-Bridged Preyssler-Type Polyoxometalate Frameworks. Manuscript in Preparation. The author of this dissertation was the second author of the material. I would like to thank Linfeng for valuable discussions we had.

VITA

2013	Bachelor of Science in Materials Science and Engineering
	Korea Advanced Institute of Science and Technology, South Korea
2015	Master of Science in Materials Science and Engineering
	Korea Advanced Institute of Science and Technology, South Korea
2021	Doctor of Philosophy in Materials Science and Engineering
	University of California San Diego

PUBLICATIONS

1. Mnoyan, A., Lee, Y., **Jung, H.**, Kim, S., and Jeon, D. Y.* Cadmium Free Quantum Dots. Invited for: Phosphors, Up conversion Nano Particles, Quantum Dots and Their Applications. Ru-Shi Liu, *Springer*, (2016)

2. **Jung, H.**, Schimpf, A. M.* Photochemical Reduction of Nanocrystalline Maghemite to Magnetite. Under Review.

3. Chen, L., **Jung, H.**, Schimpf, A. M.* Air-Stable Reduction of Zn-Bridged Preyssler-Type Polyoxometalate Frameworks. Manuscript in Preparation.

ABSTRACT OF THE DISSERTATION

Photochemical Manipulation of Nanoscale Semiconductor Materials

by

Hankyeol Jung

Doctor of Philosophy in Materials Science and Engineering

University of California San Diego, 2021

Professor Alina M. Schimpf, Chair

Modulation of chemical, photophysical, and electronic properties by controlling the type and concentration of carriers is an essential ability that enables semiconductor applications in a wide range of technologies. Colloidal semiconductor nanocrystals are an attractive class of solution processable and tunable semiconductor materials. Several doping strategies have been successfully applied to semiconductor nanocrystals, making them promising components of emerging technologies. Photochemical doping has emerged as a particularly attractive strategy for post-synthetic electronic doping of colloidal semiconductor nanocrystals because it is reversible, nondestructive and solution-stable. This dissertation focuses on the photochemical manipulation of nanoscale materials, including colloidal nanocrystals and cluster-based frameworks.

Chapter 1 provides an introductory overview of electronic doping strategies. Furthermore, background on the classes of materials studied within, colloidal nanocrystals and cluster-based frameworks, is provided. Chapter 2 presents the photochemical reduction of colloidal maghemite nanocrystals as a means to access high-quality magnetite nanocrystals. The phase-transformation of iron oxide nanocrystal *via* introduction of excess carriers is analyzed by X-ray, optical, and magnetic characterization methods. Furthermore, the factors limiting photochemical reduction are discussed. Chapter 3 details the UV irradiation of colloidal 2H tungsten diselenide nanocrystals using lithium triethylborohydride. This phototreatment leads to a bleach of the band-edge absorption and an enhancement and blue-shift of the C-exciton absorption. Powder X-ray diffraction suggests that these changes are primarily due to lithium-ion intercalation into these two-dimensional materials. Chapter 4 extends the methods for electron-quantification in photochemically doped semiconductor nanocrystals do photochemically reduced cluster-based frameworks. The synthesis of cluster-based frameworks allows for *in situ* photodoping to access highly crystalline, reduced cluster-based frameworks. The results are used to demonstrates the unique stability of reduced Zn-bridged frameworks based on Mo-doped Preyssler clusters.

Chapter 1: Introduction

1.1 Introduction to electronic doping of semiconductor materials

The electrical properties of semiconductors can be modulated by electronic doping,[1] which refers to a process of controlling the carrier density without significantly changing the crystal structure. The introduction of delocalized electrons or holes renders the semiconductor *n*-type or *p*-type, respectively. The introduction of delocalized carriers leads to new intraband absorption and to a bleach of the band-edge absorption, indicative of band-filling. By altering the degree of doping, electron density and conductivity of the semiconductor materials can be controlled, which is a critical feature of many semiconductor-based technologies. This thesis will focus largely on photochemically induced electronic doping of colloidal semiconductor nanocrystals, with extension to bulk materials in the final chapter.

Electronic doping of nanocrystals can be challenging due to the high surface-area, which can host defects and trap states that act as a source for undesired of charge-compensation.[2-7] Although "deactivation" of charge-carriers due to these surface sites remains a challenge, several methods of electronic doping have been successfully applied to colloidal semiconductor nanocrystals. These include aliovalent impurity doping, defect-induced doping, remote chemical doping, and photochemical doping, which will be the focus of this thesis.

Aliovalent doping. Aliovalent or heterovalent doping (**Figure 1.1**) is a conventional doping method for bulk semiconductors. For example, substituting a silicon with a group-V dopant (e.g. P, As, Sb) generates an excess positive charge, which can be compensated by a free electron that tunes the neutral silicon into an *n*-type semiconductor. If a group-III dopant (e.g. B, Al, Ga, In) is doped into silicon, a hole is generated to compensate the excess negative charge, and the silicon becomes *p*-type. Although aliovalent doping of colloidal semiconductor nanocrystals is challenging due to uncontrolled surface impurities or trap sites, which can serve as another sources of charge compensation, there have been some noticeable achievements. For example, in Sn^{4+}-doped In_2O_3 (ITO), In^{3+} in nanocrystals replaced by Sn^{4+}, yielding excess positive charge on the cation site that is compensated by delocalized electrons.[8-9] Aliovalent doping results in air-stable *n*- or *p*-type doping but controlling the homogeneity of the dopants throughout the lattice remains challenging.

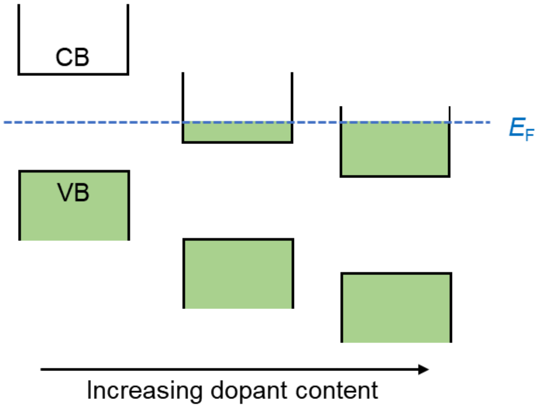

Figure 1.1. Aliovalent *n*-type doping is achieved through substitutional incorporation of excess positive charges, which stabilize the conduction and valence bands (CB and VB, respectively) relative to the Fermi level (E_F) and allow for air-stable electron-accumulation.

Defect-induced doping. Similar to aliovalent impurity doping, defects in the crystal lattice such as vacancies or interstitial ions can serve as electron donors or acceptors to yield r *n*-type or *p*-type doping. For example, copper vacancies are prevalent defects in $Cu_{2-x}E$ (E = S, Se, Te) nanocrystals.[10-12] The missing cations can be compensated by delocalized holes, inducing *p*-type degenerate electronic doping and plasmonic features.[13-16] Similarly, a change in stoichiometry can induce electronic doping. For example, infusing excess Pb or Se into PbSe nanocrystals leads to *p*- or *n*-type doping, respectively, exhibiting semi-metallic properties.[17]

Remote chemical doping. In remote chemical doping, free carriers are injected into the nanocrystals by charge-transfer from a molecular donor (**Figure 1.2**). For example, biphenyl radicals have been used to reduce colloidal ZnO, CdS, and CdSe nanocrystals with band-like electrons.[18] In another example, cobaltocene was used as an electron donor for PbS and PbSe colloidal nanocrystals, leading to the bleach of $1S_h$–$1S_e$ absorption peaks and heavy charging that increased the conductivity of nanocrystal-derived films.[19]

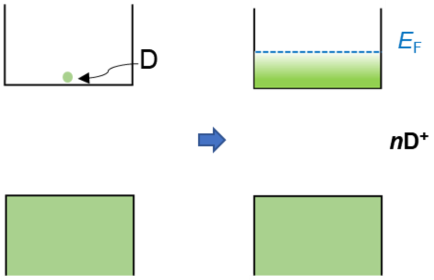

Figure 1.2. Scheme of remote chemical doping. D = electron donor, D$^+$ = oxidized electron donor.

Photochemical doping (Photodoping). Comparable to remote chemical doping, photochemical doping also introduces excess carriers into colloidal semiconductor nanocrystals. As opposed to chemical doping, which employs a direct charge-transfer from a reductant to the nanocrystal, photochemical doping (**Figure 1.3**) employs light and hole-quenchers (sacrificial reductants), such as alcohols or borohydrides.[20-23] In this case the semiconductor is irradiated with UV light, generating a CB-electron and VB-hole. In the presence of an appropriate sacrificial reductant, the photogenerated hole is quenched, leaving an electron in the CB. As long as the oxidation of the hole-quencher remains irreversible,[20] this process can be used to accumulate multiple electrons in the CB. Photochemical doping thus allows post-synthetic and reversible in situ manipulation of carrier concentration. For example, ZnO and TiO_2 nanocrystals have been photochemically reduced under UV irradiation using alcohols as hole-quenchers.[20-22, 24-26] The shallower VB of CdSe requires more reducing sacrificial reductants, such as $Li[Et_3BH]$ to be photochemically reduced.[23] This dissertation focuses on the application of photochemical doping toward various semiconductor systems, including colloidal nanocrystals and cluster-based frameworks, which are briefly introduced below.

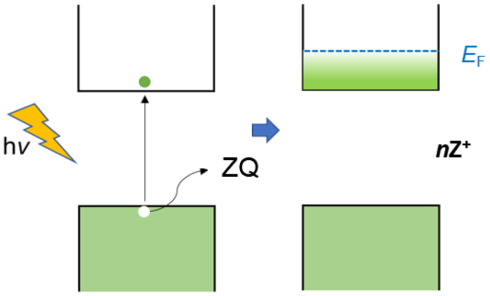

Figure 1.3. Scheme of photochemical doping. E_F = Fermi level, ZQ = hole-quencher and Z^+ = charge-compensating cations from the oxidized hole-quencher.

1.2 Introduction to colloidal semiconductor nanocrystals

Colloidal semiconductor nanocrystals and quantum dots are among the most essential materials for next-generation technologies, including light emitting diodes,[27-29] photodetector,[30-33] and solar cells[32, 34-36], due to their high absorption coefficients, high PLQY, size-dependent bandgap, and solution-processability. Significant progress has been made over decades from fundamental concepts to fabrication and manipulation of nanoscale crystallites.[37-42] In colloidal syntheses, the composition, size, size-distribution, and shape of products can be easily controlled by tuning experimental parameters, such as identity/ratio of precursors and surface ligands, time, and temperature of the colloidal synthesis. (**Figure 1.4**) The resulting products are in the form of inorganic cores colloidally stabilized by organic ligand-shells in solution, which make them primed for fundamental, solution-phase studies and processing.

To fully exploit the advantages of semiconductor nanocrystals for future technologies, understanding on the modulation of optical, electrical, and magnetic properties is essential. In this thesis, we use photochemistry to induce and study changes in the properties of colloidal semiconductor nanocrystals. Chapters 2 and 3 focus on UV irradiation of colloidal iron oxide and tungsten diselenide nanocrystals, respectively. Chapter 4 extends the photochemical methods to solid-state materials derived from cluster coordination assembly.

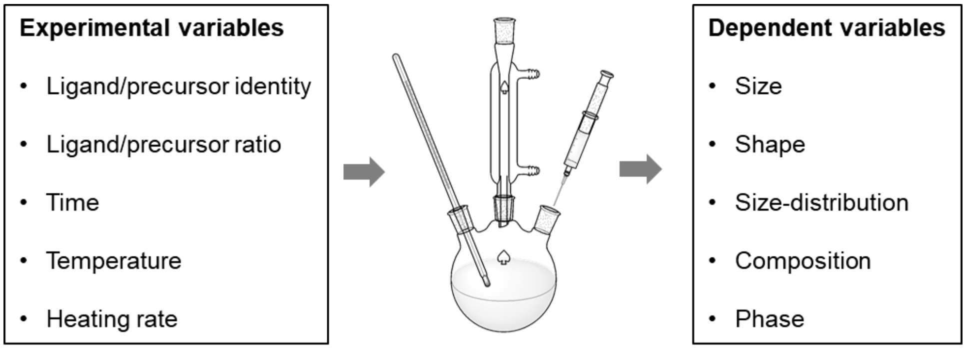

Figure 1.4. In colloidal synthesis of semiconductor nanocrystals, experimental variables give facile handle for controlling the physical and chemical properties of the resulting nanocrystal products.

1.3 Introduction to polyoxometalate-based frameworks

Polyoxometalates (POMs) are molecular analogs of metal oxide quantum dots that can be assembled into nano-, micro- or even millimeter sized metal oxide materials.[43-44] The structural diversity and reversible redox activity of POMs make them attractive building-blocks for coordination with organic or inorganic linkers to build frameworks.[45-46] POM-based frameworks are expected to have high electron capacity and exceptional structural stability, but their photophysical properties are only beginning to be explored.[44, 47-49] Our group focuses on metal-cation-bridged POM frameworks derived from the Preyssler polyoxotungstate, $[NaP_5W_{30}O_{110}]^{14-}$ (**Figure 1.5**). These materials maintain the advantage of the rich redox chemistry of POMs and add tunability with the bridging metal ion[48, 50] or with the assembly architecture.[50] This class of materials has the potential to bridge the gap between molecular and solid-state metal oxides. The exceptional air-stability of a TM-linked POM-based frameworks will be discussed in Chapter 4. The methods developed for electron-quantification in photodoped colloidal nanocrystals allow for quantification of the electron density in POM-based frameworks.

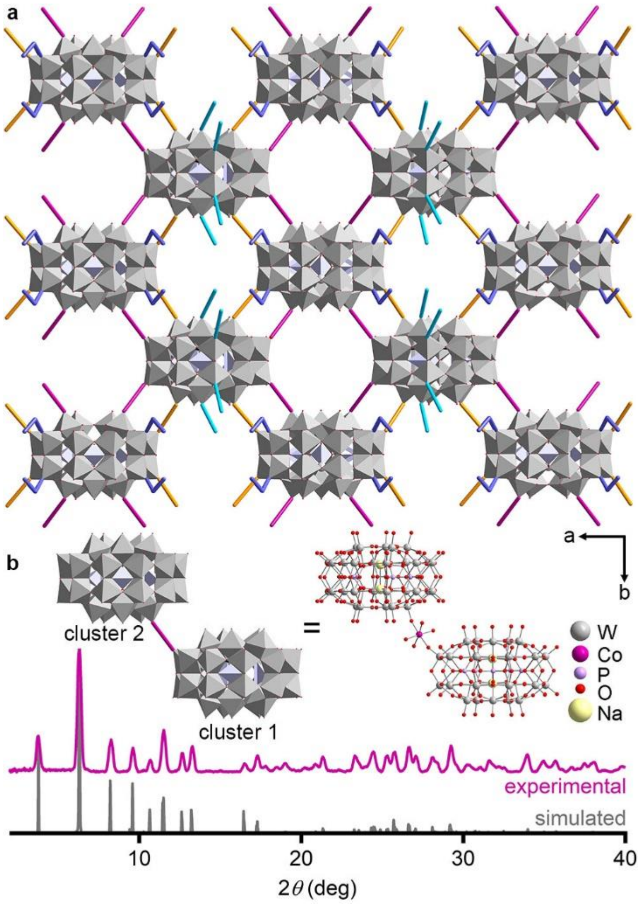

Figure 1.5. (a) Crystal structure of Co^{2+}-bridged $[NaP_5W_{30}O_{110}]^{14-}$ framework extending in the *ab* lattice plane. Water and charge-compensating cations removed for clarity. **(b)** Experimental and simulated pXRD patterns. From ref. 48.

1.6 References

1. Solymar, L.; Walsh, D., *Electrical Properties of Materials*. 7th ed.; Oxford University Press: Oxford ; New York, 2004.

2. Voznyy, O., Mobile Surface Traps in CdSe Nanocrystals with Carboxylic Acid Ligands. *J. Phys. Chem. C* **2011,** *115* (32), 15927.

3. Milliron, D. J., The Surface Plays a Core Role. *Nat. Mater.* **2014,** *13* (8), 772.

4. Nagpal, P.; Klimov, V. I., Role of Mid-Gap States in Charge Transport and Photoconductivity in Semiconductor Nanocrystal Films. *Nat. Commun.* **2011,** *2*, 486.

5. Gai, Y. Q.; Peng, H. W.; Li, J. B., Electronic Properties of Nonstoichiometric PbSe Quantum Dots from First Principles. *J. Phys. Chem. C* **2009,** *113* (52), 21506.

6. Kim, D.; Kim, D. H.; Lee, J. H.; Grossman, J. C., Impact of Stoichiometry on the Electronic Structure of PbS Quantum Dots. *Phys. Rev. Lett.* **2013,** *110* (19), 196802.

7. Zhitomirsky, D.; Voznyy, O.; Levina, L.; Hoogland, S.; Kemp, K. W.; Ip, A. H.; Thon, S. M.; Sargent, E. H., Engineering Colloidal Quantum Dot Solids Within and Beyond the Mobility-Invariant Regime. *Nat. Commun.* **2014,** *5*, 3803.

8. Schimpf, A. M.; Lounis, S. D.; Runnerstrom, E. L.; Milliron, D. J.; Gamelin, D. R., Redox Chemistries and Plasmon Energies of Photodoped In_2O_3 and Sn-Doped In_2O_3 (ITO) Nanocrystals. *J. Am. Chem. Soc.* **2015,** *137* (1), 518.

9. Kanehara, M.; Koike, H.; Yoshinaga, T.; Teranishi, T., Indium Tin Oxide Nanoparticles with Compositionally Tunable Surface Plasmon Resonance Frequencies in the Near-IR Region. *J. Am. Chem. Soc.* **2009,** *131* (49), 17736.

10. Chen, L.; Hu, H.; Chen, Y.; Gao, J.; Li, G., Plasmonic $Cu_{2-x}S$ nanoparticles: a brief introduction of optical properties and applications. *Mater. Adv.* **2021,** *2* (3), 907.

11. Lesnyak, V.; Brescia, R.; Messina, G. C.; Manna, L., Cu Vacancies Boost Cation Exchange Reactions in Copper Selenide Nanocrystals. *J. Am. Chem. Soc.* **2015,** *137* (29), 9315.

12. Kriegel, I.; Rodríguez-Fernández, J.; Wisnet, A.; Zhang, H.; Waurisch, C.; Eychmüller, A.; Dubavik, A.; Govorov, A. O.; Feldmann, J., Shedding Light on Vacancy-Doped Copper Chalcogenides: Shape-Controlled Synthesis, Optical Properties, and Modeling of Copper Telluride Nanocrystals with Near-Infrared Plasmon Resonances. *ACS Nano* **2013,** *7* (5), 4367.

13. Bekenstein, Y.; Vinokurov, K.; Keren-Zur, S.; Hadar, I.; Schilt, Y.; Raviv, U.; Millo, O.; Banin, U., Thermal Doping by Vacancy Formation in Copper Sulfide Nanocrystal Arrays. *Nano Lett.* **2014,** *14* (3), 1349.

14. Luther, J. M.; Jain, P. K.; Ewers, T.; Alivisatos, A. P., Localized Surface Plasmon Resonances Arising From Free Carriers in Doped Quantum Dots. *Nat. Mater.* **2011,** *10* (5), 361.

15. Scotognella, F.; Della Valle, G.; Kandada, A. R. S.; Dorfs, D.; Zavelani-Rossi, M.; Conforti, M.; Miszta, K.; Comin, A.; Korobcheyskaya, K.; Lanzani, G.; Manna, L.; Tassone, F., Plasmon Dynamics in Colloidal $Cu_{2-x}Se$ Nanocrystals. *Nano Lett.* **2011,** *11* (11), 4711.

16. Hartstein, K. H.; Brozek, C. K.; Hinterding, S. O. M.; Gamelin, D. R., Copper-Coupled Electron Transfer in Colloidal Plasmonic Copper-Sulfide Nanocrystals Probed by in Situ Spectroelectrochemistry. *J. Am. Chem. Soc.* **2018,** *140* (9), 3434.

17. Oh, S. J.; Berry, N. E.; Choi, J. H.; Gaulding, E. A.; Paik, T.; Hong, S. H.; Murray, C. B.; Kagan, C. R., Stoichiometric Control of Lead Chalcogenide Nanocrystal Solids to Enhance Their Electronic and Optoelectronic Device Performance. *ACS Nano* **2013,** *7* (3), 2413.

18. Shim, M.; Guyot-Sionnest, P., *N*-type Colloidal Semiconductor Nanocrystals. *Nature* **2000,** *407* (6807), 981.

19. Koh, W. K.; Koposov, A. Y.; Stewart, J. T.; Pal, B. N.; Robel, I.; Pietryga, J. M.; Klimov, V. I., Heavily Doped *n*-type PbSe and PbS Nanocrystals Using Ground-State Charge Transfer From Cobaltocene. *Sci. Rep.* **2013,** *3*, 2004.

20. Carroll, G. M.; Schimpf, A. M.; Tsui, E. Y.; Gamelin, D. R., Redox Potentials of Colloidal *n*-Type ZnO Nanocrystals: Effects of Confinement, Electron Density, and Fermi-Level Pinning by Aldehyde Hydrogenation. *J. Am. Chem. Soc.* **2015,** *137* (34), 11163.

21. Schimpf, A. M.; Knowles, K. E.; Carroll, G. M.; Gamelin, D. R., Electronic Doping and Redox-Potential Tuning in Colloidal Semiconductor Nanocrystals. *Acc. Chem. Res.* **2015,** *48* (7), 1929.

22. Schimpf, A. M.; Gunthardt, C. E.; Rinehart, J. D.; Mayer, J. M.; Gamelin, D. R., Controlling Carrier Densities in Photochemically Reduced Colloidal ZnO Nanocrystals: Size Dependence and Role of the Hole Quencher. *J. Am. Chem. Soc.* **2013,** *135* (44), 16569.

23. Rinehart, J. D.; Schimpf, A. M.; Weaver, A. L.; Cohn, A. W.; Gamelin, D. R., Photochemical Electronic Doping of Colloidal CdSe Nanocrystals. *J. Am. Chem. Soc.* **2013,** *135* (50), 18782.

24. Schrauben, J. N.; Hayoun, R.; Valdez, C. N.; Braten, M.; Fridley, L.; Mayer, J. M., Titanium and Zinc Oxide Nanoparticles Are Proton-Coupled Electron Transfer Agents. *Science* **2012,** *336* (6086), 1298.

25. Liu, W. K.; Whitaker, K. M.; Kittilstved, K. R.; Gamelin, D. R., Stable Photogenerated Carriers in Magnetic Semiconductor Nanocrystals. *J. Am. Chem. Soc.* **2006,** *128* (12), 3910.

26. Joost, U.; Sutka, A.; Oja, M.; Smits, K.; Dobelin, N.; Loot, A.; Jarvekulg, M.; Hirsimaki, M.; Valden, M.; Nommiste, E., Reversible Photodoping of TiO_2 Nanoparticles for Photochromic Applications. *Chem. Mater.* **2018,** *30* (24), 8968.

27. Shirasaki, Y.; Supran, G. J.; Bawendi, M. G.; Bulovic, V., Emergence of Colloidal Quantum-Dot Light-Emitting Technologies. *Nat. Photonics* **2013,** *7* (1), 13.

28. Yang, Y. X.; Zheng, Y.; Cao, W. R.; Titov, A.; Hyvonen, J.; Manders, J. R.; Xue, J. G.; Holloway, P. H.; Qian, L., High-Efficiency Light-Emitting Devices Based on Quantum Dots With Tailored Nanostructures. *Nat. Photonics* **2015,** *9* (4), 259.

29. Choi, M. K.; Yang, J.; Kang, K.; Kim, D. C.; Choi, C.; Park, C.; Kim, S. J.; Chae, S. I.; Kim, T. H.; Kim, J. H.; Hyeon, T.; Kim, D. H., Wearable Red-Green-Blue Quantum Dot Light-Emitting Diode Array Using High-Resolution Intaglio Transfer Printing. *Nat. Commun.* **2015,** *6*, 7149.

30. Konstantatos, G.; Badioli, M.; Gaudreau, L.; Osmond, J.; Bernechea, M.; de Arquer, F. P. G.; Gatti, F.; Koppens, F. H. L., Hybrid Graphene-Quantum Dot Phototransistors With Ultrahigh Gain. *Nat. Nanotechnol.* **2012,** *7* (6), 363.

31. Konstantatos, G.; Howard, I.; Fischer, A.; Hoogland, S.; Clifford, J.; Klem, E.; Levina, L.; Sargent, E. H., Ultrasensitive Solution-Cast Quantum Dot Photodetectors. *Nature* **2006,** *442* (7099), 180.

32. McDonald, S. A.; Konstantatos, G.; Zhang, S. G.; Cyr, P. W.; Klem, E. J. D.; Levina, L.; Sargent, E. H., Solution-Processed PbS Quantum Dot Infrared Photodetectors and Photovoltaics. *Nat. Mater.* **2005,** *4* (2), 138.

33. Deng, Z. Y.; Jeong, K. S.; Guyot-Sionnest, P., Colloidal Quantum Dots Intraband Photodetectors. *ACS Nano* **2014,** *8* (11), 11707.

34. Yuan, M. J.; Voznyy, O.; Zhitomirsky, D.; Kanjanaboos, P.; Sargent, E. H., Synergistic Doping of Fullerene Electron Transport Layer and Colloidal Quantum Dot Solids Enhances Solar Cell Performance. *Adv. Mater.* **2015,** *27* (5), 917.

35. Labelle, A. J.; Thon, S. M.; Masala, S.; Adachi, M. M.; Dong, H. P.; Farahani, M.; Ip, A. H.; Fratalocchi, A.; Sargent, E. H., Colloidal Quantum Dot Solar Cells Exploiting Hierarchical Structuring. *Nano Lett.* **2015,** *15* (2), 1101.

36. Huynh, W. U.; Dittmer, J. J.; Alivisatos, A. P., Hybrid Nanorod-Polymer Solar Cells. *Science* **2002,** *295* (5564), 2425.

37. Nanocrystals in Their Prime. *Nat. Nanotechnol.* **2014,** *9* (5), 325.

38. Murray, C. B.; Norris, D. J.; Bawendi, M. G., Synthesis and Characterization of Nearly Monodisperse CdE (E = S, Se, Te) Semiconductor Nanocrystallites. *J. Am. Chem. Soc.* **1993,** *115* (19), 8706.

39. Peng, X. G.; Manna, L.; Yang, W. D.; Wickham, J.; Scher, E.; Kadavanich, A.; Alivisatos, A. P., Shape Control of CdSe Nanocrystals. *Nature* **2000,** *404* (6773), 59.

40. Ithurria, S.; Dubertret, B., Quasi 2D Colloidal CdSe Platelets with Thicknesses Controlled at the Atomic Level. *J. Am. Chem. Soc.* **2008,** *130* (49), 16504.

41. Lan, X. Z.; Masala, S.; Sargent, E. H., Charge-Extraction Strategies for Colloidal Quantum Dot Photovoltaics. *Nat. Mater.* **2014,** *13* (3), 233.

42. Kairdolf, B. A.; Smith, A. M.; Stokes, T. H.; Wang, M. D.; Young, A. N.; Nie, S. M., Semiconductor Quantum Dots for Bioimaging and Biodiagnostic Applications. *Annu. Rev. Anal. Chem.* **2013,** *6*, 143.

43. Long, D. L.; Tsunashima, R.; Cronin, L., Polyoxometalates: Building Blocks for Functional Nanoscale Systems. *Angew. Chem. Int. Edit.* **2010,** *49* (10), 1736.

44. Miras, H. N.; Vila-Nadal, L.; Cronin, L., Polyoxometalate Based Open-Frameworks (POM-OFs). *Chem. Soc. Rev.* **2014,** *43* (16), 5679.

45. Long, D. L.; Burkholder, E.; Cronin, L., Polyoxometalate Clusters, Nanostructures and Materials: From Self Assembly to Designer Materials and Devices. *Chem. Soc. Rev.* **2007,** *36* (1), 105.

46. Petel, B. E.; Brennessel, W. W.; Matson, E. M., Oxygen-Atom Vacancy Formation at Polyoxovanadate Clusters: Homogeneous Models for Reducible Metal Oxides. *J. Am. Chem. Soc.* **2018,** *140* (27), 8424.

47. Boyd, T.; Mitchell, S. G.; Gabb, D.; Long, D. L.; Song, Y. F.; Cronin, L., POMzites: A Family of Zeolitic Polyoxometalate Frameworks from a Minimal Building Block Library. *J. Am. Chem. Soc.* **2017,** *139* (16), 5930.

48. Turo, M. J.; Chen, L. F.; Moore, C. E.; Schimpf, A. M., Co^{2+}-Linked $[NaP_5W_{30}O_{110}]^{14-}$: A Redox-Active Metal Oxide Framework with High Electron Density. *J. Am. Chem. Soc.* **2019,** *141* (11), 4553.

49. Chen, L.; San, K. A.; Turo, M. J.; Gembicky, M.; Fereidouni, S.; Kalaj, M.; Schimpf, A. M., Tunable Metal Oxide Frameworks via Coordination Assembly of Preyssler-Type Molecular Clusters. *J. Am. Chem. Soc.* **2019,** *141* (51), 20261.

50. Chen, L. F.; Turo, M. J.; Gembicky, M.; Reinicke, R. A.; Schimpf, A. M., Cation-Controlled Assembly of Polyoxotungstate-Based Coordination Networks. *Angew. Chem. Int. Edit.* **2020,** *59* (38), 16609.

Chapter 2: Photochemical Reduction of Nanocrystalline Maghemite to Magnetite

2.1. Abstract

We present a photochemical conversion method for the inverse spinel iron oxides, in which the mixed-valent magnetite phase (Fe_3O_4) is accessed from the maghemite phase (γ-Fe_2O_3) phase via a stable, colloidal nanocrystal-to-nanocrystal transformation. Anaerobic UV-irradiation of colloidal γ-Fe_2O_3 nanocrystals in the presence of ethanol as a sacrificial reductant yields reduction of some Fe^{3+} to Fe^{2+}, resulting in a topotactic reduction of γ-Fe_2O_3 to Fe_3O_4. This reduction is evidenced by the emergence of charge-transfer absorption and increased *d*-spacing in UV-irradiated nanocrystals. Redox titrations reveal that ~43 % of Fe in $\langle d \rangle$ = 4.8 nm nanocrystals can be reduced with this method, and comparison of optical data suggests similar reduction levels in $\langle d \rangle$ = 7.3 and 9.0 nm nanocrystals. Addition of excess acetaldehyde during photoreduction shows that the extent of reduction is likely pinned by the hydrogenation of acetaldehyde back to ethanol and can be increased with the use of alkylborohydride sacrificial reductants. Photochemical reduction is accompanied by increased magnetization and emergence of magnetic features characteristic of Fe_3O_4. This work provides a reversible, post-synthetic strategy to obtain Fe_3O_4 nanocrystals with well-controlled Fe^{2+} compositions.

2.2. Introduction

Superparamagnetic iron oxide nanocrystals, particularly magnetite (Fe_3O_4) and maghemite (γ-Fe_2O_3), have been extensively studied[1-5] due to their potential use in myriad technologies, including magnetoresistive devices,[6-13] biomedical diagnostics and treatments,[14-17] and water purification.[18-21] Phase-selective synthesis and use of these nanomaterials, however, is often challenging because Fe_3O_4 easily oxidizes to γ-Fe_2O_3 under ambient conditions, resulting in mixed phases and/or loss of desired properties. For example, γ-Fe_2O_3 has a lower overall magnetic moment and decreased magnetocrystalline anisotropy compared to Fe_3O_4. Additionally, Fe_3O_4 can exhibit half-metallicity with a high degree of spin-polarization, while γ-Fe_2O_3 is electrically insulating. These properties make Fe_3O_4 more desirable for incorporation into spin transport devices. exhibits a half-metallic nature with a partially filled spin-polarized band, while γ-Fe_2O_3 is electrically insulating. These properties make Fe_3O_4 more desirable for incorporation into spin transport devices. Furthermore, catalytic degradation of organic pollutants requires the oxidation of Fe^{2+},[19] not natively present in γ-Fe_2O_3. Here, we present a method to photochemically transform γ-Fe_2O_3 or Fe_3O_4/γ-Fe_2O_3 mixtures into Fe_3O_4, enabling reversible, post-synthetic switching between the two phases.

Both Fe_3O_4 and γ-Fe_2O_3 crystallize in an inverse spinel structure, $B(AB)X_4$. In the case of Fe_3O_4, 1/3 of Fe cations are in the +2 oxidation state (the "A" cations) and occupy primarily octahedral (O_h) sites, while 2/3 are in the +3 oxidation state and are distributed equally between O_h and tetrahedral (T_d) sites (the "B" cations). γ-Fe_2O_3 is often described as Fe^{2+}-deficient Fe_3O_4 ($Fe_{3-3\delta}O_4$, $\delta = 1/3$) because the 16 O_h sites in the unit cell are replaced by 40/3 Fe^{3+} and 8/3 vacancies. The structural similarity of these phases enables easy topotaxial oxidation of Fe_3O_4 to γ-Fe_2O_3,[22-31] which occurs even faster in nanocrystals than in the bulk due to the relatively high surface area. Consequently, nanostructures of these iron oxides often contain a mixture of Fe_3O_4 and γ-Fe_2O_3.[2, 22, 30-38] Many studies have focused on evaluating the extent and/or mechanism of oxidation in Fe_3O_4/γ-Fe_2O_3 nanocrystals,[2, 13, 22, 27, 30, 32-38] but direct reduction of γ-Fe_2O_3 has rarely been successfully employed as a strategy for accessing Fe_3O_4 nanocrystals.[39-41] For example, the addition of excess catechol-type ligands to γ-Fe_2O_3 leads to only partial reduction, likely occurring at the surface while maintaining an oxidized γ-Fe_2O_3 core.[39]

Photochemical reduction has been used to introduce band-like charge-carriers into various metal oxide nanocrystals, including ZnO,[42-45] TiO_2,[45-46] and In_2O_3,[42] with a mild sacrificial reductant, such as ethanol (EtOH). In this process (eq 1), UV illumination excites an electron across the metal-oxide nanocrystals (NC) bandgap and the strong oxidizing power of the photogenerated valence-band hole (h^+_{VB}) leads to oxidation of EtOH to acetaldehyde (CH_3CHO), which is irreversible unless more reducing potentials are accessed. The overall reaction deposits conduction-band electrons (e^-_{CB}) and charge-compensating protons. Notably, when ZnO nanocrystals are doped with Fe^{3+}, UV irradiation leads to localized reduction to Fe^{2+} prior to accumulation of delocalized electrons.[47-48] These results, along with the similarly high oxidizing power of the γ-Fe_2O_3 valence band suggest that photochemical reduction of Fe^{3+} in γ-Fe_2O_3 should be feasible. Indeed, UV irradiation of Fe_3O_4 nanomaterials has been exploited for the in-situ reduction of surface Fe^{3+} for Fenton-like reactions[49-53] used in the catalytic degradation of wastewater contaminants. Here, we show that photo-oxidation of EtOH can be used to access Fe_3O_4 nanocrystals from γ-Fe_2O_3 or Fe_3O_4/γ-Fe_2O_3 mixtures.

$$e^-_{CB},h^+_{VB}{:}\mathrm{NC} + CH_3CH_2OH \rightarrow 2e^-_{CB}{:}\mathrm{NC} + 2H^+ + CH_3CHO \qquad (1)$$

2.3 Results and Discussion

Colloidal γ-Fe_2O_3 nanocrystals were synthesized via thermal decomposition of iron pentacarbonyl in a mixture of oleic acid and a dialkyl ether (R_2O; R = octyl or benzyl).[54] This synthesis yields nanocrystals with mixtures of Fe_3O_4 and γ-Fe_2O_3, likely in a core/shell architecture.[33] which where oxidized to γ-Fe_2O_3 by additional heating in air. The resulting γ-Fe_2O_3 nanocrystals were photodoped following procedures used for other colloidal metal oxide nanocrystals.[42-46] Briefly, anaerobic solutions of the nanocrystals (~1 mM Fe) in toluene/THF (1/1) containing 124 EtOH/Fe as a sacrificial reductant were irradiated using a 365 nm LED (0.5 W/cm^2). The absorption was measured periodically, and samples were considered to be maximally photoreduced when the absorption stopped changing over ~30 min. **Figure 2.1a** shows the electronic absorption spectra (top) and differential absorption (bottom) of a solution of $\langle d \rangle = 4.8$ nm nanocrystals with increasing exposure to UV irradiation (following the direction of arrows). Prior to UV irradiation, the solution is yellow (**Figure 2.1a**, inset, left) and shows absorption only above 2.0 eV, corresponding to the bandgap of maghemite derived from O(2*p*)→Fe(3*d*) transitions.[55] Following UV irradiation, the nanocrystal solutions turn dark brown (**Figure 2.1a**, inset, right) due to new near-IR and visible absorption. These new features are consistent with the intervalence charge transfer (IVCT) and intersublattice charge transfer (ISCT) absorption characteristic of Fe_3O_4.[55-57] Concomitant with a growth in near-IR/visible absorption, a decrease in the absorption above 3.0 eV is observed. This decrease in the O(2*p*)→Fe(3*d*) transition in consistent with a greater ratio of Fe^{2+}/Fe^{3+}, as is expected for the reduction of γ-Fe_2O_3 to Fe_3O_4. These spectroscopic changes mirror those observed when Fe_3O_4 nanocrystals are chemically oxidized to γ-Fe_2O_3.[24]

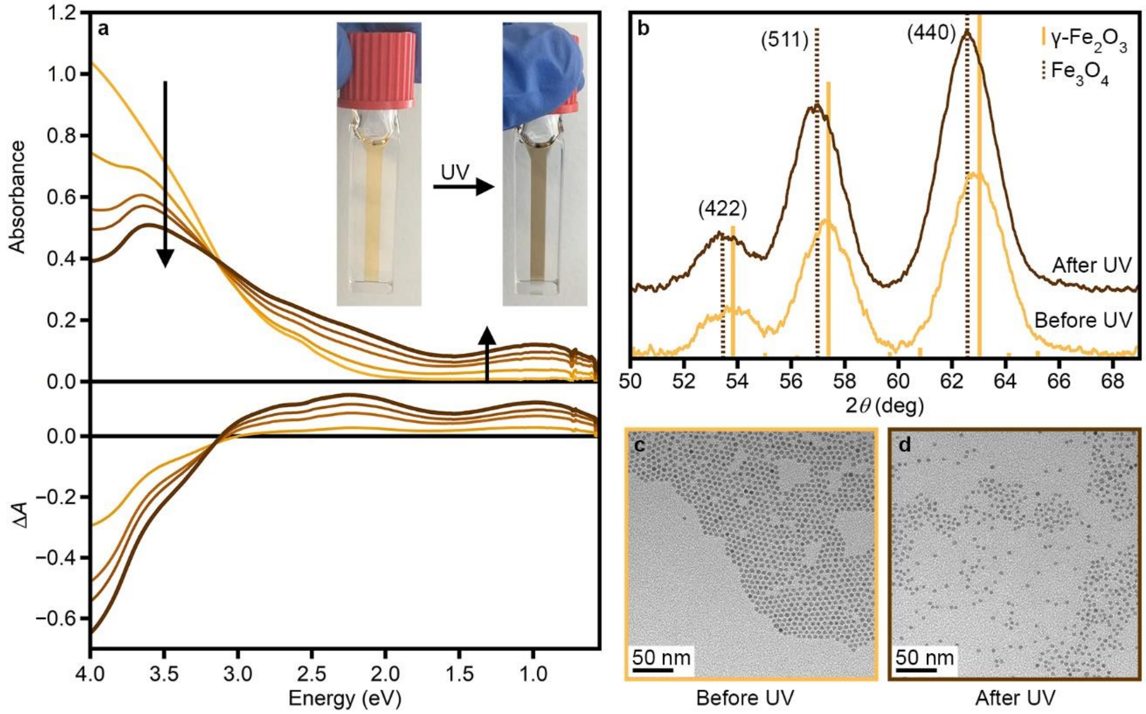

Figure 2.1. Photochemical conversion of γ-Fe_2O_3 to Fe_3O_4 in <*d*> = 4.8 nm nanocrystals. **(a)** Absorption spectra of nanocrystals ([Fe] = 1.0 mM) with increasing UV irradiation. Inset: Photographs of the colloidal suspension before (left) and after (right) 3 h UV irradiation show a color change from yellow to brown. **(b)** pXRD patterns before (yellow) and after (brown) 3 h UV irradiation. Simulated patterns for γ-Fe_2O_3 (solid yellow)[58] and Fe_3O_4 (dashed brown)[59] are shown for reference. All patterns are plotted for diffraction of Cu Kα radiation (1.5406 Å). TEM images of nanocrystals **(c)** before and **(d)** after 3 h UV irradiation. Size-distributions are provided in **Figure A.2**.

Changes in the iron oxide structure before and after photochemical reduction were monitored by pXRD. **Figure 2.1b** shows a comparison of the (422), (511) and (440) reflections before (yellow) and after 3 h UV irradiation (brown). Full powder patterns (2θ = 10–80°) are provided in **Figure A.1.** Following UV irradiation, all resolvable reflections shift to lower values of 2θ (**Table A.1**), consistent with the larger unit cell of Fe_3O_4 compared to γ-Fe_2O_3 (**Table A.2**). Importantly, transmission electron microscopy (TEM) reveals no change in the size or size-distribution of the nanocrystals after UV irradiation (**Figure 2.1c,d** and **A.2**). When the same method was used with <*d*> = 9.0 nm maghemite nanocrystals, absorption spectroscopy (**Figure A.3a**) pXRD (**Figure A.3b**) and Raman spectroscopy[4, 60] (**Figure A.4**) revealed analogous conversion to magnetite.

To determine the extent of reduction, photoreduced nanocrystals were titrated using methods similar to those developed for other photodoped metal oxide nanocrystals[42, 44-45, 61] and frameworks.[62] Specifically, the incremental addition of copper(II) triflate ($Cu[OTf]_2$) leads to a decrease in the absorbance below 3.0 eV and a recovery of the bleach above 3.0 eV (**Figure 2.2**). Spectra are plotted as the differential absorption and extinction ($\Delta A = A - A_{\text{BeforeUV}}$ and $\Delta\varepsilon = \varepsilon - \varepsilon_{\text{BeforeUV}}$, respectively). The integrated intensity of the IVCT/ISCT absorbance (0.8–3.0 eV) was plotted as a function of Cu^{2+}/Fe (**Figure 2.2**, inset). Up to ~0.2 Cu^{2+}/Fe, the absorption decreases linearly with Cu^{2+} addition. Further addition of Cu^{2+} leads to very little change in the absorption spectra (**Figure A.5**). Similar results are seen even with the use of a stronger oxidant (Ce^{4+}, **Figure A.6**). These observations suggest that a subset of the Fe is more stably reduced to Fe^{2+} or is kinetically more difficult to re-oxidize. This subset is comparable to the subset of Fe^{2+} in the as-synthesized nanocrystals (**Figure A.7**), which are expected to contain a $Fe_3O_4/\gamma\text{-}Fe_2O_3$ core/shell structure.[54] Heating of the nanocrystal solutions containing 0.58 equiv Cu^{2+}/Fe lead to further recovery of the initial spectroscopic features (**Figure A.5**) but could not be performed for extended times without solvent evaporation. The ratio of Fe^{2+} was thus estimated by extrapolating the fit of the linear regime. A similar method was used for the titration of free electrons in $Sn^{4+}:In_2O_3$ nanocrystals, in which photodoped electrons could be removed with a mild oxidant but aliovalently introduced electrons could not.[42]

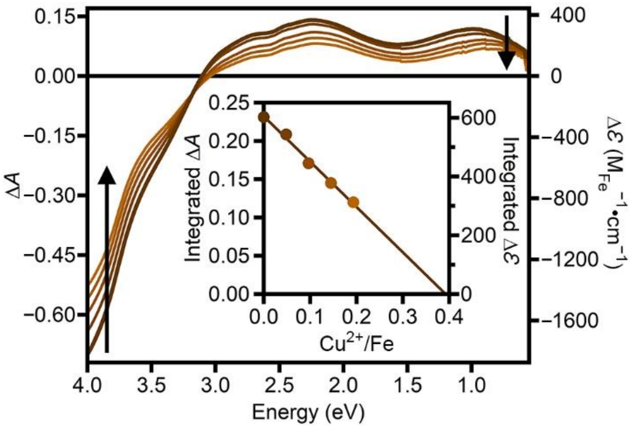

Figure 2.2 Absorption and extinction (plotted as $\Delta A = A - A_{\text{BeforeUV}}$ and $\Delta\varepsilon = \varepsilon - \varepsilon_{\text{BeforeUV}}$, respectively) spectra of photodoped <*d*> = 4.8 nm nanocrystals ([Fe] = 1.0 mM) with added $Cu[OTf]_2$. Arrows show direction of increased addition of oxidant, from 0 to ~0.2 equiv Cu^{2+}/Fe. Inset: Integrated (0.8–3.0 eV) ΔA as a function of Cu^{2+}/Fe. The linear fit is used to estimate the fraction of Fe^{2+} in the photodoped nanocrystals (39%).

A total of four titrations were conducted and the linear regime (up to ~0.2 oxidant/Fe) was extrapolated to estimate the fraction of Fe that had been reduced. Results from each titration are provided in **Table A.3**. Based on these experiments, 43 ± 3 % of Fe is in the +2 oxidation state following UV irradiation. This value is slightly greater than the fraction of Fe^{2+} in Fe_3O_4 (33 %), suggesting that photochemical reduction can be used to completely convert from γ-Fe_2O_3 to Fe_3O_4.

To confirm that photochemical reduction can occur throughout the nanocrystals and not only at the surface, various-sized nanocrystals were evaluated. **Figure 2.3** shows the differential extinction spectra (plotted as $\Delta\varepsilon = \varepsilon - \varepsilon_{\text{BeforeUV}}$) of maximally photoreduced nanocrystals with average diameters of <*d*> = 4.8 nm (dotted brown, reproduced from **Figure 2.2**), <*d*> = 7.0 nm (solid pink) and <*d*> = 9.0 nm (dashed blue). If reduction were only happening at the surface, a systematic decrease in $\Delta\varepsilon$ would be expected for increasing nanocrystal size due to decreasing surface-area/volume. A lack of such trend suggests that the reduction can penetrate the volume of the nanocrystal for the sizes investigated here. It is worth noting that ensembles with larger average sizes were photoreduced more slowly (**Figure 2.3**, inset; **Table A.2**), possibly due to slow charge-diffusion from the surface into the nanocrystal volume.

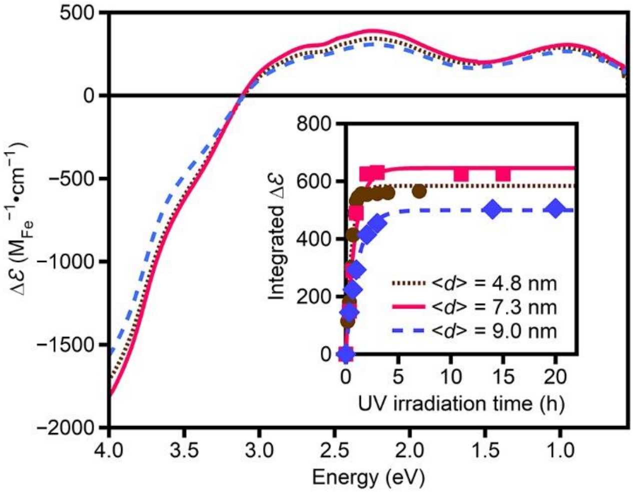

Figure 2.3. Extinction spectra ($\Delta\varepsilon = \varepsilon - \varepsilon_{BeforeUV}$) of maximally photodoped <*d*> = 4.8 nm (brown circles), <*d*> = 7.3 nm (pink squares) and <*d*> = 9.0 nm (blue diamonds) nanocrystals. Inset: Integrated extinction as a function of time.

It has been shown previously that degenerate photodoping of ZnO nanocrystals with EtOH as the sacrificial reductant is pinned by the hydrogenation of acetaldehyde to EtOH, which is the reverse of the EtOH photooxidation reaction.[42] To test if this is also the limiting factor for iron oxide reduction, γ-Fe_2O_3 nanocrystals were photodoped in the presence of various amounts of added acetaldehyde (**Figure A.8**). Here, the integrated IVCT/ISCT intensity (0.8–3.0 eV) is used to represent the level of photoreduction. Similar to the photodoping of ZnO nanocrystals, the maximum photoreduction decreases with added acetaldehyde, suggesting that acetaldehyde hydrogenation can limit the photoreduction of γ-Fe_2O_3.

It has also been shown in ZnO nanocrystals that the use of alkylborohydrides as sacrificial reductants leads to an increase in the maximum photodoping level.[44] In the case of γ-Fe_2O_3, addition of ~50 equiv $LiEt_3BH$/Fe led to direct reduction of <*d*> = 4.8 nm nanocrystals, even without UV irradiation (**Figure A.9i**). This level of reduction is comparable to the maximum level of photoreduction achieved using EtOH as the sacrificial reductant (**Figure A.9ii**). UV irradiation of the $LiEt_3BH$-reduced sample leads to further spectroscopic changes (**Figure A.9iii**), which are distinct from those observed with EtOH. Namely, the lowest energy transition (~1.0 eV) blueshifts, which was not observed for photochemical reduction with EtOH (**Figure 2.1a**). Additionally, a large bleach of the absorbance above ~2.2 eV leads to the loss of the isosbestic point, normally observed at ~3.1 eV (**Figure 2.1a**).[24] These changes make quantification of reduction by integrated intensity unreliable but may suggest reduction beyond the pure Fe_3O_4 phase. No new phase was observable by pXRD, however (**Figure A.10**).

Finally, changes in the magnetic behavior upon photoreduction were monitored using superconducting quantum interference device (SQUID) magnetometry. For these measurements, anaerobic nanocrystal solutions (~50 mg, 10–20 mM) in toluene/THF/EtOH (75/75/1) were sealed in a quartz tube. Magnetic data were collected on the as-prepared sample ("Before UV") and after varying UV irradiation times (**Figure 2.4**). Importantly, the magnetization vs field (M vs H, **Figure 2.4a**) reveals an increase in the saturation magnetization (M_s) from 70 to 110 emu/g (an increase of 57 %) following 6.5 h UV irradiation. This increase is consistent with phase-conversion to Fe_3O_4, in which the presence of Fe^{2+} contributes to higher magnetization due to ferromagnetic coupling with Fe^{3+} via double-exchange.[63-64] A similar, reverse trend has been observed upon the partial chemical oxidation of Fe_3O_4 to γ-Fe_2O_3.[65] Notably, there is negligible exchange bias (H_E) observed before and after UV irradiation (**Table A.5**), suggesting that reduction is distributed throughout the $<d>$ = 4.8 nm nanocrystals.

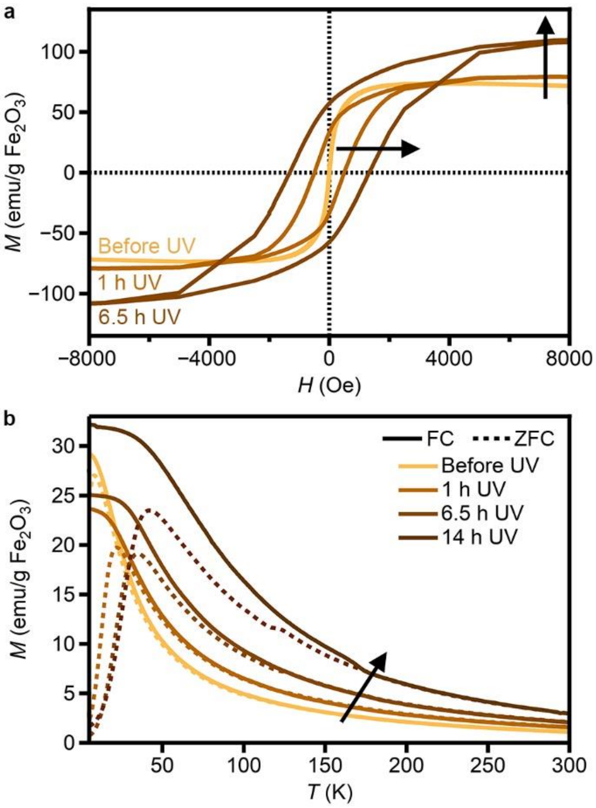

Figure 2.4. Magnetic behavior of <*d*> = 4.8 nm nanocrystals before and after varying UV irradiation times. Magnetization as a function of **(a)** applied field at 5 K and **(b)** temperature for field-cooled (FC, solid lines, 100 Oe) and zero-field-cooled (ZFC, dashed lines) samples. Arrows show changes with increasing UV irradiation.

The increase in magnetization is accompanied by (a) an opening of the hysteresis loop and an increase in the coercive field (H_c) from 14 to 1320 Oe (**Figure 2.4a**) and (b) an increase in the blocking temperature (T_b), here defined as the maximum point of the zero-field-cooled (ZFC) curve in *M* vs temperature (*T*) measurements, from 6 to 35 K (**Figure 2.4b**). These increases are consistent with the larger intrinsic magnetocrystalline anisotropy of Fe_3O_4.[66-67] Further UV irradiation of the <*d*> = 4.8 nm nanocrystals leads to the emergence of a feature at ~120 K, consistent with the Verwey transition[68-70] (**Figure 2.4b**). The emergence of a Verwey transition with photochemical reduction is notable, as previous studies have shown that this transition is generally suppressed for nanocrystals with $<d> < 20$ nm and completely disappears when $<d> < 6$ nm due to the high percentage of surface sites that can easily host defects.[71]

Similar trends in M_s, H_c and T_b are seen following UV irradiation of larger ($<d> = 9.0$ nm) nanocrystals (**Figure A.11**). These nanocrystals, however, display significant H_E following UV irradiation (**Table A.5**), which may suggest that photoreduction proceeds more heterogeneously in larger nanocrystals. The sharp magnetization feature at ~200 K in the most reduced nanocrystals (**Figure A.11b**) indicates the presence of a subpopulation of the further-reduced antiferromagnetic wüstite phase ($Fe_{1-x}O$; Neél temperature, $T_N \sim 200$ K).[72-73] The dominant superparamagnetic behavior (**Figure A.9b**) suggests that that the fraction $Fe_{1-x}O$ is small, and this phase is not observed by pXRD (**Figure A.12**).

Based on the crystal structures of Fe_3O_4 and γ-Fe_2O_3, the reduction of Fe^{3+} in γ-Fe_2O_3 is expected to be favored at O_h A-sites. An idealized chemical equation for the photochemical reduction of γ-Fe_2O_3 ($(\mathrm{Fe}_8^{\mathrm{III}})_{\mathrm{tet}}(\mathrm{Fe}_{40/3}^{\mathrm{III}})_{\mathrm{oct}}\mathrm{O}_{32}$), in which 50% of $\mathrm{Fe}_{\mathrm{oct}}^{\mathrm{III}}$ cations (all A cations) are reduced, is presented in Scheme 1a. The reduction of $\mathrm{Fe}_{\mathrm{oct}}^{\mathrm{III}}$ cations results in a charged nanocrystal in which charge-compensation is provided by H^+ generated from MeOH oxidation (Scheme 1a(i)). The reduced nanocrystal can be rewritten in terms of a magnetite core ($(\mathrm{Fe}_8^{\mathrm{III}})_{\mathrm{tet}}(\mathrm{Fe}_8^{\mathrm{III}}\mathrm{Fe}_8^{\mathrm{II}})_{\mathrm{oct}}\mathrm{O}_{32}$) with "excess" O atoms (Scheme 1a(ii)), which likely reside on the surface and are compensated by the photogenerated H^+.

a

$$\left(\mathrm{Fe}_{8}^{\mathrm{III}}\right)_{\mathrm{tet}}\left(\mathrm{Fe}_{40/3}^{\mathrm{III}}\right)_{\mathrm{oct}}\mathrm{O}_{32}+\frac{10}{3}\mathrm{CH_3OH}\rightarrow\left[\left(\mathrm{Fe}_{8}^{\mathrm{III}}\right)_{\mathrm{tet}}\left(\mathrm{Fe}_{20/3}^{\mathrm{III}}\mathrm{Fe}_{20/3}^{\mathrm{II}}\right)_{\mathrm{oct}}\mathrm{O}_{32}\right]^{20/3-}+\frac{10}{3}\mathrm{CH_2O}+\frac{20}{3}\mathrm{H}^{+} \quad \text{(i)}$$

$$\left[\left(\mathrm{Fe}_{8}^{\mathrm{III}}\right)_{\mathrm{tet}}\left(\mathrm{Fe}_{20/3}^{\mathrm{III}}\mathrm{Fe}_{20/3}^{\mathrm{II}}\right)_{\mathrm{oct}}\mathrm{O}_{32}\right]^{20/3-}=\frac{8}{9}\left[\left\{\left(\mathbf{Fe}_{\mathbf{8}}^{\mathbf{III}}\right)_{\mathbf{tet}}\left(\mathbf{Fe}_{\mathbf{8}}^{\mathbf{III}}\mathbf{Fe}_{\mathbf{8}}^{\mathbf{II}}\right)_{\mathbf{oct}}\mathbf{O}_{\mathbf{32}}\right\}\mathrm{O}_{4}\right]^{15/2-} \quad \text{(ii)}$$

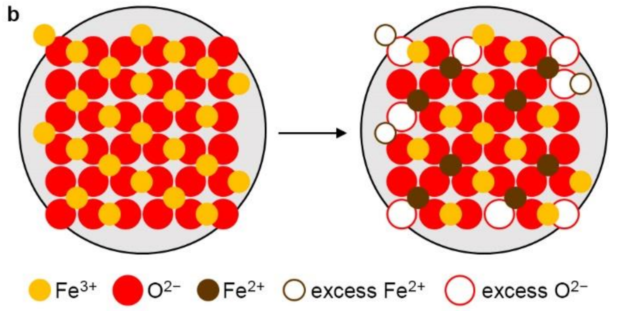

Figure 2.5. (a) Idealized chemical equations for the photochemical reduction of γ-Fe_2O_3 with MeOH. (i) The reduction of 50% $\mathrm{Fe}_{\mathrm{oct}}^{\mathrm{III}}$ results in a charged nanocrystal, with charge-compensation provided by the H^+ generated from MeOH oxidation. (ii) The reduced nanocrystal can be rewritten in terms of a magnetite core with "excess" O atoms, which likely reside on the surface and are compensated by photogenerated H^+. **(b)** Abstract schematic depiction of the reduction of γ-Fe_2O_3 to Fe_3O_4, in which some ("excess") surface atoms are no longer part of the core nanocrystalline phase.

The reduction must first happen at surface Fe, after which charge-migration can lead to reduction of Fe in the bulk of the nanocrystal. The reduction of ~43% of Fe in the nanocrystals (**Table A.3**) is slightly higher than expected for a pure reduction of γ-Fe_2O_3 to Fe_3O_4, which should result in 33% of Fe being reduced. This excess Fe reduction, however, can occur at surface Fe (Scheme 1b, "excess Fe^{2+}"), and does not necessarily imply that B-site Fe ions are reduced in the bulk of the nanocrystal. Similarly, although γ-Fe_2O_3 and Fe_3O_4 have different FeO stoichiometries, the crystal structure can be relaxed at the surface, such that some of the O atoms are no longer counted in the core nanocrystal structure (Scheme 1a(ii); Scheme 1b, "excess O^{2-}"). As depicted in Scheme 1b, excess Fe-reduction and changes in Fe/O stoichiometry can be accounted for at the surface while the bulk of the reduced nanocrystal retains the stoichiometry of Fe_3O_4.

The "over-reduction" of Fe may also be responsible for the emergence of a small fraction of $Fe_{1-x}O$, which is detectable in larger nanocrystals via the appearance of a feature near T_N (**Figure A.11b**). This phase could also be present in the smaller nanocrystals but masked due to the weakly superparamagnetic nature of small $Fe_{1-x}O$.[74] Importantly, nanocrystals are photochemically reduced to the same level, regardless of whether they start as fully oxidized (γ-Fe_2O_3) or as γ-Fe_2O_3/Fe_3O_4 mixtures (**Figure A.13**). Photochemical reduction can thus be exploited to obtain a "normalized" Fe^{2+} content. The slower ensemble reduction with increasing nanocrystal size (**Table A.4**) suggests that this method is effective over a broad size range and only limited by charge-diffusion from the surface into the nanocrystal volume. This limit provides a facile strategy for post synthetic and reversible tuning of the exchange bias in single-component iron oxide nanostructures (**Figure 2.4**, **Table A.5**).

The photochemical addition of delocalized electrons to ZnO nanocrystals has previously been shown to be pinned by aldehyde hydrogenation, which is negligible in as-prepared nanocrystals but becomes more favorable at increased electron densities.[42] The lower photochemical reduction of γ-Fe_2O_3 in the presence of added acetaldehyde (**Figure A.8**) suggests that hydrogenation of acetaldehyde could also be limiting the photochemical reduction of γ-Fe_2O_3. Catalytic hydrogenation of aldehydes by iron oxides has been reported at slightly elevated temperatures (60 °C) but requires the use of a noble metal catalyst and an atmosphere of H_2.[75-76] In our case, aldehyde hydrogenation likely becomes favorable due to an increasingly negative Fermi level with increasing Fe^{2+} content. Indeed, pre-reduction of Fe_2O_3 has been shown to increase its activity in benzaldehyde hydrogenolysis.[77]

2.4. Summary and Conclusions

We demonstrate a new strategy for controlling the oxidation state of Fe in inverse spinel iron oxide nanocrystals using photochemical reduction. Anaerobic UV irradiation of colloidal γ-Fe_2O_3 nanocrystals results in new charge-transfer absorption, increased *d*-spacing and enhanced magnetization, characteristic of a topotactic reduction to Fe_3O_4. Redox titrations reveal that ~43 % of Fe in <*d*> = 4.8 nm nanocrystals can be reduced with this method, indicating full conversion to Fe_3O_4, with excess reduction likely at the surface of the nanocrystals. As with other metal oxide nanocrystals, this photoreduction is likely pinned by the hydrogenation of acetaldehyde back to EtOH and can be increased with the use of $LiEt_3BH$ as sacrificial reductant. Reduction in the presence of EtOH proceeds to the same level, regardless of starting point, providing a post-synthetic method for obtaining well-controlled Fe^{2+} concentrations across various samples. Overall, this strategy allows for facile access to the desired properties of fully reduced Fe_3O_4 colloidal nanocrystals.

2.5. Experimental Methods

Chemicals. Chemical manufacturers and purities are given in **Table 2.1.** Toluene (tol) and tetrahydrofuran (THF) were obtained from a solvent purification system, transferred to a nitrogen-filled glovebox and stored over molecular sieves (3 Å) for 24 h prior to use.

Table 2.1. Chemicals

Chemical	Purity	Manufacturer
Chemicals used in γ-Fe_2O_3 nanocrystal synthesis		
Iron pentacarbonyl ($Fe(CO)_5$)	99.5%	Strem Chemicals
Oleic acid (OA)	>97%	Aldrich
Dioctyl ether ($C_{16}H_{34}O$)	>98%	Aldrich
Dibenzyl ether ($C_{14}H_{14}O$)	>95%	Alfa Aesar
Chemicals used for post-synthetic redox experiments		
Anhydrous ethanol (EtOH)	90%	Strem Chemicals
tert-Butyl alcohol (t-BuOH)	99.5%	Alfa Aesar
Lithium triethylborohydride ($LiEt_3BH$, 1 M in TH	1.00 M	Alfa Aesar
Copper(II) trifluoromethanesulfonate ($Cu[OTf]_2$)	99.95%	Oakwood Chemic
Ammonium cerium (IV) nitrate (CAN)	>98.0%	TCI
Acetaldehyde (CH_3CHO)	99%	Alfa Aesar
Other chemicals		
Nitric acid (HNO_3, 69%), TraceMetal grade	Fisher Chemical	
Hydrogen peroxide (H_2O_2, 31%) for ultratrace anal	Sigma Aldrich	

Nanocrystal Synthesis. Colloidal γ-Fe_2O_3 nanocrystals were prepared by thermal decomposition of iron pentacarbonyl ($Fe(CO)_5$) in the presence of oleic acid (OA), adapting a previously published synthesis.[54] In a typical synthesis of nanocrystals with <*d*> ≈ 5 nm, 10 ml dibenzyl ether (52.6 mmol) and 1.43 ml OA (4.56 mmol) were degassed in a 100-ml 3-neck round-bottom flask at 100 °C for 2 h. The solution was then placed under a nitrogen atmosphere and 0.2 ml (1.52 mmol) $Fe(CO)_5$ was rapidly injected. The resulting mixture was heated to reflux (~290 °C) at the rate of 8 °C/min and held for 1 h, after which it was cooled to room-temperature. Nanocrystals with <*d*> ≈ 7 nm were obtained using a similar method, with a faster heating rate of 3 °C/min. Nanocrystals with <*d*> ≈ 9.0 nm were obtained using a similar method, replacing dibenzyl ether with an equivalent volume of dioctyl ether (33.2 mmol) and heating at 3 °C/min. A quarter of the resulting solution was taken to prepare the as-synthesized stock solution and the remaining nanocrystals were oxidized by heating at 100 °C in air (8–48 h) until the IVCT was not visible by absorption measurements at [Fe] ~ 1 mM.

After cooling the solution to room-temperature, ~0.1 ml OA was added to the solution and the mixture was sonicated for 10 s. The nanocrystals were washed by adding EtOH to the reaction mixture and centrifuging at 15000 rpm for 5 min. The resulting pellets were resuspended in toluene/EtOH (1/3) and centrifuged again at 15000 rpm for 5 min. The addition of toluene/EtOH followed by centrifugation was repeated a total of 3 times. After the third centrifugation, the resulting pellet was dried under vacuum for 2 h on a Schlenk line, after which it was brought into a nitrogen-filled glovebox and resuspended in 10~20 ml anaerobic toluene. As-synthesized and oxidized nanocrystals were processed following the same procedure. The [Fe] of each stock solution is provided in **Table 2.2**.

Table 2.2. Preparation of anaerobic solutions for optical measurements

<*d*> (nm)	[Fe] in anaerobic stock solution (mM)	Volume of stock solution (μl)	Volume of toluene (μl)	Volume of THF (μl)	[Fe] in cuvette (mM)
4.8	21	68	682	750	0.96
7.3	30	50	700	750	1.0
9.0	41	36	714	750	0.98

Elemental analysis. 50 μl anaerobic stock solution was dried under vacuum and digested in 2 ml HNO_3/H_2O_2 (1/1) for 1 day.[78] 100 μl of the digested solution was diluted in 9.9 ml ultrapure H_2O with 5% HNO_3. 1 ml diluted solution was further diluted in 9 ml ultrapure H_2O with 5% HNO_3. Inductively coupled plasma–mass spectrometry (ICP–MS) was collected on a Thermo iCAP RQ ICP–MS.

Photoreduction for optical measurements. In a typical experiment with <*d*> = 4.8 nm nanocrystals, 68 μl anaerobic stock solution, 682 μl toluene and 750 μl THF were loaded into a 4-mm screw-cap cuvette (final [Fe] ~ 1.0 mM). To this solution, 10 μl EtOH (124 equiv per Fe) was added as a sacrificial reductant. The absorption spectrum of the as-prepared solution was collected using a Cary 5000 spectrometer. The solution was irradiated with a 365-nm LED (0.5 W/cm^2) and the absorption spectrum was monitored periodically. Nanocrystals were considered to be maximally photoreduced when no change in the absorption spectrum was observed over 30 min. Under these conditions, maximum photoreduction levels were typically reached within 2, 3, or 5 h for <*d*> = 4.8, 7.3 or 9.0 nm, respectively. For larger nanocrystals, the volume of stock solution was adjusted such that all solutions used for optical measurements had similar [Fe] (**Table 2.2**). For photoreduction with $LiEt_3BH$, 68 µl anaerobic stock solution, 682 µl toluene, and 750 µl $LiEt_3BH$ (0.1 M in THF, 54 equiv per Fe) were loaded into a 4-mm screw-cap cuvette. Addition of $LiEt_3BH$ to the nanocrystals resulted in a color-change and absorption measurements revealed reduction prior to UV irradiation.

Titrations. The cuvette containing maximally photoreduced <*d*> = 4.8 nm nanocrystals was brought into a nitrogen-filled glovebox. A solution of oxidant (0.014 M) was prepared by dissolving 41.5 mg $Cu[OTf]_2$ (0.115 mmol) or 63.0 mg CAN (0.115 mmol) in 8 ml acetonitrile in a nitrogen-filled glovebox. To the cuvette containing maximally photoreduced nanocrystals, 10 µl oxidant solution was added and mixed by vigorous shaking. After each addition, the absorption spectrum was recorded. The addition of oxidant solution was repeated until 90–100 µl was added in total. The integrated intensities (0.8–3.0 eV) of the differential absorption spectra were plotted as a function of oxidant equivalents. The first 5 data points (in which integrated intensity decreased linearly with added oxidant) were fit to a line, where the *x*-intercept was the fraction of Fe that had been oxidized (equal to the fraction of Fe^{2+}/Fe_{total}). For titrations with mild heating, the cuvette was heated on a hotplate at the lowest setting for 2 h. The temperature was measured using an IR gun to be 85 °C.

Photoreduction in the presence of acetaldehyde. In a typical experiment, 1 ml anaerobic stock solution was diluted with 10 ml toluene. From this diluted solution, 750 μl was loaded into a 4-mm screw-cap cuvette and to it was added 750 μl THF and 10 μl EtOH. This solution was the "0 equiv acetaldehyde" control. When adding acetaldehyde, the volume of THF was adjusted to maintain a constant [Fe] and total volume. Each solution was irradiated with 365-nm LED (0.5 W/cm^2) and the absorption spectrum was monitored periodically. Nanocrystals were considered to be maximally photoreduced when no change in the absorption spectrum was observed over 30 min.

Powder X-ray diffraction. For measurements on oxidized samples, nanocrystals were precipitated by adding with 0.5 ml EtOH to 0.5 ml anaerobic stock solution and collected via centrifugation at 15000 rpm for 5 min. The resulting pellets were dried under vacuum (2 h) and stored under nitrogen for 1 h prior to the measurement. For measurements on photoreduced samples, maximally photoreduced samples (1.5 ml, ~1 mM) were brought into a nitrogen-filled glovebox and precipitated with 0.5 ml EtOH in air-tight centrifuge tubes. Precipitates were collected via centrifugation at 15000 rpm for 5 min and resuspended in toluene (0.5 ml). Precipitation with EtOH followed by centrifugation was repeated a total of 3 times. After the third centrifugation, the resulting pellets were dried under vacuum (2 h) and stored under nitrogen for 1 h prior to the measurement. X-ray diffraction patterns were collected at 300 K using a Bruker Apex II Single-Crystal X-ray Diffractometer equipped with a Mo Kα radiation source (λ = 0.7107Å) and Apex II area Detector. The measurement was performed in transmission mode with detector distance of 200 mm and 3 frames collected ϕ = 0° and 45°. The first, second, and third frames were centered at 2θ = 10°, 22°, and 34°, respectively. The diffraction rings obtained from the three frames were overlaid together and radially integrated in Diffrac.eva software. Single-crystal corundum (Bruker) was used as a calibration standard. To report the reflection locations, powder patterns were fit in the range of 2θ = 26–68 deg with a cubic baseline and Gaussian peaks. Fitting was performed using the Wavemetrics Multi-Peak Fitting Package in Igor.

Transmission electron microscopy. "Before UV" sample: In a nitrogen-filled glovebox, 0.1 ml anaerobic stock solution was diluted with ~1 ml toluene. The diluted solution was removed from the glovebox and ~20 µl was drop-cast onto a 100-mesh copper TEM grid coated with formvar and carbon (Electron Microscopy Sciences). "After UV" sample: Nanocrystals were maximally photoreduced following the method used for optical measurements. Outside of the glovebox, ~20 µl photoreduced solution was removed from the cuvette and drop-cast onto the TEM grid. Grids were examined using either a JEOL JEM-1400Plus transmission electron microscope operating at 80 kV equipped with a Gatan OneView 4K digital camera ($<d> = 4.8$ nm) or a FEI Spirit microscope operating at 80 kV equipped with a 2k×2k Gatan CCD camera ($<d> = 7.3$ nm and 9.0 nm). Images were transformed into contrast-binary image files and sizing and statistical analyses were performed using the "Analyze Particles" function in ImageJ. The resulting data were histogrammed with 0.2-nm bins and fit with a Gaussian distribution.

Raman spectroscopy. "Before UV" sample: In a nitrogen-filled glovebox, 0.5 ml anaerobic stock solution was transferred to an air-tight centrifuge tube and mixed with 0.5 ml EtOH to precipitate the nanocrystals. The mixture was centrifuged at 15000 rpm for 5 min. The addition of toluene/EtOH in the glovebox followed by centrifugation was repeated a total of 3 times, after which the resulting pellet was transferred to a Si substrate.

"After UV" sample: In a nitrogen-filled glovebox, 250 µl anaerobic stock solution was transferred to a 4-mm screw-cap cuvette containing 500 µl toluene, 750 µl THF and 100 µl EtOH. The cuvette was irradiated by UV for 40 h. In the glovebox, 0.5 ml photoreduced solution was transferred to an air-tight centrifuge tube and mixed with 0.5 ml EtOH to precipitate the nanocrystals. The addition of toluene/EtOH followed by centrifugation was repeated a total of 3 times, after which the resulting pellet was transferred to a Si substrate. Raman spectra were collected on freshly prepared samples using a Renishaw inVia confocal Raman microscope with 532-nm laser-excitation (5 mW) and a 50× objective lens.

Magnetometry. 750 µl anaerobic stock solution was mixed with 750 µl THF and 10 µl EtOH. From this diluted solution, ~50 mg was loaded into a pre-massed, customized quartz tube. The mass of the loaded solution was recorded by and the tube was then sealed anaerobically using an H_2/O_2 torch. Magnetic data was collected on the as-prepared sample ("Before UV"). The quartz tube was then irradiated using a 365-nm LED (0.5 W/cm^2) and the magnetization data were collected after various irradiation times. Magnetic data were collected by a Quantum Design MPMS3 SQUID magnetometer. Field-dependent magnetization data (*M–H)* were collected at 300 K and 5K and temperature-dependent magnetization data (*M–T*) were collected at 100 Oe.

Chapter 2, in full, is a reprint of the material as it appears in **Jung, H.**, Schimpf, A. M. Photochemical reduction of nanocrystalline maghemite to magnetite. *Nanoscale*, under review. The author of this dissertation was the primary author of the material. I would like to thank Ben Zhou and Jeremy Hilgar for assistance with magnetic measurements and analysis

TEM data were collected at the UCSD Cellular and Molecular Medicine Electron Microscopy Facility (NIH 1S10OD023527) and the UCSD National Center for Microscopy and Imaging Research (NIH 1R24GM137200-01). Raman data were collected using instrumentation supported by the U. S. National Science Foundation through the UCSD Materials Research Science and Engineering Center (DMR-2011924). The authors thank Prof. J. D. Rinehart and B. H. Zhou for assistance with magnetic measurements and analysis.

References

1. Laurent, S.; Forge, D.; Port, M.; Roch, A.; Robic, C.; Elst, L. V.; Muller, R. N., Magnetic Iron Oxide Nanoparticles: Synthesis, Stabilization, Vectorization, Physicochemical Characterizations, and Biological Applications. *Chem. Rev.* **2008,** *108* (6), 2064.

2. Demortiere, A.; Panissod, P.; Pichon, B. P.; Pourroy, G.; Guillon, D.; Donnio, B.; Begin-Colin, S., Size-Dependent Properties of Magnetic Iron Oxide Nanocrystals. *Nanoscale* **2011,** *3* (1), 225.

3. Yuan, H. T.; Liu, Z. K.; Xu, G.; Zhou, B.; Wu, S. F.; Dumcenco, D.; Yan, K.; Zhang, Y.; Mo, S. K.; Dudin, P.; Kandyba, V.; Yablonskikh, M.; Barinov, A.; Shen, Z. X.; Zhang, S. C.; Huang, Y. S.; Xu, X. D.; Hussain, Z.; Hwang, H. Y.; Cui, Y.; Chen, Y. L., Evolution of the Valley Position in Bulk Transition-Metal Chalcogenides and Their Monolayer Limit. *Nano Lett.* **2016,** *16* (8), 4738.

4. Testa-Anta, M.; Ramos-Docampo, M. A.; Comesana-Hermo, M.; Rivas-Murias, B.; Salgueirino, V., Raman spectroscopy to unravel the magnetic properties of iron oxide nanocrystals for bio-related applications. *Nanoscale Adv.* **2019,** *1* (6), 2086.

5. Samrot, A. V.; Sahithya, C. S.; Selvarani A, J.; Purayil, S. K.; Ponnaiah, P., A Review on Synthesis, Characterization and Potential Biological Applications of Superparamagnetic Iron Oxide Nanoparticles. *Curr. Res. Green Sustain. Chem.* **2021,** *4,* 100042.

6. Zeng, H.; Black, C. T.; Sandstrom, R. L.; Rice, P. M.; Murray, C. B.; Sun, S. H., Magnetotransport of Magnetite Nanoparticle Arrays. *Phys. Rev. B* **2006,** *73* (2), 020402(R).

7. Chen, J.; Ye, X. C.; Oh, S. J.; Kikkawa, J. M.; Kagan, C. R.; Murray, C. B., Bistable Magnetoresistance Switching in Exchange-Coupled $CoFe_2O_4$–Fe_3O_4 Binary Nanocrystal Superlattices by Self-Assembly and Thermal Annealing. *ACS Nano* **2013,** *7* (2), 1478.

8. Kohiki, S.; Kinoshita, T.; Nara, K.; Akiyama-Hasegawa, K.; Mitome, M., Large, Negative Magnetoresistance in an Oleic Acid-Coated Fe_3O_4 Nanocrystal Self-Assembled Film. *ACS Appl. Mater. Inter.* **2013,** *5* (22), 11584.

9. Mitra, A.; Barick, B.; Mohapatra, J.; Sharma, H.; Meena, S. S.; Aslam, M., Large Tunneling Magnetoresistance in Octahedral Fe_3O_4 Nanoparticles. *AIP Adv.* **2016,** *6* (5), 055007.

10. Jiang, C. P.; Ng, S. M.; Leung, W.; Pong, P. W. T., Magnetically Assembled Iron Oxide Nanoparticle Coatings and Their Integration With Pseudo-Spin-Valve Thin Films. *J. Mater. Chem. C* **2017,** *5* (2), 252.

11. Lin, Y.; Xu, H. Y.; Wang, Z. Q.; Cong, T.; Liu, W. Z.; Ma, H. L.; Liu, Y. C., Transferable and Flexible Resistive Switching Memory Devices Based on PMMA Films With Embedded Fe_3O_4 Nanoparticles. *Appl. Phys. Lett.* **2017,** *110* (19).

12. Zhou, B. H.; Rinehart, J. D., Pseudo Spin Valve Behavior in Colloidally Prepared Nanoparticle Films. *ACS Appl. Electron. Mater.* **2019,** *1* (7), 1065.

13. Nguyen, H. H.; Ta, H. K. T.; Park, S.; Phan, T. B.; Pham, N. K., Resistive Switching Effect and Magnetic Properties of Iron Oxide Nanoparticles Embedded-Polyvinyl Alcohol Film. *RSC Adv.* **2020,** *10* (28), 12900.

14. Krishnan, K. M., Biomedical Nanomagnetics: A Spin Through Possibilities in Imaging, Diagnostics, and Therapy. *IEEE T. Magn.* **2010,** *46* (7), 2523.

15. Frimpong, R. A.; Hilt, J. Z., Magnetic Nanoparticles in Biomedicine: Synthesis, Functionalization and Applications. *Nanomedicine-UK* **2010,** *5* (9), 1401.

16. Yan, K.; Li, P. H.; Zhu, H. E.; Zhou, Y. J.; Ding, J. D.; Shen, J.; Li, Z.; Xu, Z. S.; Chu, P. K., Recent Advances in Multifunctional Magnetic Nanoparticles and Applications to Biomedical Diagnosis and Treatment. *RSC Adv.* **2013,** *3* (27), 10598.

17. Lee, N.; Yoo, D.; Ling, D.; Cho, M. H.; Hyeon, T.; Cheon, J., Iron Oxide Based Nanoparticles for Multimodal Imaging and Magnetoresponsive Therapy. *Chem. Rev.* **2015,** *115* (19), 10637.

18. Khin, M. M.; Nair, A. S.; Babu, V. J.; Murugan, R.; Ramakrishna, S., A Review on Nanomaterials for Environmental Remediation. *Energ. Environ. Sci.* **2012,** *5* (8), 8075.

19. Nidheesh, P. V., Heterogeneous Fenton Catalysts for the Abatement of Organic Pollutants From Aqueous Solution: a Review. *RSC Adv.* **2015,** *5* (51), 40552.

20. Kefeni, K. K.; Mamba, B. B.; Msagati, T. A. M., Application of Spinel Ferrite Nanoparticles in Water and Wastewater Treatment: A Review. *Sep. Purif. Technol.* **2017,** *188*, 399.

21. Luo, H. W.; Zeng, Y. F.; He, D. Q.; Pan, X. L., Application of Iron-Based Materials in Heterogeneous Advanced Oxidation Processes for Wastewater Treatment: A Review. *Chem. Eng. J.* **2021,** *407*, 127191.

22. Bogart, L. K.; Blanco-Andujar, C.; Pankhurst, Q. A., Environmental Oxidative Aging of Iron Oxide Nanoparticles. *Appl. Phys. Lett.* **2018,** *113* (13), 133701.

23. Sidhu, P. S.; Gilkes, R. J.; Posner, A. M., Mechanism of the Low Temperature Oxidation of Synthetic Magnetites. *J. Inorg. Nucl. Chem.* **1977,** *39* (11), 1953.

24. Tang, J.; Myers, M.; Bosnick, K. A.; Brus, L. E., Magnetite Fe_3O_4 Nanocrystals: Spectroscopic Observation of Aqueous Oxidation Kinetics. *J. Phys. Chem. B* **2003,** *107* (30), 7501.

25. Schwaminger, S. P.; Bauer, D.; Fraga-Garcia, P.; Wagner, F. E.; Berensmeier, S., Oxidation of Magnetite Nanoparticles: Impact on Surface and Crystal Properties. *CrystEngComm* **2017,** *19* (2), 246.

26. Ozdemir, O.; Dunlop, D. J.; Moskowitz, B. M., The Effect of Oxidation on the Verwey Transition in Magnetite. *Geophys. Res. Lett.* **1993,** *20* (16), 1671.

27. Colombo, U.; Fagherazzi, G.; Gazzarri.F; Lanzavecchia, G.; Sironi, G., Mechanism of Low Temperature Oxidation of Magnetites. *Nature* **1968,** *219* (5158), 1036.

28. Gallaghe, K. J.; Feitknec, W.; Mannweil, U., Mechanism of Oxidation of Magnetite to γ-Fe_2O_3. *Nature* **1968,** *217* (5134), 1118.

29. Roca, A. G.; Marco, J. F.; Morales, M. D.; Serna, C. J., Effect of Nature and Particle Size on Properties of Uniform Magnetite and Maghemite Nanoparticles. *J. Phys. Chem. C* **2007,** *111* (50), 18577.

30. Daou, T. J.; Pourroy, G.; Begin-Colin, S.; Greneche, J. M.; Ulhaq-Bouillet, C.; Legare, P.; Bernhardt, P.; Leuvrey, C.; Rogez, G., Hydrothermal Synthesis of Monodisperse Magnetite Nanoparticles. *Chem. Mater.* **2006,** *18* (18), 4399.

31. Daou, T. J.; Greneche, J. M.; Pourroy, G.; Buathong, S.; Derory, A.; Ulhaq-Bouillet, C.; Donnio, B.; Guillon, D.; Begin-Colin, S., Coupling Agent Effect on Magnetic Properties of Functionalized Magnetite-Based Nanoparticles. *Chem. Mater.* **2008,** *20* (18), 5869.

32. Dehsari, H. S.; Ksenofontov, V.; Moller, A.; Jakob, G.; Asadi, K., Determining Magnetite/Maghemite Composition and Core-Shell Nanostructure from Magnetization Curve for Iron Oxide Nanoparticles. *J. Phys. Chem. C* **2018,** *122* (49), 28292.

33. Frison, R.; Cernuto, G.; Cervellino, A.; Zaharko, O.; Colonna, G. M.; Guagliardi, A.; Masciocchi, N., Magnetite–Maghemite Nanoparticles in the 5–15 nm Range: Correlating the Core–Shell Composition and the Surface Structure to the Magnetic Properties. A Total Scattering Study. *Chem. Mater.* **2013,** *25* (23), 4820.

34. da Costa, G. M.; Blanco-Andujar, C.; De Grave, E.; Pankhurst, Q. A., Magnetic Nanoparticles for in Vivo Use: A Critical Assessment of Their Composition. *J. Phys. Chem. B* **2014,** *118* (40), 11738.

35. Gorski, C. A.; Scherer, M. M., Determination of Nanoparticulate Magnetite Stoichiometry by Mossbauer Spectroscopy, Acidic Dissolution, and Powder X-Ray Diffraction: A Critical Review. *Am. Mineral.* **2010,** *95* (7), 1017.

36. Hwang, Y.; Angappane, S.; Park, J.; An, K.; Hyeon, T.; Park, J. G., Exchange Bias Behavior of Monodisperse Fe_3O_4/ɣ-Fe_2O_3 Core/Shell Nanoparticles. *Curr. Appl. Phys.* **2012,** *12* (3), 808.

37. Martinez-Boubeta, C.; Simeonidis, K.; Angelakeris, M.; Pazos-Perez, N.; Giersig, M.; Delimitis, A.; Nalbandian, L.; Alexandrakis, V.; Niarchos, D., Critical Radius for Exchange Bias in Naturally Oxidized Fe Nanoparticles. *Phys. Rev. B* **2006,** *74* (5), 054430.

38. Salazar, J. S.; Perez, L.; de Abril, O.; Lai, T. P.; Ihiawakrim, D.; Vazquez, M.; Greneche, J. M.; Begin-Colin, S.; Pourroy, G., Magnetic Iron Oxide Nanoparticles in 10–40 nm Range: Composition in Terms of Magnetite/Maghemite Ratio and Effect on the Magnetic Properties. *Chem. Mater.* **2011,** *23* (6), 1379.

39. Daniel, P.; Shylin, S. I.; Lu, H.; Tahir, M. N.; Panthofer, M.; Weidner, T.; Moller, A.; Ksenofontova, V.; Tremel, W., The Surface Chemistry of Iron Oxide Nanocrystals: Surface Reduction of γ-Fe_2O_3 to Fe_3O_4 by Redox-Active Catechol Surface Ligands. *J. Mater. Chem. C* **2018,** *6* (2), 326.

40. Martinez-Mera, I.; Gutierrez-Wing, C.; Arganis-Juarez, C.; Vilchis-Nestor, A. R., Reduction of Maghemite to Magnetite Over 304SS, in the Presence of Silver Nanoparticles. *Surf. Coat. Tech.* **2017,** *324,* 338.

41. Azadmanjiri, J.; Simon, G. P.; Suzuki, K.; Selomulya, C.; Cashion, J. D., Phase Reduction of Coated Maghemite (γ-Fe_2O_3) Nanoparticles Under Microwave-Induced Plasma Heating for Rapid Heat Treatment. *J. Mater. Chem.* **2012,** *22* (2), 617.

42. Carroll, G. M.; Schimpf, A. M.; Tsui, E. Y.; Gamelin, D. R., Redox Potentials of Colloidal *n*-Type ZnO Nanocrystals: Effects of Confinement, Electron Density, and Fermi-Level Pinning by Aldehyde Hydrogenation. *J. Am. Chem. Soc.* **2015,** *137* (34), 11163.

43. Liu, W. K.; Whitaker, K. M.; Kittilstved, K. R.; Gamelin, D. R., Stable Photogenerated Carriers in Magnetic Semiconductor Nanocrystals. *J. Am. Chem. Soc.* **2006,** *128* (12), 3910.

44. Schimpf, A. M.; Gunthardt, C. E.; Rinehart, J. D.; Mayer, J. M.; Gamelin, D. R., Controlling Carrier Densities in Photochemically Reduced Colloidal ZnO Nanocrystals: Size Dependence and Role of the Hole Quencher. *J. Am. Chem. Soc* **2013,** *135* (44), 16569.

45. Schrauben, J. N.; Hayoun, R.; Valdez, C. N.; Braten, M.; Fridley, L.; Mayer, J. M., Titanium and Zinc Oxide Nanoparticles Are Proton-Coupled Electron Transfer Agents. *Science* **2012,** *336* (6086), 1298.

46. Mohamed, H. H.; Mendive, C. B.; Dillert, R.; Bahnemann, D. W., Kinetic and Mechanistic Investigations of Multielectron Transfer Reactions Induced by Stored Electrons in TiO_2 Nanoparticles: A Stopped Flow Study. *J. Phys. Chem. A* **2011,** *115* (11), 2139.

47. Zhou, D. M.; Kittilstved, K. R., Electron Trapping on Fe^{3+} Sites in Photodoped ZnO Colloidal Nanocrystals. *Chem. Commun.* **2016,** *52* (58), 9101.

48. Brozek, C. K.; Zhou, D. M.; Liu, H. B.; Li, X. S.; Kittilstved, K. R.; Gamelin, D. R., Soluble Supercapacitors: Large and Reversible Charge Storage in Colloidal Iron-Doped ZnO Nanocrystals. *Nano Lett.* **2018,** *18* (5), 3297.

49. Minella, M.; Marchetti, G.; De Laurentiis, E.; Malandrino, M.; Maurino, V.; Minero, C.; Vione, D.; Hanna, K., Photo-Fenton Oxidation of Phenol With Magnetite as Iron Source. *Appl. Catal. B-Environ.* **2014,** *154*, 102.

50. Avetta, P.; Pensato, A.; Minella, M.; Malandrino, M.; Maurino, V.; Minero, C.; Hanna, K.; Vione, D., Activation of Persulfate by Irradiated Magnetite: Implications for the Degradation of Phenol under Heterogeneous Photo-Fenton-Like Conditions. *Environ. Sci. Technol.* **2015,** *49* (2), 1043.

51. Goncalves, N. P. F.; Minella, M.; Fabbri, D.; Calza, P.; Malitesta, C.; Mazzotta, E.; Prevot, A. B., Humic Acid Coated Magnetic Particles as Highly Efficient Heterogeneous Photo-Fenton Materials for Wastewater Treatments. *Chem. Eng. J.* **2020,** *390*, 124619.

52. Wu, J. F.; Bai, J.; Wang, Z. D.; Liu, Z. W.; Mao, Y. L.; Liu, B.; Zhu, X. F., UV-Assisted Nitrogen-Doped Reduced Graphene Oxide/Fe_3O_4 Composite Activated Peroxodisulfate Degradation of Norfloxacin. *Environ. Technol.* **2020**.

53. Goncalves, N. P. F.; Minella, M.; Mailhot, G.; Brigante, M.; Prevot, A. B., Photo-Activation of Persulfate and Hydrogen Peroxide by Humic Acid Coated Magnetic Particles for Bisphenol A Degradation. *Catal. Today* **2021,** *361*, 43.

54. Hyeon, T.; Lee, S. S.; Park, J.; Chung, Y.; Bin Na, H., Synthesis of Highly Crystalline and Monodisperse Maghemite Nanocrystallites Without a Size-Selection Process. *J. Am. Chem. Soc.* **2001,** *123* (51), 12798.

55. Strens, R. G. J.; Wood, B. J., Diffuse Reflectance Spectra and Optical-Properties of Some Iron and Titanium-Oxides and Oxyhydroxides. *Mineral. Mag.* **1979,** *43* (327), 347.

56. Park, S. K.; Ishikawa, T.; Tokura, Y., Charge-Gap Formation Upon the Verwey Transition in Fe_3O_4. *Phys. Rev. B* **1998,** *58* (7), 3717.

57. Fontijn, W. F. J.; van der Zaag, P. J.; Feiner, L. F.; Metselaar, R.; Devillers, M. A. C., A Consistent Interpretation of the Magneto-Optical Spectra of Spinel Type Ferrites (Invited). *J. Appl. Phys.* **1999,** *85* (8), 5100.

58. Solano, E.; Frontera, C.; Puig, T.; Obradors, X.; Ricart, S.; Ros, J., Neutron and X-Ray Diffraction Study of Ferrite Nanocrystals Obtained by Microwave-Assisted Growth. A Structural Comparison With the Thermal Synthetic Route. *J. Appl. Crystallogr.* **2014,** *47*, 414.

59. Fleet, M., The Structure of Magnetite. *Acta Crystallogr. B* **1981,** *37* (4), 917.

60. Dar, M. I.; Shivashankar, S. A., Single crystalline magnetite, maghemite, and hematite nanoparticles with rich coercivity. *RSC Adv.* **2014,** *4* (8), 4105.

61. Schimpf, A. M.; Ochsenbein, S. T.; Buonsanti, R.; Milliron, D. J.; Gamelin, D. R., Comparison of Extra Electrons in Colloidal N-Type Al^{3+}-Doped and Photochemically Reduced ZnO Nanocrystals. *Chem. Commun.* **2012,** *48* (75), 9352.

62. Turo, M. J.; Chen, L. F.; Moore, C. E.; Schimpf, A. M., Co^{2+}-Linked $[NaP_5W_{30}O_{110}]^{14-}$: A Redox-Active Metal Oxide Framework with High Electron Density. *J. Am. Chem. Soc.* **2019,** *141* (11), 4553.

63. Rosencwaig, A., Double Exchange and Metal–Nonmetal Transition in Magnetite. *Phys. Rev.* **1969,** *181* (2), 946.

64. McQueeney, R. J.; Yethiraj, M.; Chang, S.; Montfrooij, W.; Perring, T. G.; Honig, J. M.; Metcalf, P., Zener Double Exchange From Local Valence Fluctuations in Magnetite. *Phys. Rev. Lett.* **2007,** *99* (24), 246401.

65. Rebodos, R. L.; Vikesland, P. J., Effects of Oxidation on the Magnetization of Nanoparticulate Magnetite. *Langmuir* **2010,** *26* (22), 16745.

66. Coey, J. M. D., *Magnetism and Magnetic Materials*. Cambridge University Press: Cambridge, 2010; p xii.

67. Kucheryavy, P.; He, J. B.; John, V. T.; Maharjan, P.; Spinu, L.; Goloverda, G. Z.; Kolesnichenko, V. L., Superparamagnetic Iron Oxide Nanoparticles with Variable Size and an Iron Oxidation State as Prospective Imaging Agents. *Langmuir* **2013,** *29* (2), 710.

68. Verwey, E. J. W., Electronic Conduction of Magnetite (Fe_3O_4) and Its Transition Point at Low Temperatures. *Nature* **1939,** *144*, 327.

69. Walz, F., The Verwey Transition—a Topical Review. *J. Phys.-Condens. Mat.* **2002,** *14* (12), R285.

70. Bohra, M.; Agarwal, N.; Singh, V., A Short Review on Verwey Transition in Nanostructured Fe_3O_4 Materials. *J. Nanomater.* **2019,** *2019*, 8457383.

71. Lee, J.; Kwon, S. G.; Park, J. G.; Hyeon, T., Size Dependence of Metal–Insulator Transition in Stoichiometric Fe_3O_4 Nanocrystals. *Nano Lett.* **2015,** *15* (7), 4337.

72. Seehra, M. S.; Srinivasan, G., Magnetic Studies of Nonstoichiometric Fe_zO and Evidence for Magnetic Defect Clusters. *J. Phys. C Solid State* **1984,** *17* (5), 883.

73. Mccammon, C. A., Magnetic-Properties of Fe_xO ($x>0.95$) - Variation of Neel Temperature. *J. Magn. Magn. Mater.* **1992,** *104*, 1937.

74. Estrader, M.; López-Ortega, A.; Golosovsky, I. V.; Estradé, S.; Roca, A. G.; Salazar-Alvarez, G.; López-Conesa, L.; Tobia, D.; Winkler, E.; Ardisson, J. D.; Macedo, W. A. A.; Morphis, A.; Vasilakaki, M.; Trohidou, K. N.; Gukasov, A.; Mirebeau, I.; Makarova, O. L.; Zysler, R. D.; Peiró, F.; Baró, M. D.; Bergström, L.; Nogués, J., Origin of the Large Dispersion of Magnetic Properties in Nanostructured Oxides: Fe_xO/Fe_3O_4 Nanoparticles as a Case Study. *Nanoscale* **2015,** *7* (7), 3002.

75. Milone, C.; Tropeano, M. L.; Gulino, G.; Neri, G.; Ingoglia, R.; Galvagno, S., Selective Liquid Phase Hydrogenation of Citral on Au/Fe_2O_3 Catalysts. *Chem. Commun.* **2002,** (8), 868.

76. Milone, C.; Crisafulli, C.; Ingoglia, R.; Schipilliti, L.; Galvagno, S., A Comparative Study on the Selective Hydrogenation of α, β Unsaturated Aldehyde and Ketone to Unsaturated Alcohols on Au Supported Catalysts. *Catal. Today* **2007,** *122* (3-4), 341.

77. Haffad, D.; Kameswari, U.; Bettahar, M. M.; Chambellan, A.; Lavalley, J. C., Reduction of Benzaldehyde on Metal Oxides. *J. Catal.* **1997,** *172* (1), 85.

78. Gu, L.; Fang, R. H.; Sailor, M. J.; Park, J. H., In Vivo Clearance and Toxicity of Monodisperse Iron Oxide Nanocrystals. *ACS Nano* **2012,** *6* (6), 4947.

Chapter 3: UV Irradiation of Colloidal WSe_2 Nanocrystals with Lithium Triethylborohydride

3.1 Abstract

The UV irradiation of colloidal 2H-WSe_2 nanocrystals in the presence of Li[Et_3BH] is reported. This treatment leads to a bleach of the direct transition and an increase/blue-shift in the C-exciton absorption centered at ~450 nm (2.8 eV). Lattice-expansion upon UV irradiation with Li[Et_3BH] is observed by pXRD but no sign of phase-conversion is observed by either pXRD or Raman spectroscopy. The effect of irradiation-time and the recovery by MeOH addition are detailed. The possible factors causing the lattice-expansion and absorption changes are discussed.

3.2 Introduction

Group-VI transition metal dichalcogenides (Group VI TMDs; MoS_2, $MoSe_2$, $MoTe_2$, WS_2, WSe_2, and WTe_2) have gained great attention as graphene analogues that have extraordinary electronic, optical, catalytic, and mechanical properties.[1-3] For example, semiconducting 2H-MoS_2 exhibits emerging photoluminescence in the monolayer[4] and size-dependent bandgaps[4-7] with high on/off ratios reaching ~10^8, making it a promising channel material for nanoelectronics.[8] WSe_2 has an indirect bandgap of ~1.4 eV in the bulk[9-10] and is a promising material for field-effect transistors due to its ambipolar dopability.[11-12] Bulk and monolayer WSe_2 have been *p*-doped by Na- and Ta-impurities[11-14] and *n*-doped by Re-, In-, and Cu-impurities.[12, 15-17] The efficiency of *n*-type doping, however, is much less than that of *p*-type doping. For example, degenerate *p*-doping of WSe_2 by substitutional impurities is reported to have a hole density higher than 10^{19} cm^{-3}, while the maximum electron density obtained *via* *n*-type substitutional doping of WSe_2 is limited to ~10^{17} cm^{-3}.[12] Recently, few-layer WSe_2 has been *n*-type doped by K-induced surface charge transfer doping and exhibited 2.5×10^{12} cm^{-2} electron sheet density.[18] These carrier densities, however are measured in devices, but the separation of intrinsic materials properties and extrinsic device properties is often challenging due to the charge-trapping effect at the interface between the materials and substrate, which inhibits the careful characterization of intrinsic electronic properties of WSe_2 upon electron-injection.[19] Photochemical reduction, one of the doping strategies for colloidal nanocrystal systems, is known to provide facile modulation of carrier concentration in post-synthetic and nondestructive manner.[20-25] The photodoping of colloidal nanocrystals in solution is advantageous for studying the intrinsic properties of electronically doped semiconducting materials, as it removes the influence of extrinsic factors such as substrate interfaces or device contacts. Here, we synthesize colloidal 2H-WSe_2 nanocrystals and apply UV irradiation in the presence $Li[Et_3BH]$ to adopt the advantages of photochemical doping. Although there is not yet clear evidence of delocalized *n*-type doping in these materials, this phototreatment leads to Li-intercalation which may be accompanied by localized nanocrystal reduction.

TMDs are in the form of MX_2 (M = transition metal and X = chalcogenide), where M-planes are sandwiched between two X-planes to form a monolayer. Monolayers are held together by vdW force to form multilayered materials. The interlayer distance of TMDs is ~ 3–3.5 Å.[26] Due to the gap between each layers, TMDs can serve as an intercalation host for atoms, ions or small molecules.[27] Particularly, Li-ion intercalation has gained significant attention due to its ability to alter the optical, electrical, and thermal properties.[28-33] When Li is intercalated into TMDs, lattice expansion occurs along the *c*-axis, corresponding to an increase in interlayer spacing.[34-35] Upon UV irradiation in the presence of $Li[Et_3BH]$, we observe evidence of Li intercalation in colloidal

WSe_2. The newly reported spectral signs upon the Li-intercalation by the phototreatment may be useful to elucidate Li diffusion mechanism in WSe_2 layered structures.

3.3 Results and discussion

Colloidal WSe_2 nanocrystals were synthesized by a previously reported synthesis.[36] **Figure 3.1a** (dotted black trace) shows the absorption spectrum of a solution of as-synthesized WSe_2 nanocrystals. The absorption at ~1.7 eV is assigned to the direct-gap transition at the κ-point of the semiconducting 2H phase. As-synthesized WSe_2 nanocrystals were revealed by TEM to be ~100 nm in lateral size (**Figure 3.1b**). Following the previously reported photochemical doping methods for metal chalcogenide nanocrystals,[37] anaerobic solutions of WSe_2 nanocrystals ($\sim 1.3 \times 10^{-4}$ M) in toluene/THF (1/1) containing 53 Li[Et_3BH]/W were irradiated using a 365-nm LED (0.5 W/cm^2). **Figure 3.1a** shows the absorption spectra after 0.5, 1, 2 and 16 h UV irradiation. Irradiation times shorter than 0.5 h did not exhibit noticeable spectral changes. As the UV exposure-time increases, the band-edge absorption at 1.7 eV[38] bleaches with increased UV irradiation time. At the same time, the C-exciton absorption[39-40] centered at ~2.7 eV increases and blue-shifts. TEM imaging after irradiation with Li[Et_3BH] shows no degradation of the WSe_2 nanocrystals (**Figure 3.1c**). **Figure 3.1d** plots the absorption changes over time. Specifically, the absorbance of the exciton increases from 0.25 to 0.30 and the energy at the C-exciton increases by 0.04 eV after 16 h UV irradiation. Adding the same amount of Li[Et_3BH] (53 equiv per W) without UV irradiation shows very little change in the absorption (**Figure B.1**), suggesting the changes are indeed induced or facilitated by UV irradiation. Similarly, irradiating WSe_2 without Li[Et_3BH] did not show any spectral changes.

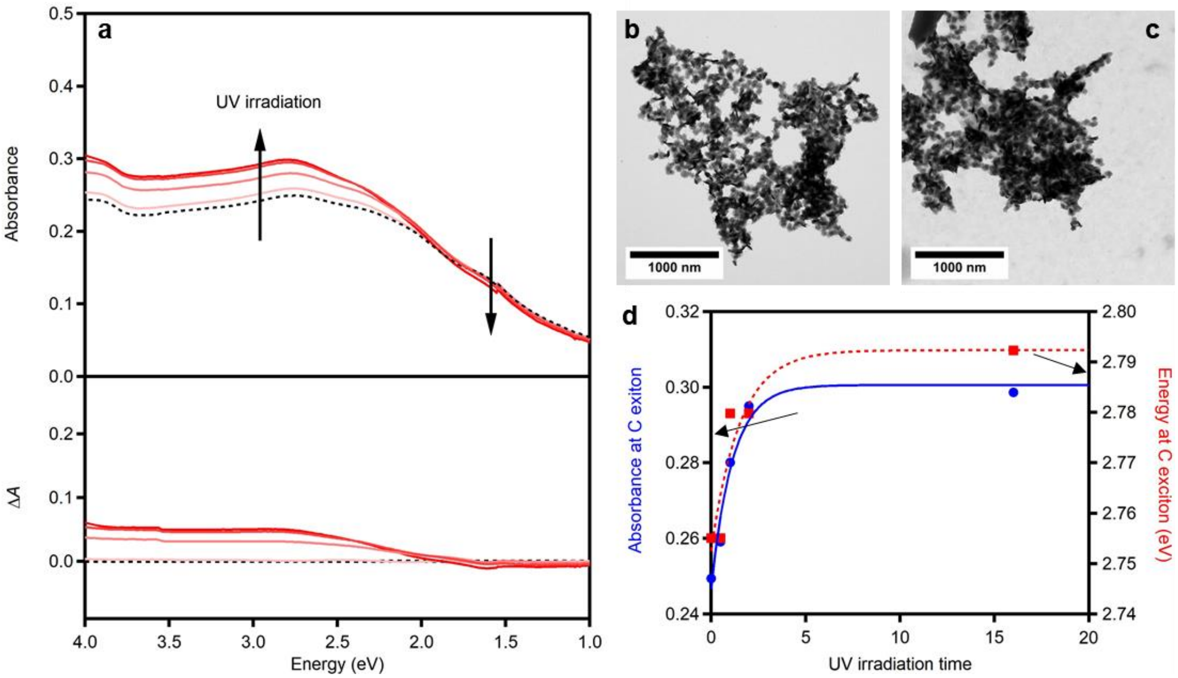

Figure 3.1. UV irradiation of WSe_2 nanocrystals with Li[Et_3BH]. **(a)** Absorption spectra of an anaerobic solution of WSe_2 nanocrystals ([W] = 0.13 mM in toluene/THF, 1/1 by volume) with Li[Et_3BH] (53 equiv per W) before (dotted black trace) and after varying times of UV irradiation (arrows show increasing time). TEM images of nanocrystals **(b)** before and **(c)** after phototreatment with Li[Et_3BH]. **(d)** Absorbance (solid blue, the *y*-axis at the left) and energy (dotted red, the *y*-axis at the right) of the C-exciton versus UV irradiation time.

To test the reversibility of the aforementioned changes, the irradiated WSe_2 nanocrystal solution was first exposed to air. **Figure B.2.** shows that air-exposure does not reverse the spectral changes. This contrasts with photochemically reduced colloidal semiconductor nanocrystals,[20, 22, 37] suggesting that the spectral changes are likely not due to delocalized reduction of WSe_2. Addition of MeOH (~2 equiv per W), however, reverses the absorption changes induced by UV irradiation. **Figure 3.2a** shows electronic absorption spectra (top) and differential absorption (bottom) of as-synthesized, irradiated, and recovered WSe_2 nanocrystals. Following the addition of MeOH, the absorption of the C-exciton decreases to 0.27 and the center of the C-exciton decreased to 2.77 eV

(**Table B.1**). The bleach of the direct-gap transition at 1.7 eV is recovered to that of as-synthesized WSe_2 nanocrystals.

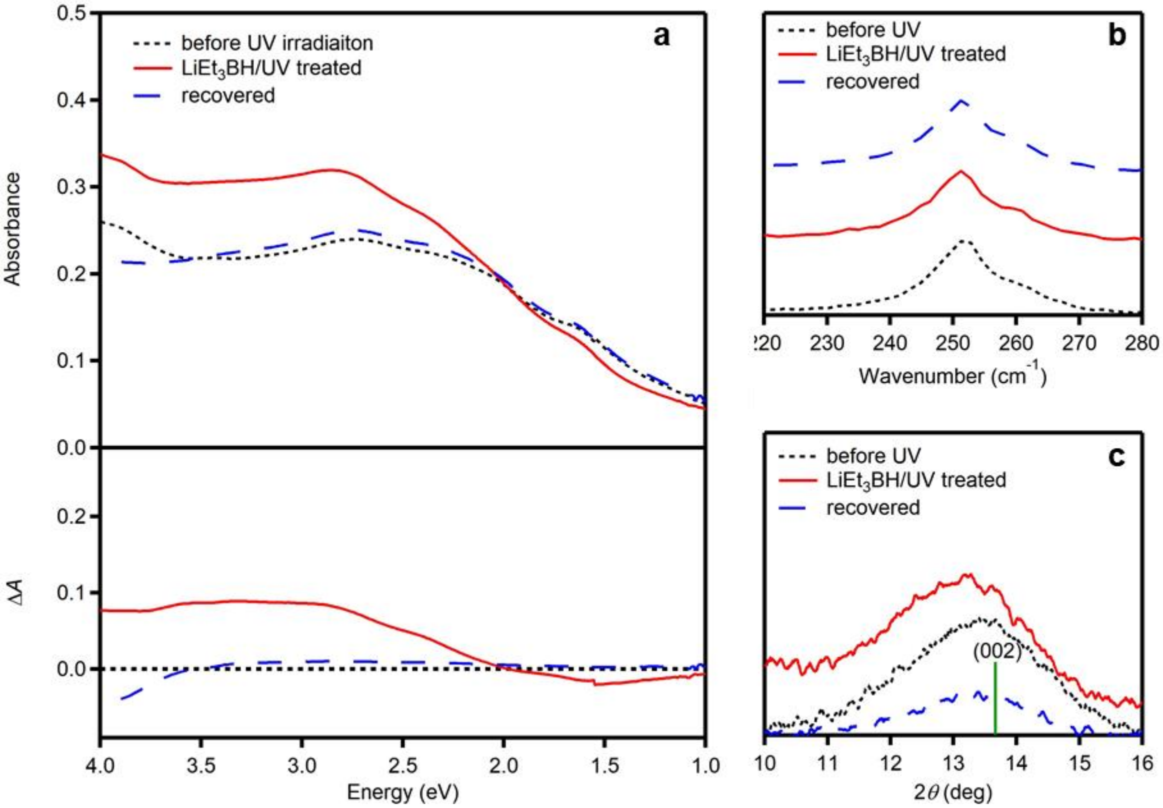

Figure 3.2. (a) Absorption spectra of a colloidal solution of 2H-WSe_2 nanocrystals ([W] = 0.13 mM) before UV irradiation (dotted black), after UV irradiation with Li[Et_3BH] (solid red), and after by addition of MeOH (dashed blue). **(b)** Raman spectra of the same samples dropcast onto a Si substrate and **(c)** pXRD pattern of the same samples precipitated from solution. A tabulated 2H-WSe_2 reference pattern (ICSD #40752)[41] is shown for comparison.

To monitor the structural stability during phototreatment, Raman spectroscopy and pXRD were performed. In the Raman spectra (**Figure 3.2b**) the as-synthesized, phototreated, and recovered WSe_2 spectra maintain an intense peak centered at 250 cm^{-1}, representative of the 2H phase, which contains nearly degenerate A_{1g} and E_{2g} modes.[42-43] The full pXRD patterns (**Figure B.3**) also show that the nanocrystals maintain the 2H phase throughout the Li[Et_3BH]

phototreatment and recovery. There are, however, noticeable changes in the 2θ-values upon UV irradiation, which are reversed upon recovery with MeOH. **Figure 3.2c** shows the (002) reflection of as-synthesized, Li[Et_3BH]/UV-treated and recovered 2H-WSe_2 nanocrystals. After UV irradiation in the presence of Li[Et_3BH], the (002) reflection shifts from 2θ = 13.3° to 12.9°, but shifts back to 13.3° following the addition of MeOH. Since the decrease in 2θ-values indicates an increase in *d*-spacing, we hypothesize that the phototreatment with Li[Et_3BH] leads to intercalation of Li^+, leading to interlayer expansion and forming an air-stable Li_xWSe_2 structure. The difference in *d*-spacing corresponds to 0.2 Å, which is comparable to the difference in the interlayer spacing in Li-intercalated MoS_2[44-45] and WSe_2.[46] Full pXRD patterns (**Figure B.3**) show that the 2θ-values of other reflections (100), (103), (110) also decrease following the phototreatment and are recovered with MeOH (**Table B.2**). These data suggest that Li^+ liberated from Li[Et_3BH] may intercalate into the interlayer spacing of the WSe_2 nanocrystals.

To separate the effects of Li-intercalation and UV irradiation, other treatments were explored. Sonication of WSe_2 nanocrystals with Li metal results in the same absorption increase in the C-exciton at 2.8 eV (**Figure B.4**). Additionally, the band-edge absorption shows a bleach, although with a different shape than that of the bleach observed following the Li[Et_3BH] phototreatment. These results may imply that Li-intercalation is also accompanied by reduction. In contrast, stirring the WSe_2 nanocrystal solution with NaK also caused an increase in the C-exciton absorption, although to a lesser extent than the Li[Et_3BH] phototreatment. Additionally, treatment with NaK did not result in a bleach in the band-edge absorption. (**Figure B.5**). This result suggests that the expansion of the interlayer spacing is responsible for the changes in the C-exciton absorption, as Na^+ is also known to intercalate into WSe_2 layered structures.[35] The changes upon various treatments are summarized in **Table 3.1**.

Table 3.1. Summary of spectroscopic and structural changes with various treatments.

Treatment	**Band-edge bleach**	**Increase and blue-shift of C-exciton**
Li[Et_3BH]/UV	Yes	Yes
Li metal	Yes	Yes
NaK	No	Yes

Figure 3.3 shows photoluminescence spectra (λ_{ex} = 365 nm) of WSe_2 nanocrystals before and after UV irradiation with Li[Et_3BH]. Before irradiation, as-synthesized WSe_2 nanocrystals show a peak centered at 2.5 eV with FWHM ≈ 1 eV. After irradiation, the photoluminescence decreases, broadens and shifts to ~1.9 eV. Similar changes have been observed following Li-intercalation into MoS_2,[47] but further studies are needed to confirm the origin of these changes.

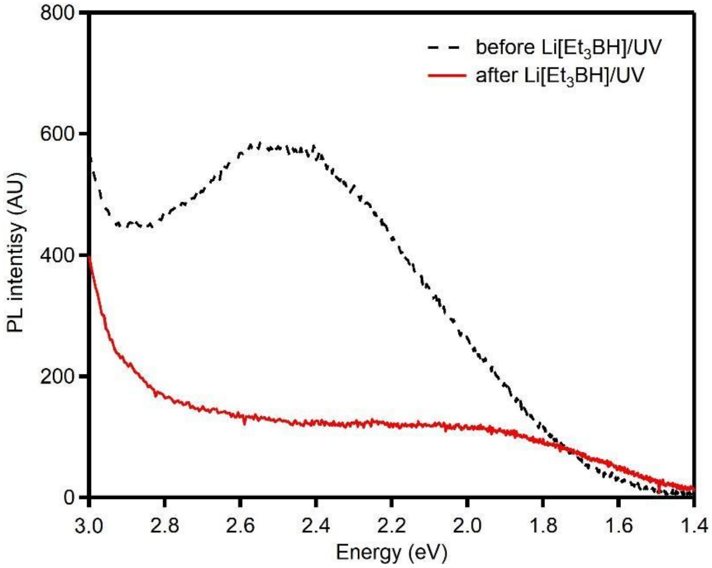

Figure 3.3. PL spectra of WSe_2 nanocrystals ([W] = 0.13 mM) in the presence of Li[Et_3BH] (56 equiv per W) before UV irradiation (dashed black) and after 3h UV irradiation (solid red)

3.4 Summary and conclusions

We show that the UV irradiation using Li[Et_3BH] leads to two noticeable spectroscopic changes in the colloidal WSe_2: (a) a bleach of the direct transition peak and (b) an increase of the C-exciton absorption. The pXRD patterns reveal expansion of the WSe_2 interlayer distance, suggesting intercalation of Li^+ in between the layers (**Figure 3.4**). Similar changes are observed after sonication of as-prepared WSe_2 nanocrystals with Li metal, further corroborating this hypothesis. Interestingly, the addition of MeOH recovers the absorption and structural changes induced by the phototreatment with Li[Et_3BH], but the mechanism of this recovery is still under investigation. This study demonstrates the correlation between Li-intercalation and changes in the C-exciton absorption, which may be useful for the distinction of Li^+ intercalation for the application of WSe_2 such as Li-ion battery electrodes.[48]

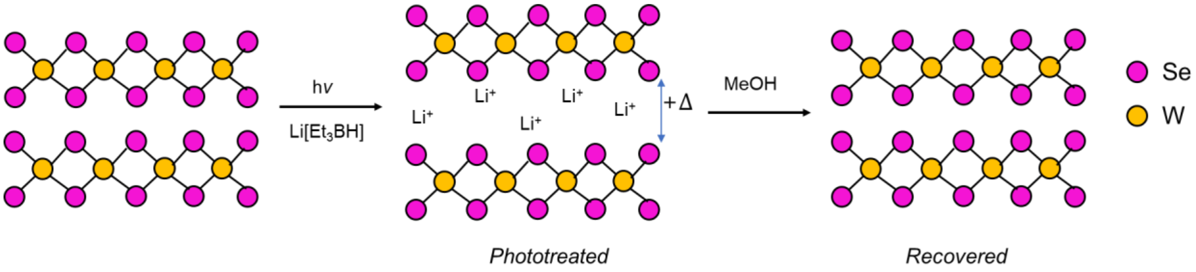

Figure 3.4 Schematic depiction of Li[Et_3BH]/UV treatment of WSe_2 and recovery by MeOH. The interlayer spacing increases upon the phototreatment and recovers when MeOH is added.

3.5 Experimental methods

Chemicals. Chemical manufacturers and purities are given in **Table 3.2.** Tol and THF were obtained from a solvent purification system, transferred to a nitrogen-filled glovebox and stored over molecular sieves (3 Å) for 24 h prior to use.

Table 3.2. Chemicals

Chemical	Purity	Manufacturer
Chemicals used in WSe_2 nanocrystal synthesis		
Tungsten hexacarbonyl ($W(CO)_6$)	99%	Acros Organics
Diphenyl diselenide (Ph_2Se_2)	>96%	TCI
Oleic acid (OA)	>90%	Sigma Aldrich
Trioctylphosphine oxide (TOPO)	>90%	Strem Chemicals
Chemicals used for post-synthetic redox experiments		
Lithium triethylborohydride ($Li[Et_3BH]$, 1 M in THF)	1.00 M	Alfa Aesar
Other chemicals		
Nitric acid (HNO_3, 69%), TraceMetal grade	Fisher Chemical	
Hydrogen peroxide (H_2O_2, 31%) for ultratrace analysis	Sigma Aldrich	

Nanocrystal Synthesis. Colloidal WSe_2 nanocrystals were prepared adapting a previously published synthesis.[36] In a 100-ml round bottom 3-neck flask, 0.8 ml OA (2.5 mmol) and 22.6 g TOPO (57 mmol) loaded with a stir bar. At the same time, a stock solution of Ph_2Se_2 was prepared by mixing 256 mg Ph_2Se_2 (0.8 mmol) and 4 ml (12.7 mmol) OA in a 50-ml round bottom 2-neck flask. Both were degassed under vacuum at 100 °C for 1 h, followed by 4 quick cycles of refilling the flask with nitrogen and degassing. Then the flask containing OA and TOPO was put under vacuum while the flask containing Ph_2Se_2 was filled with N_2 gas. The evacuated TOPO/OA mixture was brought into a nitrogen-filled glovebox and 20 mg $W(CO)_6$ (0.057 mmol) was added. The mixture was put on the Schlenk line and heated to 330 °C under nitrogen and 1 ml Ph_2Se_2 stock solution was rapidly injected into the flask. The reaction was held at 330 °C for 24 h, after which the heat was removed, and the solution cooled to room-temperature. The resulting nanocrystals were washed by the addition of ~5 ml MeOH directly to the solution, after which the precipitated nanocrystals were collected *via* centrifugation for 5 min at 3400 rpm. The resulting pellet was redispersed in 10 ml 2/1 tol/MeOH and centrifuged for 5 min at 3400 rpm. This process was repeated until the nanocrystals had been centrifuged a total of three times. The final products were loaded in 20-ml vial and vacuum-dried under the Schlenk line, brought into the nitrogen-filled glovebox and dispersed in 10 ml toluene to form the anaerobic stock solution. To the nanocrystal suspension, 20 μl OA was added and mixed vigorously to improve the solubility of the dried pellets. The W concentration of the anaerobic nanocrystal stock solutions was ~3.8 mM.

UV irradiation for optical measurements. In a typical experiment, 50 μl anaerobic stock solution, 700 μl toluene and 740 μl THF were loaded into a 4-mm screw-cap cuvette (final [W] ~ 1.3×10^{-4} M). To this solution, 10 μl Li[Et_3BH] (1 M in THF, 53 equiv per W) was added as a sacrificial reductant. (tol:THF = 1:1) The absorption spectrum of the as-prepared solution was collected using a Cary 5000 spectrometer. The solution was irradiated with a 365-nm LED (0.5 W/cm^2) and the absorption spectrum was monitored periodically for a total of 16 h. Addition of 10 μl MeOH (2.5×10^{-4} mol, 1900 equiv per W and 36 equiv per Li[Et_3BH]) to the nanocrystals resulted the recovery in the UV/vis/NIR spectrum.

Powder X-ray diffraction. For measurements on as-synthesized samples, nanocrystals were precipitated by the addition of 0.5 ml EtOH to 0.5 ml anaerobic stock solution and collected via centrifugation at 15000 rpm for 5 min. The resulting pellets were dried under vacuum (2 h) and stored under nitrogen for 1 h prior to the measurement. For measurements on Li[Et_3BH] phototreated samples, as-treated samples (1.5 ml, ~1 mM) were brought into a nitrogen-filled glovebox and precipitated in air-tight centrifuge tubes. Precipitates were collected *via* centrifugation at 15000 rpm for 5 min and resuspended in toluene (0.5 ml). Precipitation was repeated a total of 3 times. After the third centrifugation, the resulting pellets were dried under vacuum (2 h) and stored under nitrogen for 1 h prior to the measurement. The dried samples were transferred to a loop with silicon oil. XRD patterns were collected at 300 K using a D8 Smart diffractometer with a Pt 135 detector equipped with a Rigaku MicroMAx-007HF High-intensity Microfocus rotating anode with Cu Kα radiation ($\lambda = 1.54184$ Å) at 40kV, 30 mA and Varimax-HF double bounce optics. Diffraction images were merged, and background calibrated in Diffrac.Eva V.3.2.0. (Bruker) software. To obtain the reflection locations, powder patterns were fit in the range of $2\theta = 7$–75° with a cubic baseline and Gaussian peaks. Fitting was performed using the Wavemetrics Multi-Peak Fitting Package in Igor.

Raman spectroscopy. As-synthesized, Li[Et_3BH] treated, and recovered WSe_2 nanocrystals were dried as the same manner as for XRD measurement. The dried powders were then loaded onto silicon substrate. Raman spectra were collected using a Renishaw inVia confocal Raman microscope equipped with 532 nm laser excitation (10 mW) and a 50× objective lens.

Elemental analysis. 50 ml anaerobic stock solution was dried under vacuum and digested in 2 ml HNO_3/H_2O_2 (1/1) for 1 day. 100 ml of the digested solution was diluted in 9.9 ml ultrapure H_2O with 5% HNO_3. 1 ml diluted solution was further diluted in 9 ml ultrapure H_2O with 5% HNO_3. Inductively coupled plasma–mass spectrometry (ICP–MS) was collected on a Thermo iCAP RQ ICP–MS.

Transmission electron microscopy. 0.1 ml of the anaerobic stock solution was diluted with ~1 ml toluene. ~20 μl diluted solution was drop-cast onto a 100-mesh copper TEM grid coated with formvar and carbon (Electron Microscopy Sciences). For the phototreated sample, ~20 μl of the nanocrystal solution was taken from the cuvette following maximum photoreduction and drop-cast onto the TEM grid. Grids were examined using either a JEOL JEM-1400Plus transmission electron microscope operating at 80 kV equipped with a Gatan OneView 4K digital camera.

Photoluminescence. 50 µl anaerobic stock solution, 700 µl toluene and 740 µl THF were loaded into a 4-mm screw-cap cuvette (final [W] ~ 1.3×10^{-4} M). To this solution, 10 µl Li[Et_3BH] (1 M in THF, 53 equiv per W) was added as a sacrificial reductant. (tol:THF = 1:1) The cuvettes were excited by 365 nm UV light and the photoluminescence was detected with Ocean Optics QEPro with 1s integration time.

3.6 References

1. Choi, W.; Choudhary, N.; Han, G. H.; Park, J.; Akinwande, D.; Lee, Y. H., Recent Development of Two-Dimensional Transition Metal Dichalcogenides and Their Applications. *Mater. Today* **2017,** *20* (3), 116.

2. Chhowalla, M.; Liu, Z. F.; Zhang, H., Two-Dimensional Transition Metal Dichalcogenide (TMD) Nanosheets. *Chem. Soc. Rev.* **2015,** *44* (9), 2584.

3. Chhowalla, M.; Shin, H. S.; Eda, G.; Li, L. J.; Loh, K. P.; Zhang, H., The Chemistry of Two-Dimensional Layered Transition Metal Dichalcogenide Nanosheets. *Nat. Chem.* **2013,** *5* (4), 263.

4. Splendiani, A.; Sun, L.; Zhang, Y. B.; Li, T. S.; Kim, J.; Chim, C. Y.; Galli, G.; Wang, F., Emerging Photoluminescence in Monolayer MoS_2. *Nano Lett.* **2010,** *10* (4), 1271.

5. Kam, K. K.; Parkinson, B. A., Detailed Photocurrent Spectroscopy of the Semiconducting Group-VI Transition-Metal Dichalcogenides. *J. Phys. Chem.* **1982,** *86* (4), 463.

6. Mak, K. F.; Lee, C.; Hone, J.; Shan, J.; Heinz, T. F., Atomically Thin MoS_2: A New Direct-Gap Semiconductor. *Phys. Rev. Lett.* **2010,** *105* (13), 136805.

7. Kuc, A.; Zibouche, N.; Heine, T., Influence of Quantum Confinement on the Electronic Structure of the Transition Metal Sulfide TS_2. *Phys. Rev. B* **2011,** *83* (24).

8. Radisavljevic, B.; Radenovic, A.; Brivio, J.; Giacometti, V.; Kis, A., Single-Layer MoS_2 Transistors. *Nat. Nanotechnol.* **2011,** *6* (3), 147.

9. Yuan, H. T.; Liu, Z. K.; Xu, G.; Zhou, B.; Wu, S. F.; Dumcenco, D.; Yan, K.; Zhang, Y.; Mo, S. K.; Dudin, P.; Kandyba, V.; Yablonskikh, M.; Barinov, A.; Shen, Z. X.; Zhang, S. C.; Huang, Y. S.; Xu, X. D.; Hussain, Z.; Hwang, H. Y.; Cui, Y.; Chen, Y. L., Evolution of the Valley Position in Bulk Transition-Metal Chalcogenides and Their Monolayer Limit. *Nano Lett.* **2016,** *16* (8), 4738.

10. Upadhyayula, L. C.; Loferski, J. J.; Wold, A.; Giriat, W.; Kershaw, R., Semiconducting Properties of Single Crystals of *N* and *P*-Type Tungsten Diselenide (WSe_2). *J. Appl. Phys.* **1968,** *39* (10), 4736.

11. Hicks, W. T., Semiconducting Behavior of Substituted Tungsten Diselenide and Its Analogues. *J. Electrochem. Soc.* **1964,** *111* (9), 1058.

12. Mukherjee, R.; Chuang, H. J.; Koehler, M. R.; Combs, N.; Patchen, A.; Zhou, Z. X.; Mandrus, D., Substitutional Electron and Hole Doping of WSe_2: Synthesis, Electrical

Characterization, and Observation of Band-to-Band Tunneling. *Phys. Rev. Appl.* **2017,** *7* (3), 034011.

13. Fu, Y. J.; Long, M. S.; Gao, A. Y.; Wang, Y.; Pan, C.; Liu, X. W.; Zeng, J. W.; Xu, K.; Zhang, L. L.; Liu, E. F.; Hu, W. D.; Wang, X. M.; Miao, F., Intrinsic *P*-Type W-Based Transition Metal Dichalcogenide by Substitutional Ta-Doping. *App. Phys. Lett.* **2017,** *111* (4).

14. Pandey, S. K.; Alsalman, H.; Azadani, J. G.; Izquierdo, N.; Low, T.; Campbell, S. A., Controlled *P*-Type Substitutional Doping in Large-Area Monolayer WSe_2 Crystals Grown by Chemical Vapor Deposition. *Nanoscale* **2018,** *10* (45), 21374.

15. Deshpande, M. P.; Parmar, M. N.; Pandya, N. N.; Chaki, S.; Bhatt, S. V., Studies on Transport Properties of Copper Doped Tungsten Diselenide Single Crystals. *Physica B* **2012,** *407* (4), 808.

16. Deshpande, M. P.; Patel, J. B.; Pandya, N. N.; Parmar, M. N.; Solanki, G. K., Growth and Transport Pproperty Measurements of Rhenium Doped Tungsten Diselenide Single Crystal. *Mater. Chem. Phys.* **2009,** *117* (2-3), 350.

17. Deshpande, M. P.; Patel, P. D.; Vashi, M. N.; Agarwal, M. K., Effect of Intercalating Indium in WSe_2 Single Crystals. *J. Cryst. Growth* **1999,** *197* (4), 833.

18. Fang, H.; Tosun, M.; Seol, G.; Chang, T. C.; Takei, K.; Guo, J.; Javey, A., Degenerate n-Doping of Few-Layer Transition Metal Dichalcogenides by Potassium. *Nano Lett.* **2013,** *13* (5), 1991.

19. Zhao, Y. D.; Xu, K.; Pan, F.; Zhou, C. J.; Zhou, F. C.; Chai, Y., Doping, Contact and Interface Engineering of Two-Dimensional Layered Transition Metal Dichalcogenides Transistors. *Adv. Fucnt. Mater.* **2017,** *27* (19), 1603484.

20. Carroll, G. M.; Schimpf, A. M.; Tsui, E. Y.; Gamelin, D. R., Redox Potentials of Colloidal *n*-Type ZnO Nanocrystals: Effects of Confinement, Electron Density, and Fermi-Level Pinning by Aldehyde Hydrogenation. *J. Am. Chem. Soc.* **2015,** *137* (34), 11163.

21. Schimpf, A. M.; Lounis, S. D.; Runnerstrom, E. L.; Milliron, D. J.; Gamelin, D. R., Redox Chemistries and Plasmon Energies of Photodoped In_2O_3 and Sn-Doped In_2O_3 (ITO) Nanocrystals. *J. Am. Chem. Soc.* **2015,** *137* (1), 518.

22. Schimpf, A. M.; Gunthardt, C. E.; Rinehart, J. D.; Mayer, J. M.; Gamelin, D. R., Controlling Carrier Densities in Photochemically Reduced Colloidal ZnO Nanocrystals: Size Dependence and Role of the Hole Quencher. *J. Am. Chem. Soc.* **2013,** *135* (44), 16569.

23. Shim, M.; Guyot-Sionnest, P., Organic-Capped ZnO Nanocrystals: Synthesis and *n*-Type Character. *J. Am. Chem. Soc.* **2001,** *123* (47), 11651.

24. Shim, M.; Guyot-Sionnest, P., *N*-type Colloidal Semiconductor Nanocrystals. *Nature* **2000,** *407* (6807), 981.

25. Liu, W. K.; Whitaker, K. M.; Kittilstved, K. R.; Gamelin, D. R., Stable Photogenerated Carriers in Magnetic Semiconductor Nanocrystals. *J. Am. Chem. Soc.* **2006,** *128* (12), 3910.

26. Vaidya, D.; Lodha, S.; Ganguly, S., Electrical-Equivalent van der Waals Gap for Two-Dimensional Bilayers. *Phys. Rev. Appl.* **2018,** *10* (3), 034070.

27. Wang, Z.; Li, R.; Su, C.; Loh, K. P., Intercalated Phases of Transition Metal Dichalcogenides. *Smart Mat.* **2020,** *1* (1), 1013.

28. Eda, G.; Yamaguchi, H.; Voiry, D.; Fujita, T.; Chen, M.; Chhowalla, M., Photoluminescence from Chemically Exfoliated MoS_2. *Nano Lett.* **2011,** *11* (12), 5111.

29. Kappera, R.; Voiry, D.; Yalcin, S. E.; Branch, B.; Gupta, G.; Mohite, A. D.; Chhowalla, M., Phase-Engineered Low-Resistance Contacts for Ultrathin MoS_2 Transistors. *Nat. Mater.* **2014,** *13* (12), 1128.

30. Kim, J. S.; Kim, J.; Zhao, J.; Kim, S.; Lee, J. H.; Jin, Y.; Choi, H.; Moon, B. H.; Bae, J. J.; Lee, Y. H.; Lim, S. C., Electrical Transport Properties of Polymorphic MoS_2. *ACS Nano* **2016,** *10* (8), 7500.

31. Ma, Y.; Liu, B.; Zhang, A.; Chen, L.; Fathi, M.; Shen, C.; Abbas, A. N.; Ge, M.; Mecklenburg, M.; Zhou, C., Reversible Semiconducting-to-Metallic Phase Transition in Chemical Vapor Deposition Grown Monolayer WSe_2 and Applications for Devices. *ACS Nano* **2015,** *9* (7), 7383.

32. Xiong, F.; Wang, H.; Liu, X.; Sun, J.; Brongersma, M.; Pop, E.; Cui, Y., Li Intercalation in MoS_2: In Situ Observation of Its Dynamics and Tuning Optical and Electrical Properties. *Nano Lett.* **2015,** *15* (10), 6777.

33. Zhu, G.; Liu, J.; Zheng, Q.; Zhang, R.; Li, D.; Banerjee, D.; Cahill, D. G., Tuning Thermal Conductivity in Molybdenum Disulfide by Electrochemical Intercalation. *Nat. Commun.* **2016,** *7* (1), 13211.

34. Zhang, Q.; Mei, L.; Cao, X.; Tang, Y.; Zeng, Z., Intercalation and Exfoliation Chemistries of Transition Metal Dichalcogenides. *J. Mater. Chem. A* **2020,** *8* (31), 15417.

35. Wang, Y. C.; Zhang, X.; Xiong, P. X.; Yin, F. X.; Xu, Y. H.; Wan, B.; Wang, Q. Z.; Wang, G. K.; Ji, P. G.; Gou, H. Y., Insight Into the Intercalation Mechanism of WSe_2 Onions Toward Metal Ion Capacitors: Sodium Rivals Lithium. *J. Mater. Chem. A* **2018,** *6* (43), 21605.

36. Geisenhoff, J. Q.; Tamura, A. K.; Schimpf, A. M., Using Ligands to Control Reactivity, Size and Phase in the Colloidal Synthesis of WSe_2 Nanocrystals. *Chem. Commun.* **2019,** *55* (60), 8856.

37. Rinehart, J. D.; Schimpf, A. M.; Weaver, A. L.; Cohn, A. W.; Gamelin, D. R., Photochemical Electronic Doping of Colloidal CdSe Nanocrystals. *J. Am. Chem. Soc.* **2013,** *135* (50), 18782.

38. Zhao, W.; Ghorannevis, Z.; Chu, L.; Toh, M.; Kloc, C.; Tan, P. H.; Eda, G., Evolution of Electronic Structure in Atomically Thin Sheets of WS_2 and WSe_2. *ACS Nano* **2013,** *7* (1), 791.

39. Hong, J. H.; Koshino, M.; Senga, R.; Pichler, T.; Xu, H.; Suenaga, K., Deciphering the Intense Postgap Absorptions of Monolayer Transition Metal Dichalcogenides. *ACS Nano* **2021,** *15* (4), 7783.

40. Kozawa, D.; Kumar, R.; Carvalho, A.; Amara, K. K.; Zhao, W. J.; Wang, S. F.; Toh, M. L.; Ribeiro, R. M.; Neto, A. H. C.; Matsuda, K.; Eda, G., Photocarrier Relaxation Pathway in Two-Dimensional Semiconducting Transition Metal Dichalcogenides. *Nat. Commun.* **2014,** *5*, 4543.

41. Schutte, W. J.; Deboer, J. L.; Jellinek, F., Crystal-Structures of Tungsten Disulfide and Diselenide. *J. Solid State Chem.* **1987,** *70* (2), 207.

42. Sahin, H.; Tongay, S.; Horzum, S.; Fan, W.; Zhou, J.; Li, J.; Wu, J.; Peeters, F. M., Anomalous Raman Spectra and Thickness-Dependent Electronic Properties of WSe_2. *Phys. Rev. B* **2013,** *87* (16), 165409.

43. Zhao, W. J.; Ghorannevis, Z.; Amara, K. K.; Pang, J. R.; Toh, M.; Zhang, X.; Kloc, C.; Tan, P. H.; Eda, G., Lattice dynamics in mono- and few-layer sheets of WS_2 and WSe_2. *Nanoscale* **2013,** *5* (20), 9677.

44. Fan, X. B.; Xu, P. T.; Zhou, D. K.; Sun, Y. F.; Li, Y. G. C.; Nguyen, M. A. T.; Terrones, M.; Mallouk, T. E., Fast and Efficient Preparation of Exfoliated 2H MoS_2 Nanosheets by Sonication-Assisted Lithium Intercalation and Infrared Laser-Induced 1T to 2H Phase Reversion. *Nano Lett.* **2015,** *15* (9), 5956.

45. Gong, S.; Zhao, G. Y.; Lyu, P. B.; Sun, K. N., Insights Into the Intrinsic Capacity of Interlayer-Expanded MoS_2 as a Li-Ion Intercalation Host. *J. Mater. Chem. A* **2019,** *7* (3), 1187.

46. Shin, Y. S.; Lee, K.; Duong, D. L.; Kim, J. S.; Kang, W. T.; Kim, J. E.; Won, U. Y.; Lee, I.; Lee, H.; Heo, J.; Lee, Y. H.; Yu, W. J., Li Intercalation Effects on Interface Resistances of High-Speed and Low-Power WSe_2 Field-Effect Transistors. *Adv. Funct. Mater.* **2020,** *30* (45), 2003688.

47. Byrley, P.; Liu, M.; Yan, R. X., Photochemically Induced Phase Change in Monolayer Molybdenum Disulfide. *Front. Chem.* **2019,** *7*, 442.

48. Van der Ven, A.; Bhattacharya, J.; Belak, A. A., Understanding Li Diffusion in Li-Intercalation Compounds. *Acc. Chem. Res.* **2013,** *46* (5), 1216.

Chapter 4: Air-Stable Reduction of Zn-Bridged Preyssler-Type Polyoxometalate Frameworks

4.1 Abstract

POMs are polyatomic ions comprised of group 5 or group 6 TMs, usually in their highest oxidation state. The structural diversity and reversible redox activity of POMs make them attractive building-blocks for modular or multifunctional extended structures. This chapter focuses on frameworks derived from the Preyssler polyoxotungstate, $[NaP_5W_{30}O_{110}]^{14-}$ ($\{P_5W_{29}\}$), and the modified Preyssler anion, $[NaP_5MoW_{29}O_{110}]^{14-}$ ($\{P_5MoW_{29}\}$), which can be assembled into frameworks with and TM bridging ions. We show that the frameworks can be assembled under UV irradiation to access reduced frameworks without altering the crystal structure, removing the need for lengthy, post-synthetic reduction. Notably, Zn-bridged $\{P_5MoW_{29}\}$ frameworks can maintain their reduced state when stored aerobically foe extended periods of time, making them uniquely stable within this class of materials.

4.2 Introduction

POMs are metal oxide clusters that are composed of a TM, such as W or Mo, usually in their highest oxidation state.[3-6] POMs have received attention as building-blocks for the rational design of higher-order materials due to vast structural diversity and possible coordination with various linkers including metals, networks, and other suprastructures while exhibiting reversible redox activity.[2, 6-13] The high oxidation states of metals in POMs makes them susceptible to reduction in which added electrons populate the metal *d*-orbitals, giving rise to delocalized charge-transfer transitions.[7, 14-15] Incorporating this rich redox activity into POM-based solid-state enables the design of tunable materials with functionalities similar to bulk semiconductors.

The assembly of POMs into frameworks with bridging metal ions, including TMs or lanthanides, can impart additional functionality and extraordinary photophysical, electronic, and magnetic properties.[4, 7-8, 14, 16] Recently our group has shown successful fabrication of all-inorganic frameworks, where POM clusters are solely connected through coordinative O–M−O bonds to form three-dimensional networks.[17-18] We also demonstrated post-synthetic, reversible electron accumulation in Co^{2+}-bridged $[NaP_5W_{30}O_{110}]^{14-}$ frameworks by photochemical doping and oxidation by molecular acceptors.[18] This process is analogous to the photochromic effects observed in thin films of WO_{3-x}.[19-20] The photochemical doping was even assessable by irradiating the frameworks with UV during the crystallization, which is advantageous to shorten the time require to reduce them postsynthetically and achieve more crystalline materials.

Herein, we synthesize a new metal oxide framework based on a modified Preyssler ion, $K_{13.4}Na_{0.6}[NaP_5MoW_{29}O_{110}]\cdot 15H_2O$ (denoted $\{P_5MoW_{29}\}$), bridged with TMs. This study was inspired by an exciting observation that Zn-bridged $\{P_5MoW_{29}\}$ frameworks can be photoreduced with only sunlight. Although this is true for other TM-bridged frameworks, most will easily oxidize when removed from light, and do not maintain a large population of reduced clusters. Zn-bridged frameworks, on the other hand, are stable in air for over five months, allowing easy observation of their reduced state. Using redox titrations, these frameworks were determined to contain ~3 electrons per $\{P_5MoW_{29}\}$ cluster in the photoreduced state.

4.3. Results and discussions

Zn-bridged $\{P_5MoW_{29}\}$ frameworks were synthesized by adding 0.60 mmol $ZnCl_2$ and

0.016 mmol $K_{13.5}Na_{0.5}[NaP_5MoW_{29}O_{110}]\cdot 15H_2O$ ($\{P_5MoW_{29}\}$) in aqueous $LiClO_4$ (2 ml, 1 M, pH 1.0–1.5, adjusted by 4 M HCl), followed by MeOH diffusion to induce crystal-formation. One crystallization setup was kept in the dark during crystallization while the other was irradiated with UV light (λ = 365 nm, 0.04 W/cm^2). Both crystallizations were allowed to grow for two weeks. **Figure 4.1** shows photographs of the resulting framework crystals. Zn-bridged $\{P_5MoW_{29}\}$ frameworks grown in the dark are yellow (**Figure 4.1a**), consistent with the color of$\{P_5MoW_{29}\}$. Those grown under UV, however, are dark blue or nearly black (**Figure 4.1b**), owing to charge-transfer transitions in the reduced cluster. Remarkably, the dark coloring of the UV-grown frameworks is maintained even after being stored aerobically in the dark for 3 weeks (**Figure 4.1c**). In contrast, Zn-bridged $\{P_5W_{30}\}$ frameworks grown under UV are less darkly colored (**Figure 4.1e**), indicating a lower level of reduction, and do not maintain this reduction following the synthesis (**Figure 4.1f**). **Figure 4.2** shows that all frameworks synthesized here crystallize in the *Imma* space group, as has been seen previously. [17-18] The pXRD patterns also reveal no discernible difference when the crystals were stored aerobically for three months (**Figure C.1**).

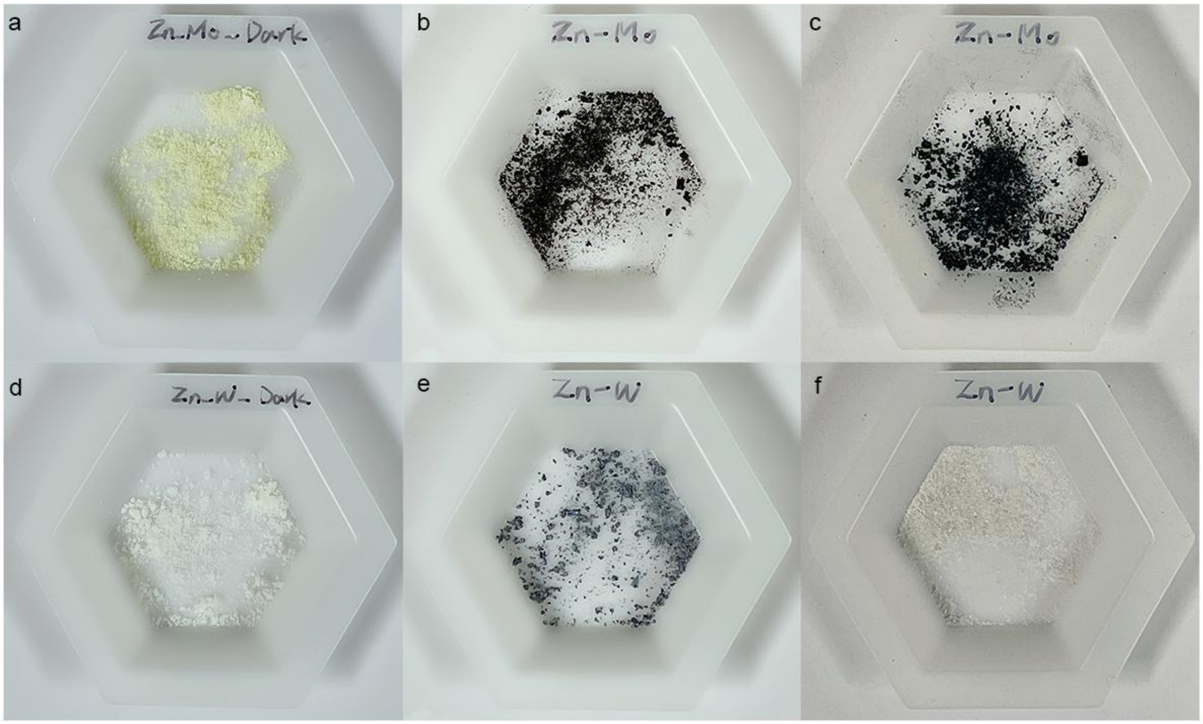

Figure 4.1. Photographs of **(a)** Zn-bridged{P_5MoW_{29}} frameworks grown in the dark, **(b)** Zn-bridged{P_5MoW_{29}} frameworks grown under UV irradiation, **(c)** Zn-bridged{P_5MoW_{29}} frameworks grown under UV irradiation and stored aerobically in the dark for 3 weeks, **(d)** Zn-bridged{P_5W_{30}} frameworks grown in the dark, **(e)** Zn-bridged{P_5W_{30}} frameworks grown under UV irradiation and **(f)** Zn-bridged{P_5W_{30}} frameworks grown under UV irradiation and stored aerobically in the dark for 3 weeks.

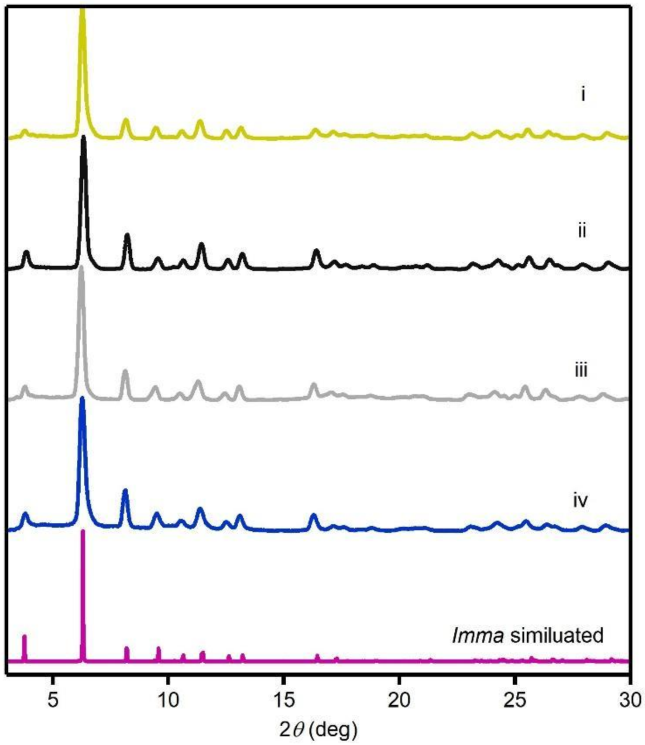

Figure 4.2. PXRD patterns of (i) Zn-bridged {P_5MoW_{29}} frameworks grown in the dark (ii) Zn-bridged {P_5MoW_{29}} frameworks grown in light (iii) Zn-bridged-{P_5W_{30}} frameworks grown in the dark (iv) Zn-bridged-{P_5W_{30}} frameworks grown in light, and simulated *Imma*.

For comparison Mn-, Fe-, Co-, and Ni-bridged {P_5MoW_{29}} frameworks were also grown under UV irradiation and in the dark (**Figure C.2**). Crystals grown under UV irradiation (**Figure C.2, top**) are all darkly colored, regardless of the bridging ion, indicating reduction of the {P_5MoW_{29}} cluster. In contrast, frameworks grown in the dark derive their color from the bridging ion, as has been observed previously.[17] When the reduced frameworks are washed and stored aerobically, the TM-derived colors are recovered (**Figure C.3**), indicating oxidation of the frameworks. These data highlight the unique stability of reduced Zn-bridged {P_5MoW_{29}} frameworks against oxidation by air.

To evaluate the excess electrons present in the reduced frameworks, $Cu[OTf]_2$ was used as a molecular oxidant. **Figure 4.3a** shows the $^2E_g \rightarrow {}^2T_{2g}$ absorption characteristic of octahedral Cu^{2+}. As reduced framework is added, this absorption decreases, indicating a reduction of the Cu^{2+}. Concomitantly, the frameworks lose their dark coloration, indicating oxidation. Incremental addition of reduced frameworks to the $Cu[OTf]_2$ solution yields an equivalence point of 0.31 ± 0.01 $\{P_5MoW_{29}\}$ per Cu^{2+}, or 3.2 ± 0.1 electrons per $\{P_5MoW_{29}\}$ cluster (**Figure 4.3a**). After the Cu^{2+} has been reduced, $Cu[OTf]_2$ is added back in to rule out any adventitious redox reactions (**Figure 4.3b**). The linear increase in Cu^{2+} absorption yields an equivalence point of 3.3 ± 0.1 e^- per cluster, consistent with the addition of reduced framework. Three titrations by the addition of framework into $Cu[OTf]_2$ solution yielded an average of 3.2 ± 0.1 e^- per $\{P_5MoW_{29}\}$, corresponding to an electron density of to $8.5 \pm 0.4 \times 10^{20}$ cm^{-3} (**Table C.1**).

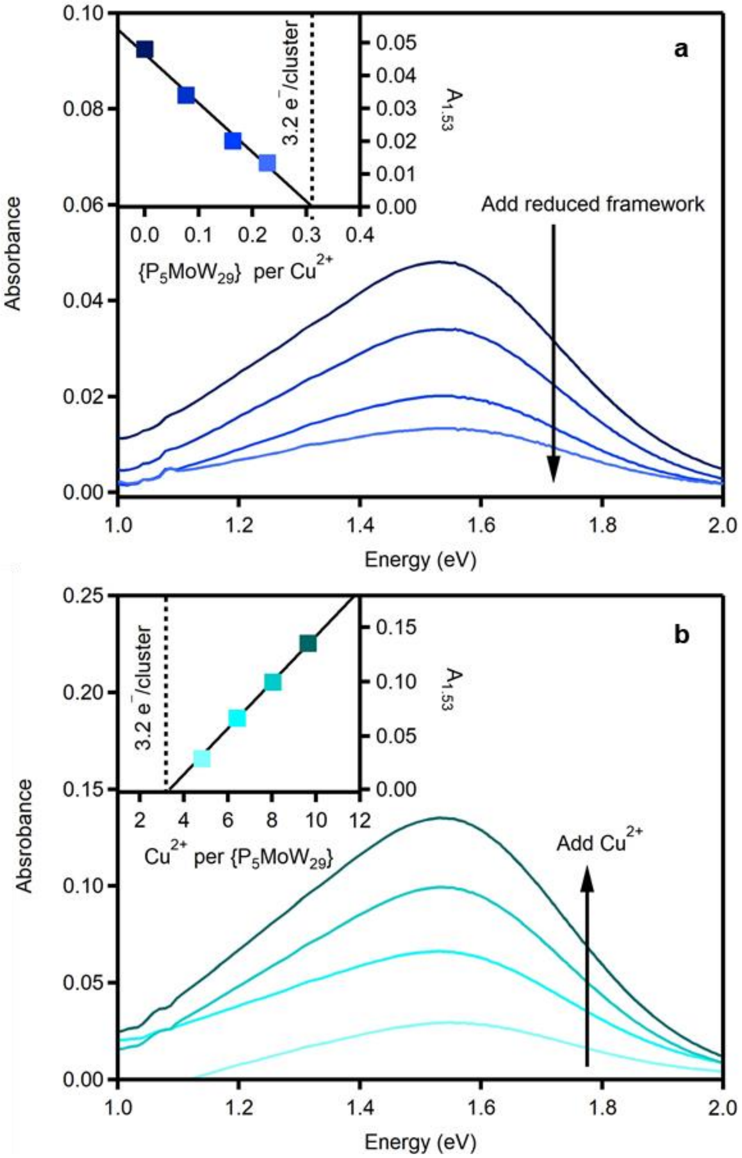

Figure 4.3. Redox titration of Zn-bridged $\{P_5MoW_{29}\}$ frameworks grown under UV irradiation. **(a)** Addition of reduced framework to a solution of $Cu[OTf]_2$ (0.021 M in 7:2:1 toluene:MeCN/MeOH) leads to a linear decrease in Cu^{2+} *d-d* absorption accompanied by a loss of the dark blue color in the framework. The equivalence point yields 3.2 ± 0.1 e^- per cluster. **(b)** Addition of $Cu[OTf]_2$ to the fully oxidized frameworks leads to a linear increase in Cu^{2+} *d-d* absorption, with an equivalence point of 3.2 e^- per cluster.

Mo-substitution into a polyoxotungstate can stabilize the cluster LUMO[21] and facilitate reduction.[21-24] This stabilization effect of the LUMO relative to the E_F should make the *n*-type charge-carriers delocalized more stably, thereby enhanced photoreduction. To detect whether this effect occurs in the framework, XPS was used.

Figure 4.4 shows the W *4f* peaks of Zn-bridged {P_5MoW_{29}} frameworks and Zn-bridged {P_5W_{30}} frameworks grown under UV irradiation and in the dark. Compared to Zn-bridged {P_5W_{30}} frameworks in the dark (**Figure 4.4i**), Zn-bridged {P_5W_{30}} frameworks grown in light (**Figure 4.4ii**) shift to slightly lower binding energy, which suggests the W atoms are slightly reduced when grown under UV. In addition, the W *4f* peaks of Zn-bridged {P_5MoW_{29}} frameworks grown in the dark (**Figure 4.4iii**) also shift to lower binding energy compared to those of Zn-bridged {P_5W_{30}} frameworks grown in the dark (**Figure 4.4i**) There is no noticeable peak shifts between Zn-bridged {P_5MoW_{29}} frameworks grown in light (**Figure 4.4iv**) and (**Figure 4.4iii**) This observation suggests W atoms are slightly reduced by the incorporation of Mo as well as by the photoreduction.

In **Figure 4.5,** the Mo *3d* spectra of Zn-bridged {P_5MoW_{29}} frameworks grown in light exhibited a doublet pair suited at 231.4 and 234.7 eV. The peak suited at 231.4 eV was stemmed from the binding energy of Mo $3d_{5/2}$, and the 234.7 eV peak was derived from the binding energy of Mo $3d_{3/2}$. The Mo $3d_{5/2}$ spectrum of Zn-bridged {P_5MoW_{29}} grown in the dark (**Figure C.4a**) was deconvoluted into two peaks: a low binding energy peak located at 234.7eV was associated with Mo^{5+}, whereas a high binding energy peak lied at 235.4 eV was arose from Mo^{6+}, indicating the mix valance of Mo. On the other hand, Zn-bridged {P_5MoW_{29}} grown in light matches with Mo^{5+} (**Figure C.4b**). A significant shift in the Mo *3d* spectra and a minor shift in W *4f* spectra suggests that the photoreduction mostly occurs in the Mo sites. Incorporating Mo into tungsten oxides is confirmed here as an efficient method to tune the band structure and improve the electronic or photoreduction properties.

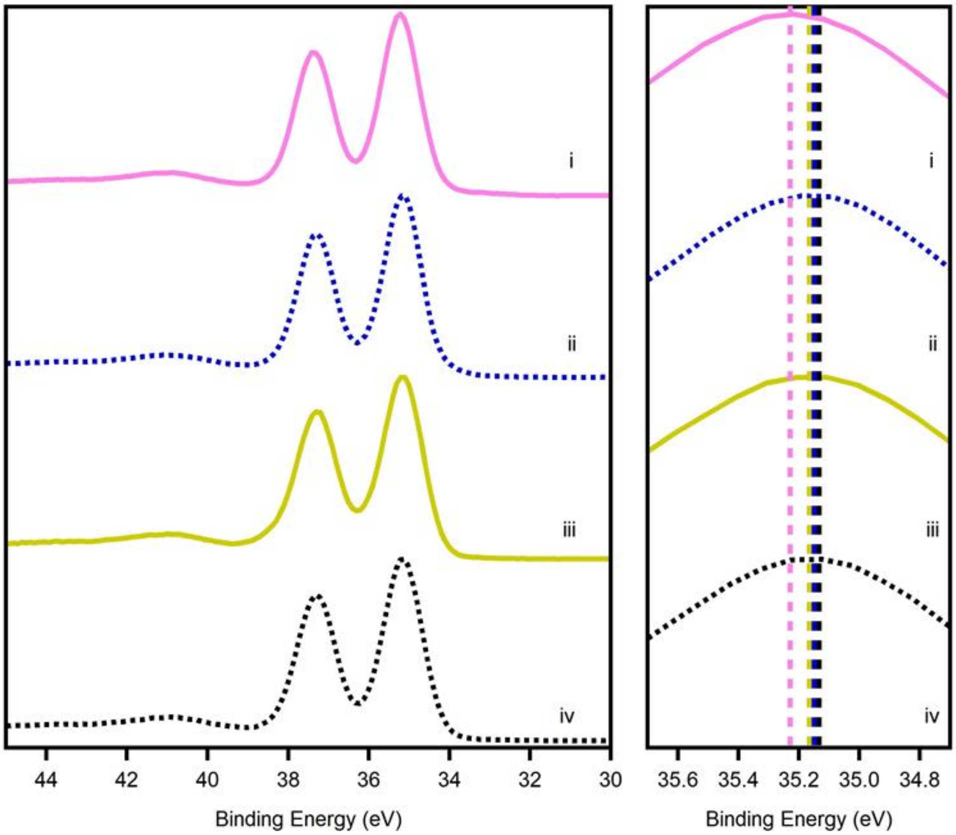

Figure 4.4. W *4f* X-ray photoelectron spectra of (i) Zn-bridged {P_5W_{30}} framework grown in the dark (solid pink) (ii) Zn-bridged {P_5W_{30}} framework grown in light (dashed blue) (iii) Zn-bridged {P_5MoW_{29}} framework grown in the dark (solid yellow) (iv) Zn-bridged {P_5MoW_{29}} grown under UV irradiation (dashed black)

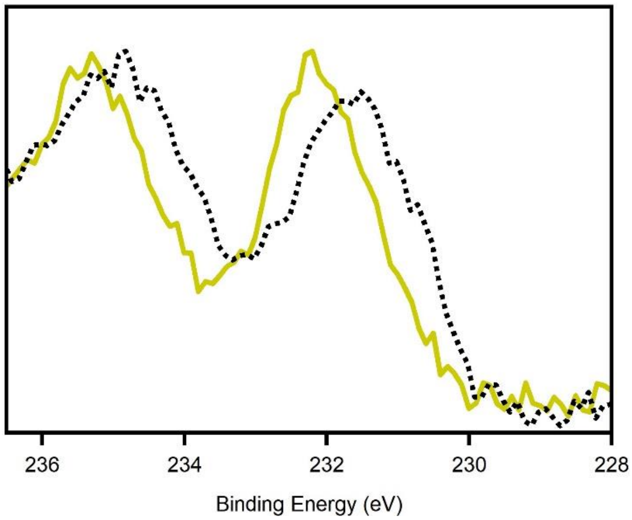

Figure 4.5. Mo *3d* X-ray photoelectron spectra of Zn-bridged {P_5MoW_{29}} grown under UV irradiation (dashed black) and in the dark (solid yellow).

4.4 Summary and conclusions

In summary, we demonstrate the use of {P_5MoW_{29}} frameworks as a platform to achieve exceptional oxidation resistance in photoreduced state with a proper selection of metal linker. Notably, by simply irradiating UV during the crystallization steps, highly crystalline frameworks in their reduced states are obtained. This observation suggests a simpler and time-effective way to obtain POM-based frameworks with high electron density. In addition, while most reduced TM-bridged POM frameworks are easily oxidized in air we show that Zn-bridged {P_5MoW_{29}} framework has exceptional air-resistance in their reduced form at least 4 weeks and longer. The unique and stable electron structure of Zn^{2+} may play a vital role in maintaining the photoreduction status, by stabilizing the LUMO of POMs, especially {P_5MoW_{29}}. These results demonstrate the exciting promise of unlocking emergent properties in POM-based frameworks and their potential ability in the field of photoelectron conversion.

4.5 Experimental methods

Chemicals. Chemical manufacturers and purities are given in **Table 4.1**. Ultrapure water was collected from a Barnstead Nanopure Water Purification System (Thermo Fisher). All chemicals were used without further purification.

Synthesis of the Preyssler cluster, $K_{14-x}Na_x[NaP_5W_{30}O_{110}]\cdot 15H_2O$ ($\{P_5W_{30}\}$). The Preyssler cluster was synthesized following a literature procedure[25] and optimized by our previous paper.[17] To imitate similar synthesis with frameworks which grew with or without light, $K_{14-x}Na_x[NaP_5W_{30}O_{110}]\cdot 15H_2O$ (130.0 mg, 0.0159 mmol) and aqueous $LiClO_4$ (2.0 ml, 0.5 M, pH 1.0–1.5, adjusted by 4 M HCl) were added to a 25-ml round-bottom flask equipped with a reflux condenser. The resulting colorless solution was heated at 90 °C with stirring for 20 h and cooled to room temperature. The colorless solution was then transferred to a 20-ml vial. The reaction was performed 2–5 times, and the vials were placed into a sealed 240-ml jar containing 80 ml MeOH and kept in the drawer without light or placed between two LEDs (ADJ Products Stage light unit, 365 nm wavelength) for one weeks. Crystals were observed within one week. Crystals were washed six times with 10 ml MeOH to remove any chloride salt impurities, as evidenced by the loss of Cl absorption in the energy dispersive X-ray spectrum.

Synthesis of Mo-doped cluster, $K_{14-x}Na_x[NaP_5MoW_{29}O_{110}]\cdot 15H_2O$ ($\{P_5MoW_{29}\}$). The Preyssler cluster was synthesized following our previous paper.[17] To imitate similar synthesis with frameworks which grew with or without light, $K_{14-x}Na_x[NaP_5MoW_{29}O_{110}]\cdot 15H_2O$ (130.0 mg, 0.0159 mmol) and aqueous $LiClO_4$ (2.0 ml, 0.5 M, pH 1.0–1.5, adjusted by 4 M HCl) were added to a 25-ml round-bottom flask equipped with a reflux condenser. The resulting yellow solution was heated at 90 °C with stirring for 20 h and cooled to room temperature. The yellow solution was then transferred to a 20-ml vial. The reaction was performed 2–5 times, and the vials were placed into a sealed 240-ml jar containing 80 ml MeOH and kept in the drawer without light or placed between two LEDs (ADJ Products Stage light unit, 365nm wavelength). Yellow crystals were observed within one week. Crystals were washed six times with 10 ml MeOH to remove any chloride salt impurities, as evidenced by the loss of Cl absorption in the energy dispersive X-ray spectrum.

Synthesis of TMs-bridged Preyssler frameworks (TMs= Mn, Fe, Co, Ni, Cu, and Zn). The frameworks were synthesized following our previous paper.[17] Detailed reaction conditions were shown in **Table 4.2**. After the reaction, the resulting solution was cooled to room temperature. The white powder was precipitated and filtered when $LiClO_4$ was used as the reaction solution. The remaining solution was then transferred to a 20-ml vial. The reaction was performed 2–5 times, and the vials were placed into a sealed 240-ml jar containing 80 ml MeOH and kept in the drawer without light or under the ultraviolet light for a couple of weeks. Crystals were observed within one week. Crystals were washed six times with 10 ml MeOH to remove any chloride salt impurities, as evidenced by the loss of Cl absorption in the energy dispersive X-ray spectrum. (The complicated formula, ICP, and TGA were shown in Table S3)

Electron titrations. In a nitrogen-filled glovebox ~10 mg (~1.2 μmol) as-grown framework powder was added to a 2-mm path length screw-cap cuvette containing ~ 17 equivalents $Cu[OTf]_2$ in 7:2:1 toluene/MeOH/MeCN and the Cu^{2+} $2E_g \rightarrow 2T_{2g}$ *d–d* absorption was monitored until it stopped decreasing (~6 days) while the added frameworks are precipitated at the bottom of the cuvette and not blocks the path of incident beam. This was repeated 3–4 times to obtain a linear decrease in Cu^{2+} absorption as a function of added framework. A linear fit to the data was used to determine the number of electrons transferred from the frameworks to Cu^{2+}. To show that the electron transfer was complete, aliquots of $Cu[OTf]_2$ in MeCN were added to the cuvette, and a linear increase in Cu^{2+} absorption could be fit to verify the equivalence point.

Formula determination. Elemental analysis was performed using inductively coupled plasma mass spectrometry (ICP–MS) collected on Thermo iCAP RQ ICP–MS. The samples were digested in a 1:1 mixture of 85% HNO_3 (Optima grade, Sigma Aldrich) and 30 % H_2O_2 (Trace metal grade, Sigma Aldrich) with sonication for 60 min. Thermogravimetric analysis (TGA) was collected on a Perkin-Elmer STA 6000 under N_2 with a heating-rate of 5 °C/s. The % mass of water was determined by the mass loss from 30 °C to 400 °C and rounded to the nearest 0.5 H_2O. Where appropriate, the experimental values are compared to literature values or to those calculated from the crystal structure.

X-ray photoelectron spectroscopy. The samples were pressed into pellets for the XPS measurement by loading ~80 mg dried powder into a 7 mm die (Specac GS03950) and pressing at 2 ton for 1 h. Then the pellets were further degassing by the Schlenk line with N_2. XPS measurements were acquired using a Kratos Analytical AXIS Supra surface analysis instrument under 5×10^{-8} torr using a monochromatic Al K_α X-ray source operating at 300W with an emission current of 20 mA. Survey spectra were measured with a 1 eV step, dwell-time of 100 ms and pass energy of 160 eV. Detail spectra of O 1*s*, W 4*f*, Zn 2*p*, Cu 2*p*, Mo 3*d*, and Zn LMM were averaged over 30 scans with a 0.1 eV step, 100 ms dwell-time and pass energy of 20 eV. Analysis of the XPS spectra was performed using Casaxps software and calibrated spectra based on O 1*s* at 530.0 eV. After background subtraction using the Shirley routine, spectra were fitted with a convolution of Lorentzian and Gaussian profiles.

Powder X-ray diffraction. PXRD patterns were collected on a Bruker K3 Kappa Vantec 500 diffractometer equipped with Cu K_a radiation (λ = 1.54184 Å). Diffraction images were merged/integrated into Diffrac. EVA V.4.2.2 (Bruker).

Table 4.1. Chemicals

Chemical	**Purity**	**Manufacturer**
Barium sulfate ($BaSO_4$)	>99%	Fisher Chemical
Cobalt(II) chloride hexahydrate ($CoCl_2{\cdot}6H_2O$)	98%	TCI America
Copper(II) chloride dihydrate ($CuCl_2{\cdot}2H_2O$)	>99%	Fisher Chemical
Copper(II) triflouromethanesulfonate, ($Cu[OTf]_2$)	99.95%	Oakwood Chemical
Hydrochloric acid (HCl)	36.50%	Fisher Chemical
Iron(II) chloride tetrahydrate ($FeCl_2{\cdot}4H_2O$)	98%	Alfa Aesar
Lithium chloride (LiCl)	>99%	Fisher Chemical
Lithium perchlorate trihydrate ($LiClO_4{\cdot}3H_2O$)	>95%	Alfa Aesar
Manganese(II) chloride tetrahydrate ($MnCl_2{\cdot}4H_2O$)	>95%	J. T Baker
Methanol (MeOH)	99.90%	Fisher Chemical
Nickel(II) chloride hexahydrate ($NiCl_2{\cdot}6H_2O$)	98%	Spectrum Chemical
Phosphoric acid (H_3PO_4)	85%	Acros Organics
Potassium chloride (KCl)	99%	Alfa Aesar
Sodium molybdate dihydrate ($Na_2MoO_4{\cdot}2H_2O$)	99.52%	Chem-impex
Sodium chloride (NaCl)	>99%	Fisher Chemical
Sodium tungstate dihydrate ($Na_2WO_4{\cdot}2H_2O$)	95%	Spectrum Chemical
Zinc chloride ($ZnCl_2$),	>95%	Fisher Chemical

Table 4.2. Summary of detailed reaction conditions.

Metal salt, Preyssler and aqueous solution were added to a 25-ml round-bottom flask equipped with a reflux condenser. The resulting solution was heated at 90 °C with stirring at for 20 h. Detailed reaction conditions were shown in the following table.

Frameworks	TMs	$\{P_5W_{30}\}/\{P_5MoW_{29}\}$	Reaction solution
Mn-$\{P_5W_{30}\}$	$MnCl_2{\cdot}4H_2O$ (130 mg, 0.657 mmol)	$\{P_5W_{30}\}$ (130 mg, 0.0159 mmol)	7 ml 1 M LiCl
Fe-$\{P_5W_{30}\}$	$FeCl_2{\cdot}4H_2O$ (130 mg, 0.654 mmol)	$\{P_5W_{30}\}$ (130 mg, 0.0159 mmol)	7 ml 1 M LiCl
Co-$\{P_5W_{30}\}$	$CoCl_2{\cdot}6H_2O$ (156 mg, 0.656 mmol)	$\{P_5W_{30}\}$ (130 mg, 0.0159 mmol)	7 ml 1 M LiCl
Ni-$\{P_5W_{30}\}$	$NiCl_2{\cdot}6H_2O$ (156 mg, 0.656 mmol)	$\{P_5W_{30}\}$ (130 mg, 0.0159 mmol)	7 ml 1 M LiCl
Cu-$\{P_5W_{30}\}$	$CuCl_2{\cdot}2H_2O$ (104 mg, 0.610 mmol)	$\{P_5W_{30}\}$ (130 mg, 0.0159 mmol)	2 ml 0.5 M $LiClO_4$
Zn-$\{P_5W_{30}\}$	$ZnCl_2$ (82 mg, 0.602 mmol)	$\{P_5W_{30}\}$ (130 mg, 0.0159 mmol)	2 ml 0.5 M $LiClO_4$
Mn-$\{P_5MoW_{29}\}$	$MnCl_2{\cdot}4H_2O$ (130 mg, 0.657 mmol)	$\{P_5MoW_{29}\}$ (130 mg, 0.0159 mmol)	7 ml 1 M LiCl
Fe-$\{P_5MoW_{29}\}$	$FeCl_2{\cdot}4H_2O$ (130 mg, 0.654 mmol)	$\{P_5MoW_{29}\}$ (130 mg, 0.0159 mmol)	7 ml 1 M LiCl
Co-$\{P_5MoW_{29}\}$	$CoCl_2{\cdot}6H_2O$ (156 mg, 0.656 mmol)	$\{P_5MoW_{29}\}$ (130 mg, 0.0159 mmol)	7 ml 1 M LiCl
Ni-$\{P_5MoW_{29}\}$	$NiCl_2{\cdot}6H_2O$ (156 mg, 0.656 mmol)	$\{P_5MoW_{29}\}$ (130 mg, 0.0159 mmol)	7 ml 1 M LiCl
Cu-$\{P_5MoW_{29}\}$	$CuCl_2{\cdot}2H_2O$ (104 mg, 0.610 mmol)	$\{P_5MoW_{29}\}$ (130 mg, 0.0159 mmol)	2 ml 0.5 M $LiClO_4$
Zn-$\{P_5MoW_{29}\}$	$ZnCl_2$ (82 mg, 0.602 mmol)	$\{P_5MoW_{29}\}$ (130 mg, 0.0159 mmol)	2 ml 0.5 M $LiClO_4$

Chapter 4, in part, is currently being prepared for submission for publication in Chen, L., **Jung, H.**, Schimpf, A. M.* Air-Stable Reduction of Zn-Bridged Preyssler-Type Polyoxometalate Frameworks. Manuscript in Preparation. The author of this dissertation was the second author of the material.

4.6 References

1. Long, D. L.; Burkholder, E.; Cronin, L., Polyoxometalate Clusters, Nanostructures and Materials: From Self Assembly to Designer Materials and Devices. *Chem. Soc. Rev.* **2007,** *36* (1), 105.

2. Petel, B. E.; Brennessel, W. W.; Matson, E. M., Oxygen-Atom Vacancy Formation at Polyoxovanadate Clusters: Homogeneous Models for Reducible Metal Oxides. *J. Am. Chem. Soc.* **2018,** *140* (27), 8424.

3. Hill, C. L., Introduction: Polyoxometalates - Multicomponent Molecular Vehicles to Probe Fundamental Issues and Practical Problems. *Chem. Rev.* **1998,** *98* (1), 1.

4. Cronin, L.; Muller, A., From Serendipity to Design of Polyoxometalates at the Nanoscale, Aesthetic Beauty and Applications. *Chem. Soc. Rev.* **2012,** *41* (22), 7333.

5. Song, Y. F.; Tsunashima, R., Recent Advances on Polyoxometalate-Based Molecular and Composite Materials. *Chem. Soc. Rev.* **2012,** *41* (22), 7384.

6. Long, D. L.; Tsunashima, R.; Cronin, L., Polyoxometalates: Building Blocks for Functional Nanoscale Systems. *Angew. Chem. Int. Edit.* **2010,** *49* (10), 1736.

7. Yamase, T., Photo- and Electrochromism of Polyoxometalates and Related Materials. *Chem. Rev.* **1998,** *98* (1), 307.

8. Long, D. L.; Burkholder, E.; Cronin, L., Polyoxometalate Clusters, Nanostructures and Materials: From Self Assembly to Designer Materials and Devices. *Chem. Soc. Rev.* **2007,** *36* (1), 105.

9. Boyd, T.; Mitchell, S. G.; Gabb, D.; Long, D. L.; Song, Y. F.; Cronin, L., POMzites: A Family of Zeolitic Polyoxometalate Frameworks from a Minimal Building Block Library. *J. Am. Chem. Soc.* **2017,** *139* (16), 5930.

10. Vila-Nadal, L.; Cronin, L., Design and Synthesis of Polyoxometalate-Framework Materials From Cluster Precursors. *Nat. Rev. Mater.* **2017,** *2* (10), 17054.

11. Liu, Q. D.; He, P. L.; Yu, H. D.; Gu, L.; Ni, B.; Wang, D.; Wang, X., Single Molecule-Mediated Assembly of Polyoxometalate Single-Cluster Rings and Their Three-Dimensional Superstructures. *Sci. Adv.* **2019,** *5* (7).

12. Miras, H. N.; Vila-Nadal, L.; Cronin, L., Polyoxometalate Based Open-Frameworks (POM-OFs). *Chem. Soc. Rev.* **2014,** *43* (16), 5679.

13. Hutin, M.; Long, D. L.; Cronin, L., Controlling the Molecular Assembly of Polyoxometalates from the Nano to the Micron Scale: Molecules to Materials. *Isr. J. Chem.* **2011,** *51* (2), 205.

14. Gumerova, N. I.; Rompel, A., Synthesis, Structures and Applications of Electron-Rich Polyoxometalates. *Nature Rev. Chem.* **2018,** *2* (2).

15. GomezRomero, P.; CasanPastor, N., Photoredox Chemistry in Oxide Clusters. Photochromic and Redox Properties of Polyoxometalates in Connection with Analog Solid State Colloidal Systems. *J. Phys. Chem.* **1996,** *100* (30), 12448.

16. Lopez, X.; Carbo, J. J.; Bo, C.; Poblet, J. M., Structure, Properties and Reactivity of Polyoxometalates: a Theoretical Perspective. *Chem. Soc. Rev.* **2012,** *41* (22), 7537.

17. Chen, L. F.; San, K. A.; Turo, M. J.; Gembicky, M.; Fereidouni, S.; Kalaj, M.; Schimpf, A. M., Tunable Metal Oxide Frameworks via Coordination Assembly of Preyssler-Type Molecular Clusters. *J. Am. Chem. Soc.* **2019,** *141* (51), 20261.

18. Turo, M. J.; Chen, L. F.; Moore, C. E.; Schimpf, A. M., Co^{2+}-Linked $[NaP_5W_{30}O_{110}]^{14-}$: A Redox-Active Metal Oxide Framework with High Electron Density. *J. Am. Chem. Soc.* **2019,** *141* (11), 4553.

19. Liao, C. C.; Chen, F. R.; Kai, J. J., Electrochromic Properties of Nanocomposite WO_3 Films. *Sol. Energ. Mat. Sol. C* **2007,** *91* (14), 1282.

20. Cai, G. F.; Cui, M. Q.; Kumar, V.; Darmawan, P.; Wang, J. X.; Wang, X.; Eh, A. L. S.; Qian, K.; Lee, P. S., Ultra-Large Optical Modulation of Electrochromic Porous WO_3 Film and the Local Monitoring of Redox Activity. *Chem. Sci.* **2016,** *7* (2), 1373.

21. Prabhakaran, V.; Lang, Z. L.; Clotet, A.; Poblet, J. M.; Johnson, G. E.; Laskin, J., Controlling the Activity and Stability of Electrochemical Interfaces Using Atom-by-Atom Metal Substitution of Redox Species. *ACS Nano* **2019,** *13* (1), 458.

22. Belhouari, A.; Keita, B.; Nadjo, L.; Contant, R., Efficient Conversion of NO into N_2O by Selected Electroreduced Heteropolyanions. *New J. Chem.* **1998,** *22* (2), 83.

23. Keita, B.; Girard, F.; Nadjo, L.; Contant, R.; Belghiche, R.; Abbessi, M., Cyclic Voltammetric Evidence of Facilitation of the Reduction of Nitrite by the Presence of Molybdenum in Fe- or Cu-Substituted Heteropolytungstates. *J. Electroanal. Chem.* **2001,** *508* (1-2), 70.

24. Song, I. K.; Barteau, M. A., Redox Properties of Keggin-Type Heteropolyacid (HPA) Catalysts: Effect of Counter-Cation, Heteroatom, and Polyatom Substitution. *J. Mol. Catal. a-Chem.* **2004,** *212* (1-2), 229.

25. Hayashi, A.; Haioka, T.; Takahashi, K.; Bassil, B. S.; Kortz, U.; Sano, T.; Sadakane, M., Cation Effect on Formation of Preyssler-type 30-Tungsto-5-phosphate: Enhanced Yield of Na-encapsulated Derivative and Direct Synthesis of Ca- and Bi-Encapsulated Derivatives. *Z. Anorg. Allg. Chem.* **2015,** *641* (15), 2670.

Appendix A. Supplementary Information for Chapter 2: Photochemical Reduction of Nanocrystalline Maghemite to Magnetite

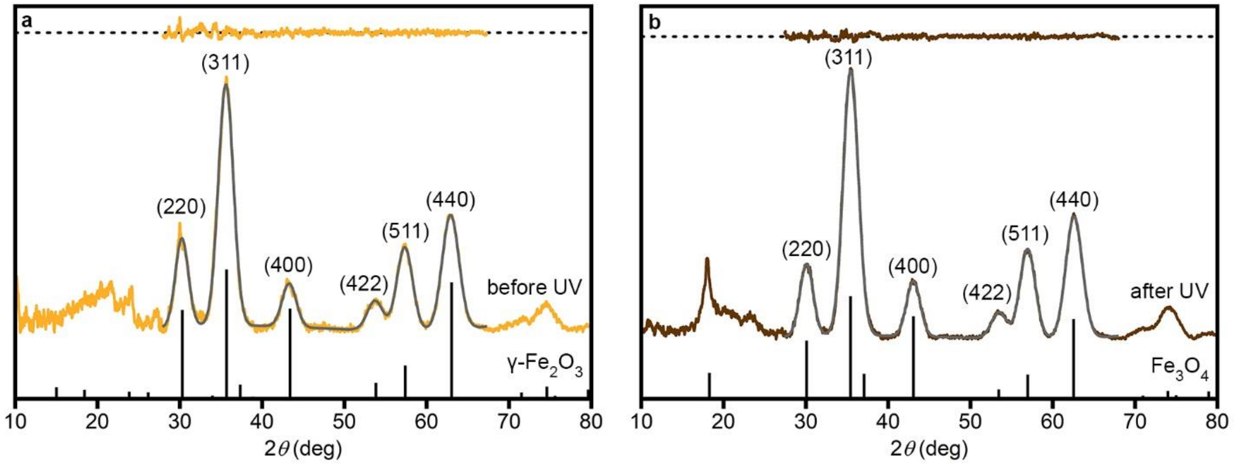

Figure A.1. Full pXRD patterns of <*d*> = 4.8 nm nanocrystals **(a)** before and **(b)** after UV irradiation. Experimental patterns are compared to those simulated from single-crystal data for γ-Fe_2O_3 (250541)[1] and Fe_3O_4 (ICSD# 26410)[2], respectively. Experimental patterns were fit from $2\theta \approx 28–67°$ (gray trace) and the residuals shown for comparison (top). These fits were used to evaluate the changes upon photoreduction (Table S1). All patterns are plotted for diffraction of Cu Kα radiation (1.5406 Å).

Table A.1. Comparison of 2θ values for representative reflections of <*d*> = 4.8 nm nanocrystals before (oxidized) and after (photoreduced) UV irradiation with EtOH or $LiEt_3BH$. Experimental values are derived from fits to the powder patterns (**Figure A.1**). Values for γ-Fe_2O_3 (ICSD# 250541)[1] and Fe_3O_4 (ICSD# 26410)[2] simulated from single-crystal data are given for comparison. All values are given for diffraction of Cu Kα radiation (1.5406 Å).

Reflection (hkl)	γ-Fe_2O_3 (ref. 1)	Oxidized	Photoreduced with EtOH	Fe_3O_4 (ref. 2)
220	30.301	30.249 ± 0.004	30.082 ± 0.002	30.087
311	35.692	35.600 ± 0.001	35.459 ± 0.001	35.439
400	43.383	43.288 ± 0.008	43.066 ± 0.003	43.070
422	53.831	53.731 ± 0.013	53.479 ± 0.008	53.431
511	57.388	57.327 ± 0.005	56.944 ± 0.002	56.958
440	63.028	62.899 ± 0.003	62.595 ± 0.002	62.545

Table A.2. Comparison of unit-cell size for γ-Fe_2O_3 and Fe_3O_4.

	a **(Å)**	**ICSD #**	**Ref.**
γ-Fe_2O_3	8.3364	250541	[1]
Fe_3O_4	8.3941	26410	[2]

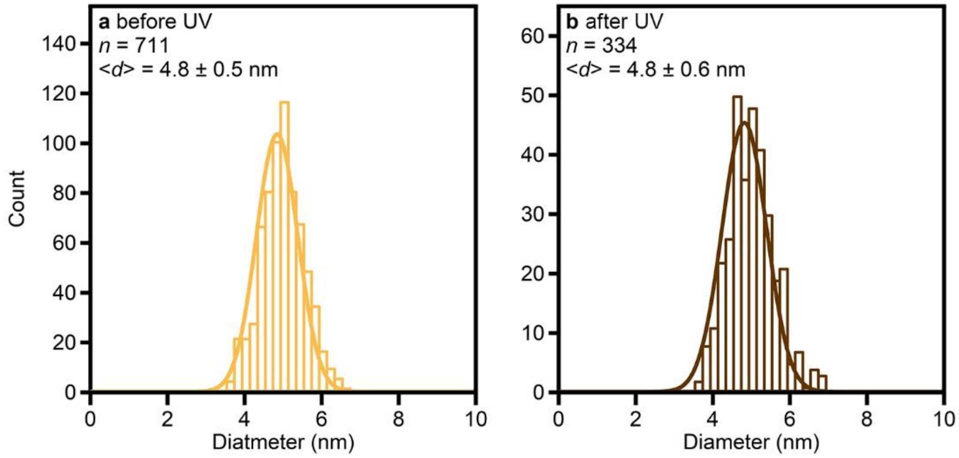

Figure A.2. Statistical analysis of TEM images of <*d*> = 4.8 nm γ-Fe_2O_3 nanocrystals **(a)** before and **(b)** after 3 h UV irradiation in the presence of EtOH.

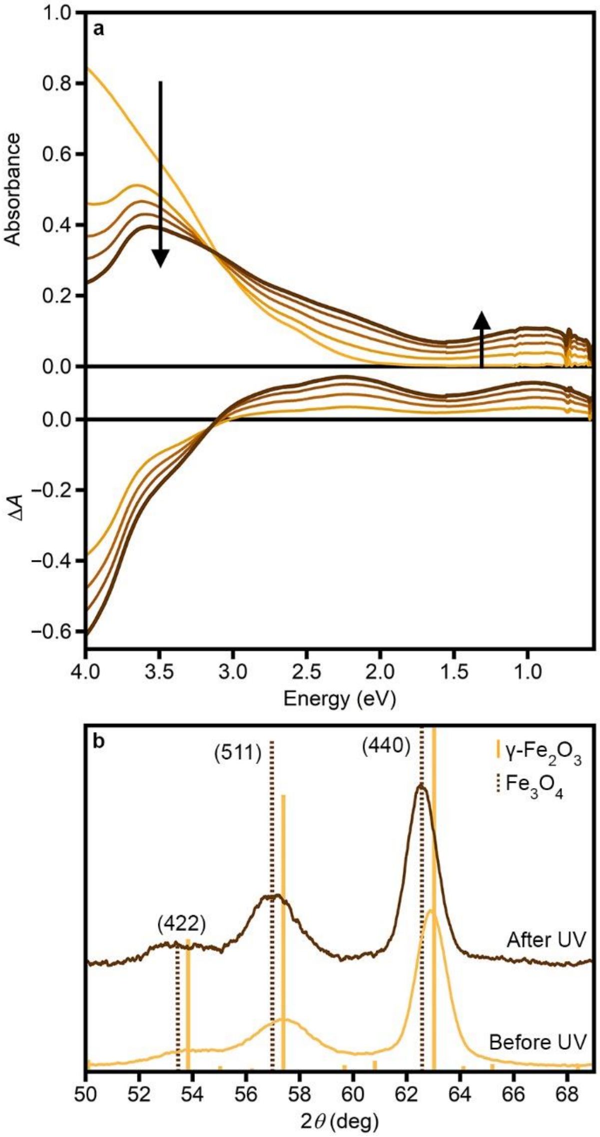

Figure A.3. Photochemical conversion of γ-Fe_2O_3 to Fe_3O_4 in <*d*> = 9.0 nm nanocrystals. **(a)** Absorption spectra of nanocrystals ([Fe] = 0.98 mM) with increasing UV irradiation. Inset: Photographs of the colloidal suspension before (left) and after (right) 3 h UV irradiation show a color change from yellow to brown. **(b)** pXRD patterns before (yellow) and after (brown) 3 h UV irradiation. Simulated patterns for γ-Fe_2O_3 (solid yellow)[1] and Fe_3O_4 (dashed brown)[2] are shown for reference. All patterns are plotted for diffraction of Cu Kα radiation (1.5406 Å).

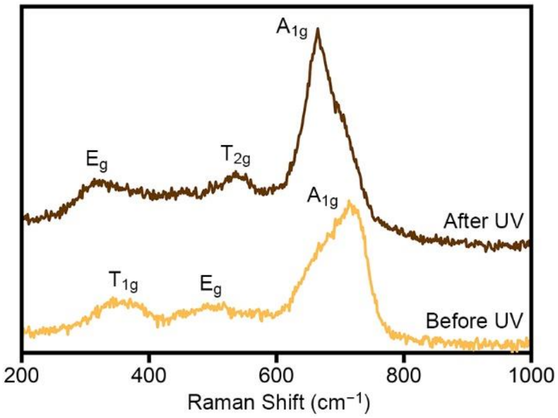

Figure A.4. Raman spectra of <*d*> = 9.0 nm nanocrystals before (yellow) and after (brown) UV irradiation. Peak assignments, including the narrowing and blueshifting of the A_{1g} mode upon UV irradiation, are indicative of conversion to magnetite.[3-4]

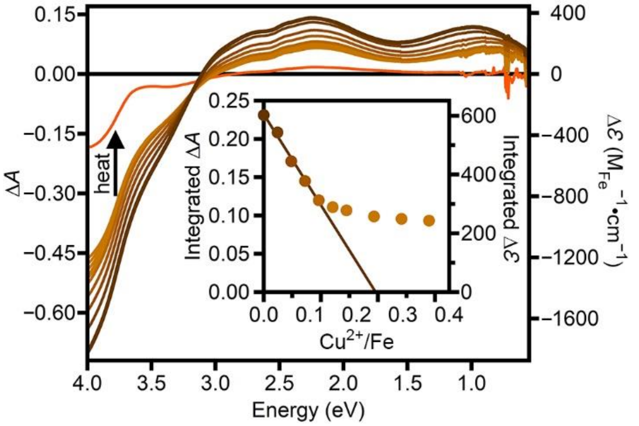

Figure A.5. Absorption and extinction (plotted as $\Delta A = A{-}A_{\mathrm{BeforeUV}}$ and $\Delta\varepsilon = \varepsilon{-}\varepsilon_{\mathrm{BeforeUV}}$, respectively) spectra of photoreduced <*d*> = 4.8 nm nanocrystals ([Fe] = 1.0 mM) with added Cu[OTf]$_2$. Inset: Integrated (0.8–3.0 eV) ΔA as a function of Cu^{2+}/Fe. The linear fit is used to estimate the fraction of Fe^{2+} in the photoreduced nanocrystals. After 0.18 equiv Cu^{2+}/Fe, further Cu[OTf]$_2$ addition leads to very little change in the absorption spectra. The solution of nanocrystals + 0.58 equiv Cu[OTf]$_2$ was heated for 2 h at 85 °C to further drive the oxidation.

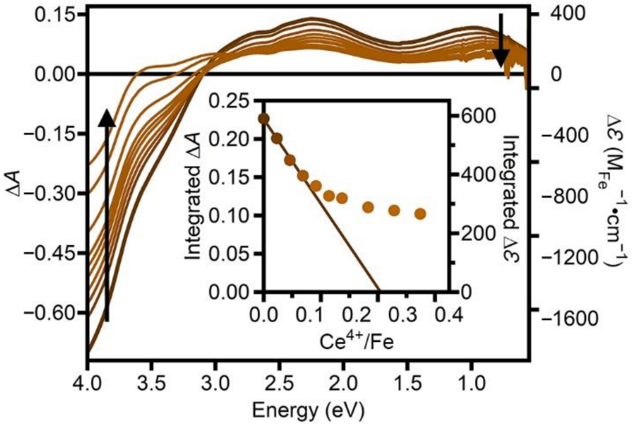

Figure A.6. Absorption and extinction (plotted as $\Delta A = A{-}A_{\mathrm{BeforeUV}}$ and $\Delta\varepsilon = \varepsilon{-}\varepsilon_{\mathrm{BeforeUV}}$, respectively) spectra of photoreduced <*d*> = 4.8 nm nanocrystals ([Fe] = 1.0 mM) with added $(NH_4)_2Ce(NO_3)_6$. Inset: Integrated (0.8–3.0 eV) ΔA as a function of Ce^{4+}/Fe. The linear fit is used to estimate the fraction of Fe^{2+} in the photoreduced nanocrystals (41 %). After 0.14 equiv Ce^{4+}/Fe, further $(NH_4)_2Ce(NO_3)_6$ addition leads to relatively little change in the absorption spectra.

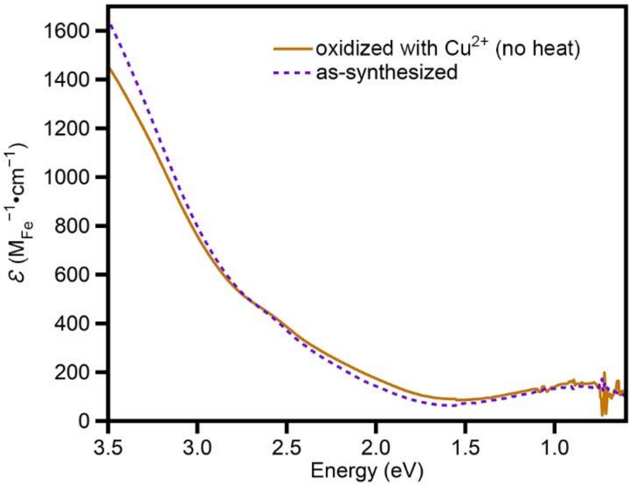

Figure A.7. Extinction spectra of maximally photoreduced <*d*> = 4.8 nm nanocrystals ([Fe] = 1.0 mM) with 0.58 equiv Cu[OTf]$_2$ per Fe added (solid brown) compared to that of as-synthesized nanocrystals (dashed purple).

Table A.3. Summary of titration results for <*d*> = 4.8 nm nanocrystals photoreduced with EtOH as the sacrificial reductant.

Oxidant	**% Fe^{2+}**
Cu[OTf]$_2$	39 (**Figure 2.2**)
Cu[OTf]$_2$	47
Cu[OTf]$_2$	45
$(NH_4)_2Ce(NO_3)_6$	41
Average	**43 ± 4**

Table A.4. Size-dependence of ensemble photochemical reduction rate, *k*, determined by fitting the data in **Figure 2.3** (inset) to $\Delta\varepsilon = C(1 - e^{-kt})$.

<*d*> (nm)	***k* (h^{-1})**
4.8	1.8
7.3	1.1
9.0	0.90

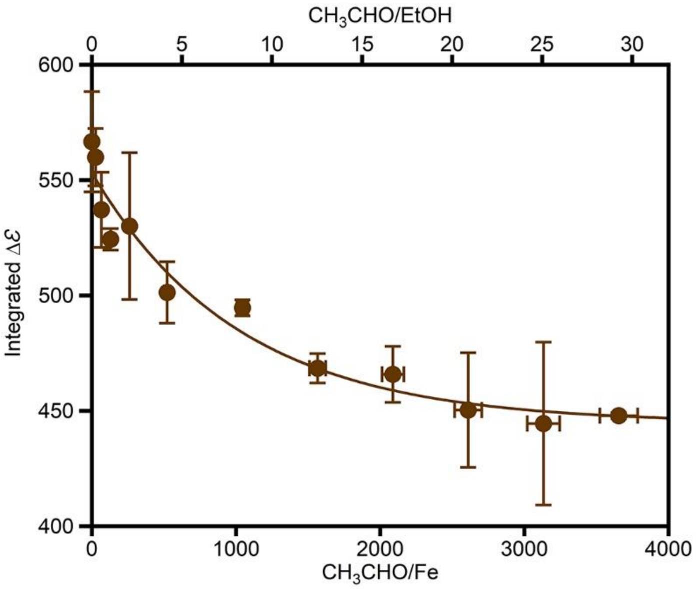

Figure A.8. Integrated extinction intensities ($\Delta\varepsilon = \varepsilon - \varepsilon_{\mathrm{BeforeUV}}$) for <*d*> = 4.8 nm nanocrystals maximally photoreduced in the presence of added acetaldehyde (CH_3CHO). The solid line is a guide to the eye.

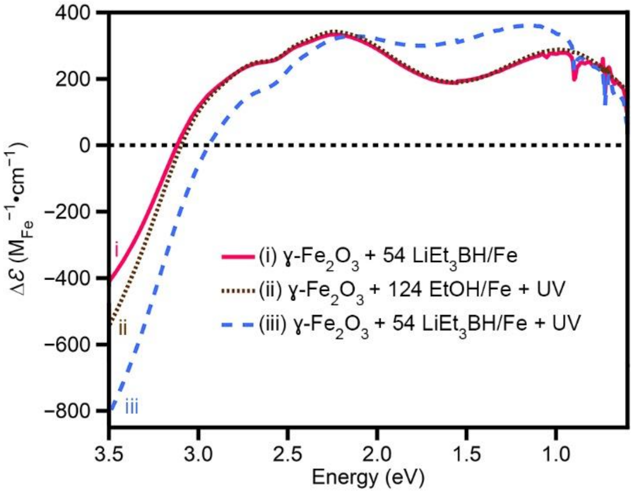

Figure A.9. (i) Differential extinction spectrum ($\Delta\varepsilon = \varepsilon - \varepsilon_{\mathrm{NoLiEt3BH}}$) of <*d*> =4.8 nm nanocrystals with added $LiEt_3BH$ in the dark compared to (ii) the differential extinction spectrum ($\Delta\varepsilon = \varepsilon - \varepsilon_{\mathrm{BeforeUV}}$) of the same nanocrystals maximally photoreduced with EtOH. (iii) UV irradiation of $LiEt_3BH$-treated nanocrystals leads to further spectroscopic changes.

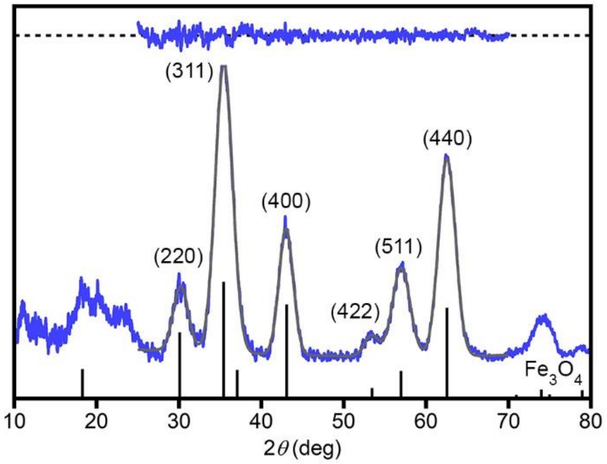

Figure A.10. PXRD pattern of <*d*> = 4.8 nm nanocrystals after 5 h UV irradiation in the presence of $LiEt_3BH$. The pattern for Fe_3O_4 simulated from single-crystal data (ICSD# 26410, ref. [2]) is shown for comparison. The experimental pattern was fit from $2\theta \approx 28$–67° (gray trace) and the residuals shown for comparison (top). All patterns are plotted for diffraction of Cu Kα radiation (1.5406 Å).

Table A.5. Exchange bias (H_E) of iron oxide nanocrystals with varying amounts of UV irradiation

Irradiation time (h)	$\boldsymbol{H_E}$ **(Oe)**
4.8 nm (**Figure 2.4**)	
0	−0.04
1	−0.39
6.5	1.19
9.0 nm (**Figure A.9**)	
0	9.01
1.5	−118
4	−117

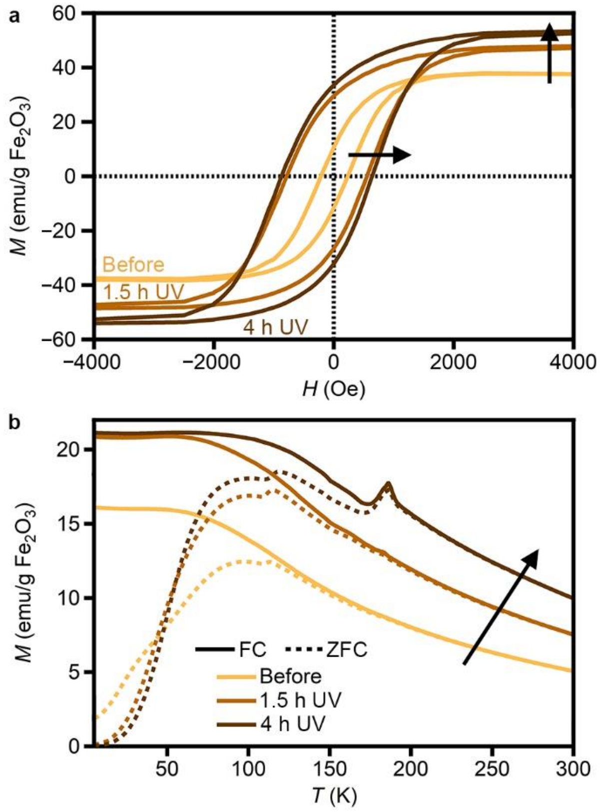

Figure A.11. Magnetic properties following UV irradiation of <*d*> = 9.0 nm nanocrystals. Magnetization as a function of **(a)** applied field at 5 K and **(b)** temperature for field-cooled (FC, solid lines, 100 Oe) and zero-field-cooled (ZFC, dashed lines) samples. Arrows show changes with increasing UV irradiation.

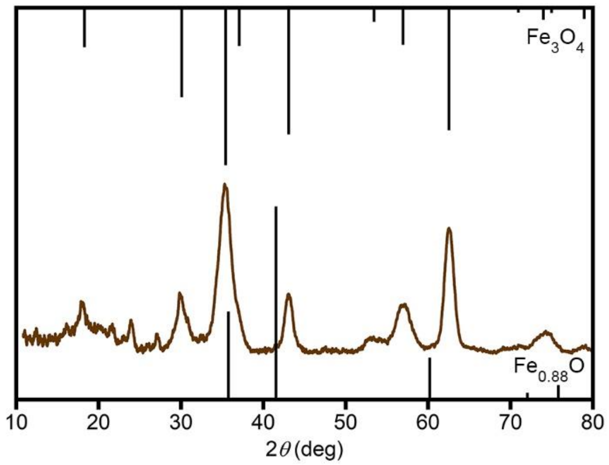

Figure A.12. PXRD pattern of <*d*> = 9.0 nm nanocrystals after 48 h UV irradiation with EtOH as a sacrificial reductant. The patterns for $Fe_{0.88}O$ (bottom, ICSD# 67203, ref. [5]) and Fe_3O_4 (ICSD# 26410, ref. [2]) simulated from single-crystal data is shown for comparison. All patterns are plotted for diffraction of Cu Kα radiation (1.5406 Å).

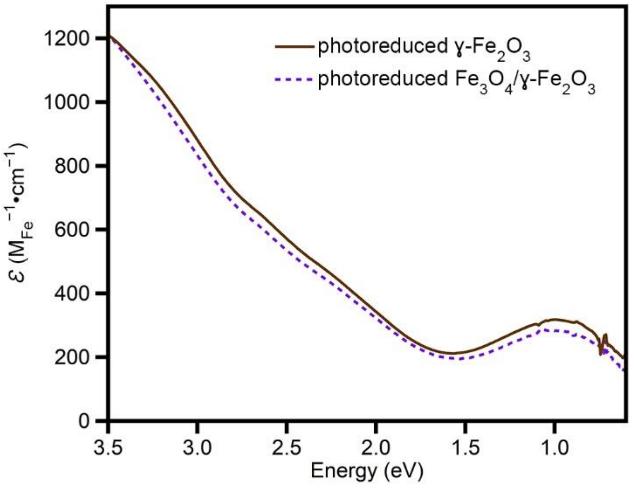

Figure A.13. Extinction spectra of maximally photoreduced as-synthesized (γ-Fe_2O_3/Fe_3O_4, dashed purple) and oxidized (γ-Fe_2O_3) <*d*> = 4.8 nm nanocrystals with EtOH as the sacrificial reductant

References

1. Solano, E.; Frontera, C.; Puig, T.; Obradors, X.; Ricart, S.; Ros, J., Neutron and X-Ray Diffraction Study of Ferrite Nanocrystals Obtained by Microwave-Assisted Growth. A Structural Comparison With the Thermal Synthetic Route. *J. Appl. Crystallogr.* **2014,** *47*, 414.

2. Fleet, M., The Structure of Magnetite. *Acta Crystallogr. B* **1981,** *37* (4), 917.

3. Testa-Anta, M.; Ramos-Docampo, M. A.; Comesana-Hermo, M.; Rivas-Murias, B.; Salgueirino, V., Raman spectroscopy to unravel the magnetic properties of iron oxide nanocrystals for bio-related applications. *Nanoscale Adv.* **2019,** *1* (6), 2086.

4. Dar, M. I.; Shivashankar, S. A., Single crystalline magnetite, maghemite, and hematite nanoparticles with rich coercivity. *RSC Adv.* **2014,** *4* (8), 4105.

5. Radler, M. J.; Cohen, J. B.; Faber, J., Point-Defect Clusters in Wüstite. *J. Phys. Chem. Solids* **1990,** *51* (3), 217.

Appendix B: Supplementary Information for Chapter 3: UV irradiation of Colloidal WSe2 Nanocrystals Using Lithium Triethylborohydride

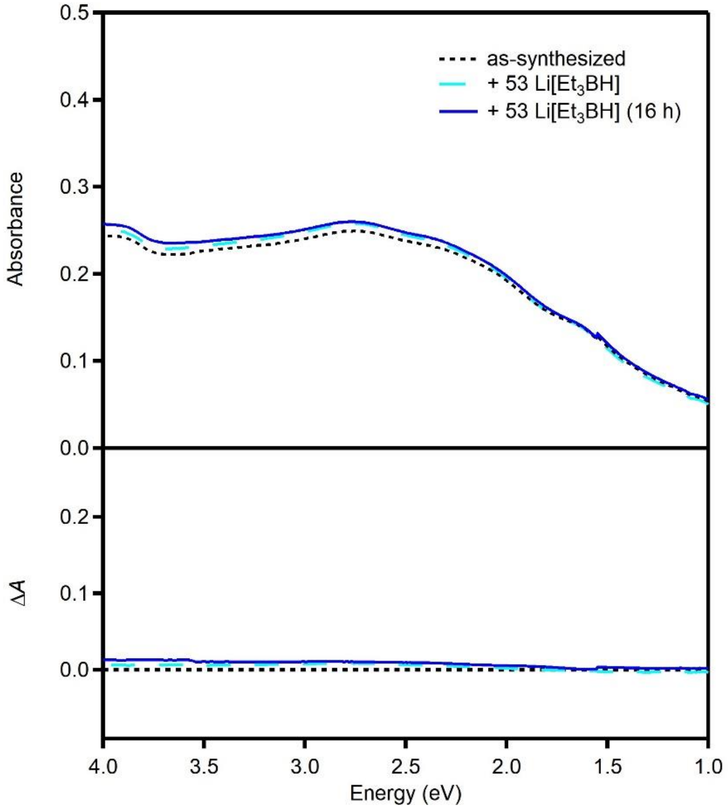

Figure B.1 Absorption (top) and differential absorption (bottom) spectra of an anaerobic solution of as-synthesized WSe_2 nanocrystals (dotted black; [W] = 0.13 mM in 1/1 tol/THF by volume), the same solution immediately after the addition of Li[Et_3BH] (53 equiv per W; dashed light blue) and 16 h after Li[Et_3BH] addition (solid dark blue).

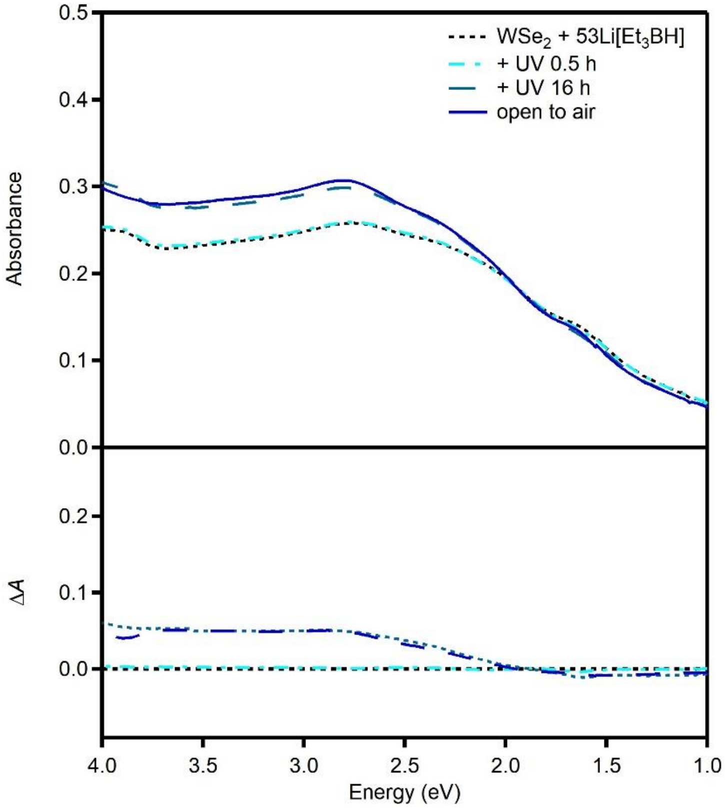

Figure B.2. Absorption (top) and differential absorption (bottom) spectra of an anaerobic solution of WSe_2 nanocrystals with 53 equiv $Li[Et_3BH]$ (dotted black; [W] = 0.13 mM in 1/1 tol/THF by volume), the same solution after 30 min UV irradiation, (dash-dotted turquoise), after 16 h UV irradiation (dashed light-blue), and after exposure to air (solid dark blue).

Table B.1. The intensity and energy of the C-exciton absorption of WSe_2 nanocrystals before and after 31 h UV irradiation with $Li[Et_3BH]$ (53 equiv per W), and after recovery with MeOH addition.

	A_{max}	E_{max} (eV)
As-synthesized	0.26	2.743
$Li[Et_3BH]$/UV	0.34	2.857
Recovered with MeOH	0.27	2.767

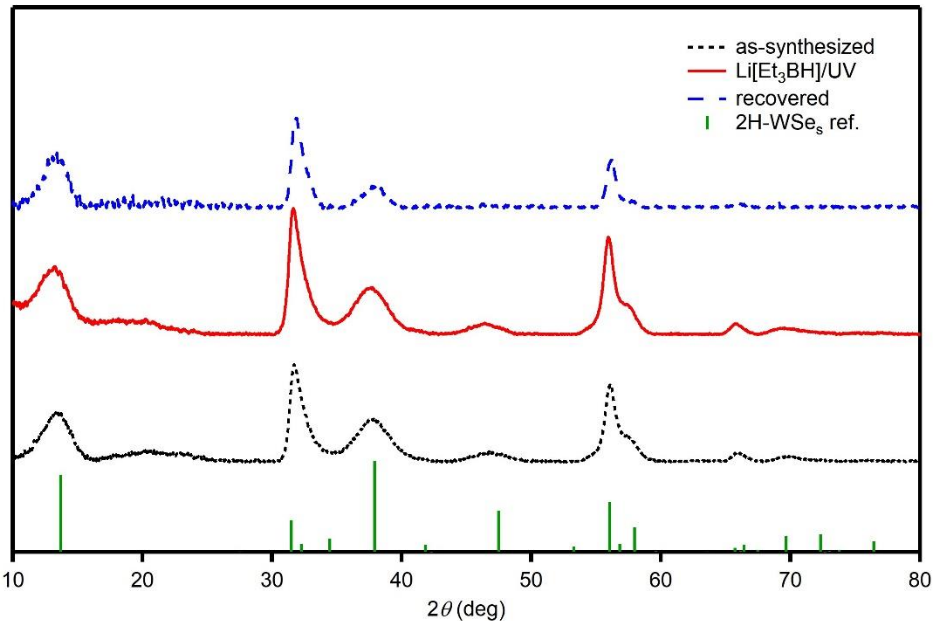

Figure B.3. Powder X-ray diffraction patterns of WSe_2 nanocrystals: as-synthesized (black dotted), irradiated with UV in the presence of Li[Et$_3$BH] (solid red), and recovered with MeOH addition (dashed blue). A reference pattern for 2H-WSe_2 (green, tabulated from ICSD# 40752)[1]. All values are given for diffraction of Cu K_α radiation (1.54184 Å).

Table B.2 Comparison of 2θ-values for representative reflections of as-prepared, Li[Et$_3$BH]/UV-treated, and recovered WSe_2 nanocrystals. Experimental values are derived from fits to the powder patterns (**Figure B.1**). Values for WSe_2 (ICSD# 40752, ref.1) is given for comparison. All values are given for diffraction of Cu K_α radiation (1.54184 Å).

Reflection (hkl)	**WSe_2**	**As-prepared**	**Treated with Li[Et$_3$BH]/UV**	**Recovered**
002	13.665	13.315 ± 0.008	12.912 ± 0.011	13.270 ± 0.005
100	31.475	31.941 ± 0.003	31.871 ± 0.004	31.989 ± 0.002
103	37.891	37.704 ± 0.011	37.520 ± 0.014	37.902 ± 0.013
110	56.041	56.067 ± 0.007	55.950 ± 0.007	56.185 ± 0.004

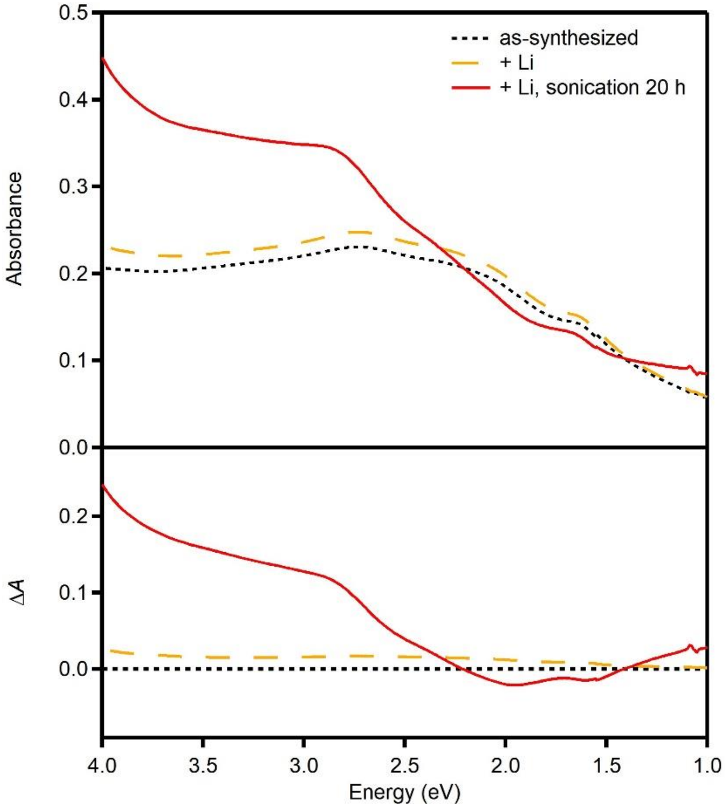

Figure B.4. Absorption (top) and differential absorption (bottom) spectra of an anaerobic solution of WSe_2 nanocrystals (dotted black; [W] = 0.13 mM in 1/1 tol/THF by volume), the same solution immediately after adding Li metal (dashed yellow) and after 20 h sonication with Li metal (solid red).

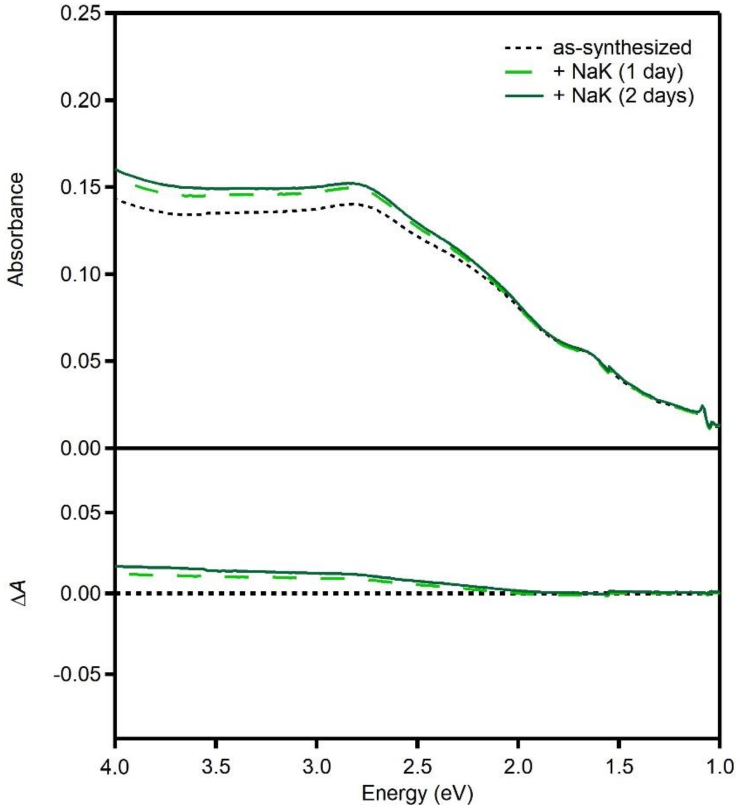

Figure B.5 Absorption (top) and differential absorption (bottom) spectra of an anaerobic solution of WSe_2 nanocrystals (dotted black; [W] = 0.13 mM in THF), the same solution 1 day after adding NaK (dashed light green) and 2 days after adding NaK (solid dark green).

References

1. Schutte, W. J.; Deboer, J. L.; Jellinek, F., Crystal-Structures of Tungsten Disulfide and Diselenide. *J. Solid State Chem.* **1987,** *70* (2), 207.

Appendix C: Supplementary Information for Chapter 4: Air-Stable Reduction of Zn-Bridged Preyssler-Type Polyoxometalate Frameworks

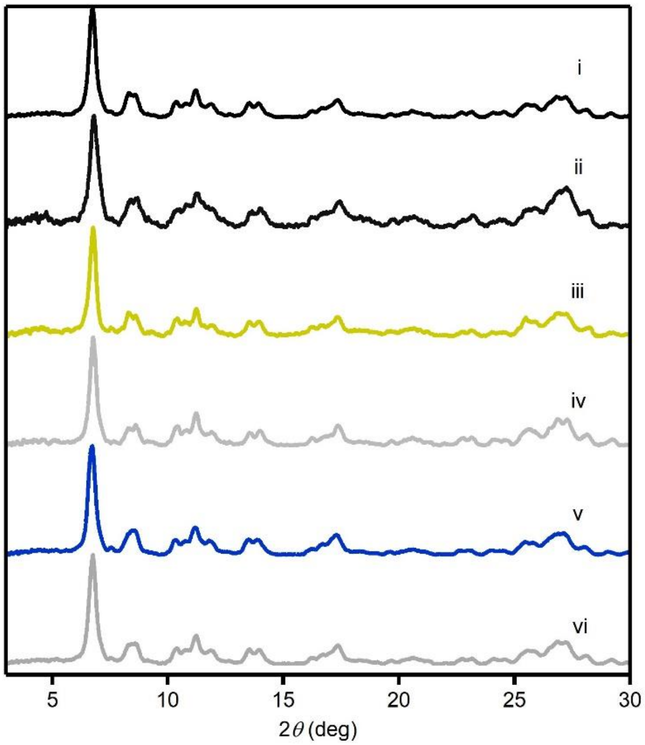

Figure C.1. pXRD patterns of (i) Zn-bridged {P_5MoW_{29}} frameworks grown in light and stored anaerobically in the dark for 3 months (ii) Zn-bridged {P_5MoW_{29}} frameworks grown in light (iii) Zn-bridged {P_5MoW_{29}} frameworks grown in the dark (iv) Zn-bridged {P_5W_{30}} frameworks grown in light and stored anaerobically in the dark for 3 months (iv) Zn-bridged {P_5W_{30}} frameworks grown in light (iv) Zn-bridged {P_5W_{30}} frameworks grown in the dark.

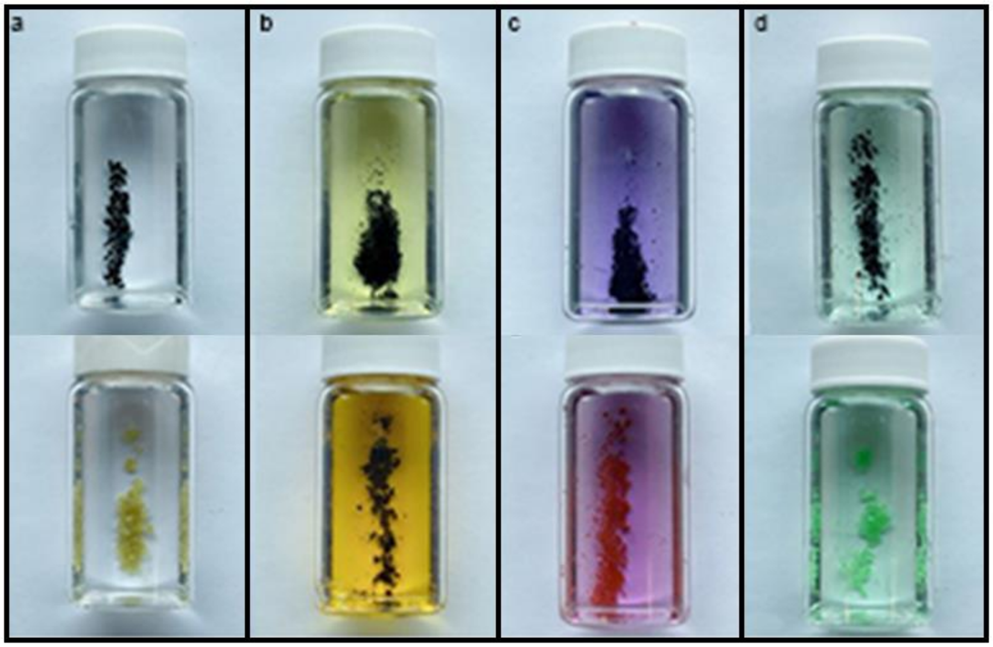

Figure C.2. Photographs of (a) Mn-, (b) Fe-, (c) Co-, and (d) Ni-bridged {P_5MoW_{29}} frameworks grown (top) under UV irradiation and (bottom) in the dark.

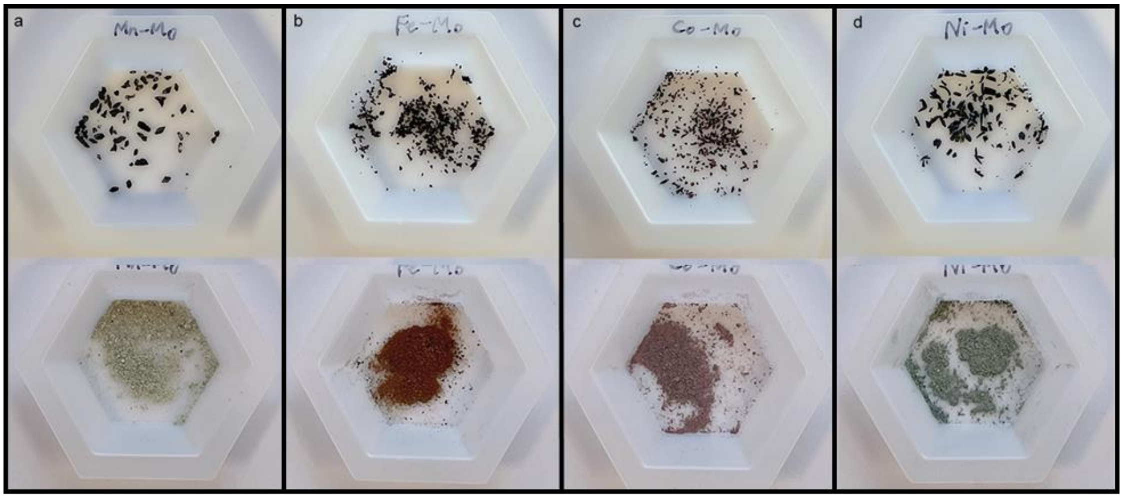

Figure C.3. Photographs of (a) Mn-, (b) Fe-, (c) Co-, and (d) Ni-bridged {P_5MoW_{29}} frameworks powders (top) grown under UV irradiation and (bottom) stored aerobically in the dark for 4 weeks.

Table C.1 Summary of titration results by the addition of framework in $Cu[OTf]_2$ solution

	e^- per $\{P_5MoW_{29}\}$	e^- density ($10^{20}/cm^3$)
Titration 1	3.3	8.9
Titration 2	3.0	8.0
Titration 3	3.2	8.7
Average	3.2 ± 0.1	8.5 ± 0.4

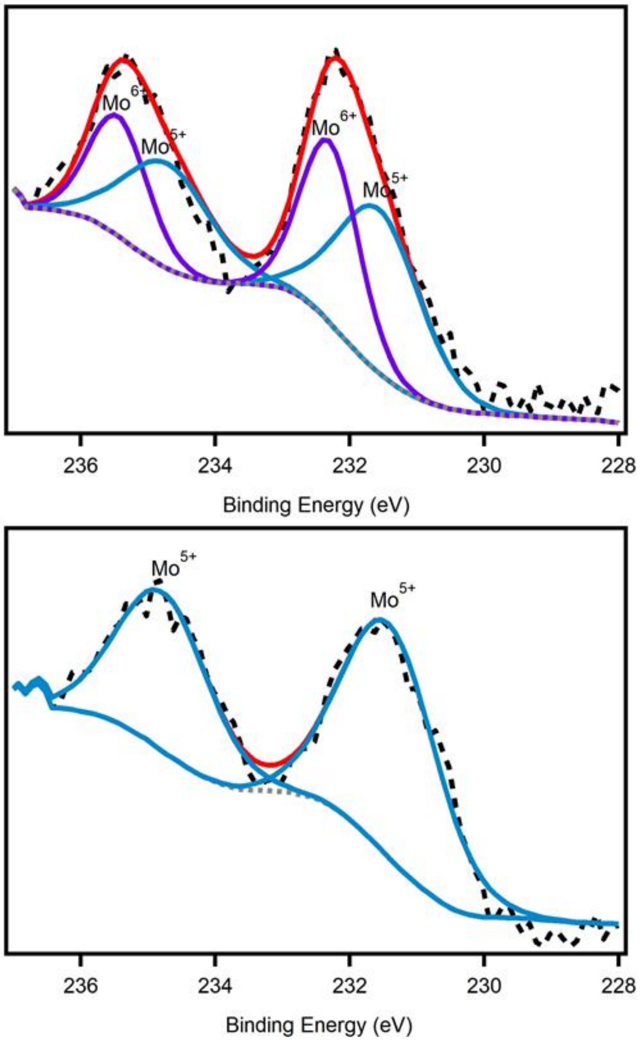

Figure C.4 Mo *3d* X-ray photoelectron spectrum of Zn-bridged {P_5MoW_{29}} frameworks (a) grown in the dark and (b) grown under UV irradiation. Dashed black traces are experimental. Solid blue, purple and red traces are the fits to Mo^{5+}, Mo^{6+} and the overall envelope, respectively.